Nano Today 55 (2024) 102162

Contents lists available at ScienceDirect

Nano Today

journal homepage: www.elsevier.com/locate/nanotoday

Review

Manufacturing and applications of multi-functional holey two-dimensional nanomaterials – A review

Dini Wang [a], Yan Dou [a], Xing Zhang [b], Kun Bi [a], Iyyappa Rajan Panneerselvam [c], Haofan Sun [a], Xinyu Jiang [a], Rui Dai [a], Kenan Song [d], Houlong Zhuang [a], Yongfeng Lu [e], Yan Wang [c], Yiliang Liao [b], Ling Ding [f], Qiong Nian [a,*]

[a] *School of Engineering for Matter, Transport and Energy, Arizona State University, Tempe, AZ 85287, USA*
[b] *Department of Industrial and Manufacturing Systems Engineering, Iowa State University, Ames, IA 50011, USA*
[c] *Department of Mechanical Engineering, University of Nevada, Reno, Reno, NV 89557, USA*
[d] *School of manufacturing systems and networks, Arizona State University, Mesa, AZ 85212, USA*
[e] *Department of Electrical and Computer Engineering, University of Nebraska–Lincoln, Lincoln, NE 68588, USA*
[f] *School of Chemistry and Chemical Engineering, Coal Conversion and New Carbon Materials Hubei Key Laboratory, Wuhan University of Science and Technology, Wuhan 430081, China*

ARTICLE INFO

Keywords:
Holey
Two-dimensional materials
Nanomanufacturing
Etching
Lithography
Electrochemical energy storage
Electrocatalysis
Molecular separation
Biosensing
Electronics

ABSTRACT

Recent research on holey 2D nanomaterials has embarked a new field in nanomaterial science and engineering. The versatility of physics and chemical properties of this group of materials opens up larger improvement spaces for the development of various applications involving energy storage and transfer, electronics, electrochemical catalysis, biochemical sensing, molecular separation, and among many others. To obtain the holey 2D nanomaterials, researchers have proposed many effective methods including oxidative etching, catalyzed etching, replacement etching, high-energy impact, lithography, templated assembly, decomposition, and bottom-up synthesis. To help understanding and further promoting the advance of this area, this review focuses on two main topics: i) demonstrating the advantages of a variety of holey 2D nanomaterials and their improvements in a broad range of applications; ii) summarizing and comparing various manufacturing approaches of the holey 2D nanomaterials and the corresponding mechanisms. In the end, this paper discusses the future development of holey 2D nanomaterials and analyzes the challenges and remaining issues with the expectation to provide effective insights in this area and inspire new ideas and conceptions for the researchers from different areas.

Introduction

The rise of two-dimensional (2D) nanomaterials brings a significant revolution in the developments of a wide range of fields, such as energy storage and conversion,[1] semiconductors,[2] biochemical,[3] and environmental applications.[4] The large specific surface area of 2D nanomaterials drastically increase the utilization ratio and makes lighter and smaller devices to become possible. One representative case is replacing mesoporous carbon particle with graphene for compact energy storage, e.g., the state-of-the-art graphene electrode for supercapacitors exhibits a volumetric capacitance of 200 F cm^{-3}, twice larger than that of commercial activated carbon. [5] These materials also exhibit distinct and unusual properties with their thickness decreasing down to atomic thin. For instance, many 2D materials like graphene and phosphorene exhibit the unique quantum hall effect and ultrahigh intrinsic carrier mobility that are essential for high-performance electronic devices.[6] 2D materials also possess an extraordinary optical response (e.g., absorption and photoluminescence) due to spatial confinement and reduced dielectric screening, which makes them an ideal candidate for optical nanodevices.[7] Thanks to these intriguing properties, 2D materials have attracted considerable interest across scientific and industrial communities, and have been considered as a key component to advance next-generation technologies (e.g., quantum computing and terahertz optoelectronic devices).[8].

Although the research on the 2D materials is still in the preliminary stage and just starts massive industrialization, the next stage of research, nanomodification of 2D materials, has already begun to lead the future material revolutions in many key areas. Nanomodification involves

---

* Corresponding author.
E-mail address: Qiong.Nian@asu.edu (Q. Nian).

https://doi.org/10.1016/j.nantod.2024.102162
Received 7 September 2023; Received in revised form 1 January 2024; Accepted 9 January 2024

heteroatom doping,[9] phase tuning,[10] defect engineering [11] interlayer engineering,[12] and 2D heterostructure design,[13] which can be used to enlarge specific surface area, tune physical and chemical properties, and impart new properties. For instance, doping graphene with nitrogen atoms can enhance the electrical conductivity and provide additional pseudocapacitance to enable better energy storage properties.[14] Intercalation of metal ions into MoS_2 can induce lattice distortion and structural modulation to trigger phase transition from semiconductive 2 H to metallic 1 T phase.[15] Assisted with such nanomodification, the intrinsic structure of 2D material can be tailored to largely improve the crucial properties for broadening applications and performance enhancements.

Currently, an increasing number of studies show that after creating nanoholes on the basal plane, the 2D materials can be more versatile to realize various functions and exhibit better performance compared to their counterparts. For example, in comparison to the non-holey graphene as membrane material for water purification, the holey graphene showed 16.5 times enhancement in water permeance while maintaining a similar salt rejection capability.[16] Another case is by comparing the non-holey and holey $Ti_3C_2T_x$ film for Li-Ion storge application, the holey $Ti_3C_2T_x$ demonstrated a 58.2% improvement in Li-Ion storage capacity and significantly enhanced cycling stability.[17] With nanoholes, these holey 2D materials possess much more mass transport channels, which are significant for the applications relying on the mass exchange process, e.g., batteries,[18] biosensors,[19] and desalination devices [20]. Moreover, the edge-sites of the nanoholes can exhibit much higher electrochemical activity than the in-plane sites to further improve the performance.[21] Driven by these advantages, a variety of approaches have been developed to obtain the holey 2D materials. Among them, chemical etching is the most used method to manufacture holey 2D nanomaterials and the most potential one for large-scale manufacturing. More precise approaches based on beaming with different sources like electrons and ions are preferred to be used in physics applications. Other advanced methods including calcination, template-directed synthesis, and bottom-up chemical synthesis have also emerged in recent years due to the fast growth in this field.

There are several review papers of holey 2D nanomaterials published in literature, including holey 2D materials for electrochemical energy storge[22], holey graphene [23] and its applications in electrochemical energy storage [18,24], and holey graphene-based nanocomposites [25]. To further promote the advance of this holey 2D material in not only electrochemical energy storage but also other areas, and help summarize current manufacturing methods, this review paper focuses on two main topics. The first topic (Section 2) is on the advantages of a variety of holey 2D nanomaterials and their improvements in a broad range of applications. The second topic (Section 3) involves the summary and comparison of various manufacturing approaches of holey 2D nanomaterials and the corresponding mechanisms. In Section 4, we share our perspectives on the future development of holey 2D nanomaterials and analyze the challenges and remaining issues with the expectation to provide effective insights in this area and inspire new ideas and conceptions for the researchers from different areas.

Holey 2D nanomaterials and their applications

In terms of holey 2D materials, the first question often is why we need them over their non-holey versions or what are the benefits by introducing the in-plane nanoholes. The answer can be multifold. First, each 2D material has its distinct advantages and disadvantages, and some of the disadvantages cannot be circumvented and gradually become the bottleneck for the further development of this 2D material. Such issues include nanosheet restacking, lacking mass transport channels, low electrochemical activity, etc. The holey 2D materials can be a good solution. Second, one can look at the potential of holey 2D materials in broadening the versatility or application range by providing a whole new dimension of structural diversity. They enable obtaining the desired properties for distinctive applications by playing with multiple structural variations, such as i) the diameter, population, and distribution pattern of nanoholes; ii) the number, alignment, and heteroatom doping of the edge-site atoms around nanoholes; iii) the interactions between nanoholes and foreign nanomaterials. Currently, as shown in Fig. 1, the research on this topic covers the field of supercapacitors, metal-ion batteries, metal-air batteries, metal-CO_2 batteries, biosensors, drug carriers, water disinfection, desalination, thermocells, heavy metal detection, water splitting, and electronics. It is expected that more intriguing findings can be revealed soon.

Because of the above reasons, an increasing number of 2D materials are joining the holey family, which can be further categorized into four groups. The first is holey graphene, which has the most articles among all. The second group includes the holey 2D transition metal compounds, such as transition metal oxides (TMOs), lithium transition metal oxides (LMOs), transition metal carbides and nitrides (MXene), transition metal dichalcogenides (TMDCs), and layered double hydroxides (LDHs). The third group is composed of the holey graphene-like materials, such as h-BN, phosphorene, nitrogenated carbon nanosheet. The last group contains the rest studies in this field exploring the potential of other holey 2D structures, including silicon, amorphous carbon, etc. The following part of Section 2 will demonstrate the characteristics and advantages of each group of holey 2D materials and their contributions to the performance of various applications in detail.

Graphene

Graphene has become one of the most revolutionary materials in recent decades due to its attractive properties, such as high strength and stiffness, high electrical and thermal conductivity, and high specific surface area, embarking a new era of 2D nanomaterials and leading the surging development of nanotechnologies [26]. Due to the superior material parameters, graphene has great potential to replace many existing materials in various fields such as electronics, photonics, electrochemical and biochemical devices, etc. Besides, the single-atom thickness of graphene makes it very versatile to fit in various applications by encapsulating, wrapping, sandwiching, directly mixing with, or stacking as building blocks with other materials to enable diverse nanostructures of both high performance and complex functions.[27].

Holey graphene is the graphene with holes on its basal plane (Fig. 2). The holes are mostly in nanoscale or sub-nanoscale and can be randomly or periodically distributed. The nanoholes allow ions and molecules directly passing through the basal plane of a graphene sheet, which interests the researchers in the fields involving mass transport to use this characteristic to improve the basic kinetics of various applications. In addition, the nanoholes change the electronic structure of pure graphene, introducing a handle to tune the electronic properties of graphene and making it more useful in the semiconducting applications. Besides the nanoholes themselves, the carbon atoms on the edge-sites around the nanoholes are also an important feature of holey graphene. They are more chemically active than those in the defect-free regions and better in charge transport, and ever more they can be doped or attached by heteroatoms, functional groups, nanoparticles, or nanostructures to obtain distinct properties while retaining the superior properties of pure graphene. The versatility of the edge-sites drives the development of various applications using holey graphene involving electrochemistry, catalytic chemistry, biochemistry, electronic, optoelectronic, thermoelectric, etc.

Although the research of holey graphene does not have a long history, it is seen a significant surge of progresses in recent years. This material was first prepared by J. Bai et al. [28] in 2010 aiming at providing a semiconductive graphene structure which could replace the graphene nanoribbon in field-effect transistors. The material was referred as the graphene nanomesh at that time because of the pattern of the nanoholes. The periodic distribution of nanoholes with controlled diameters and neck widths were significant factors to the in-plane

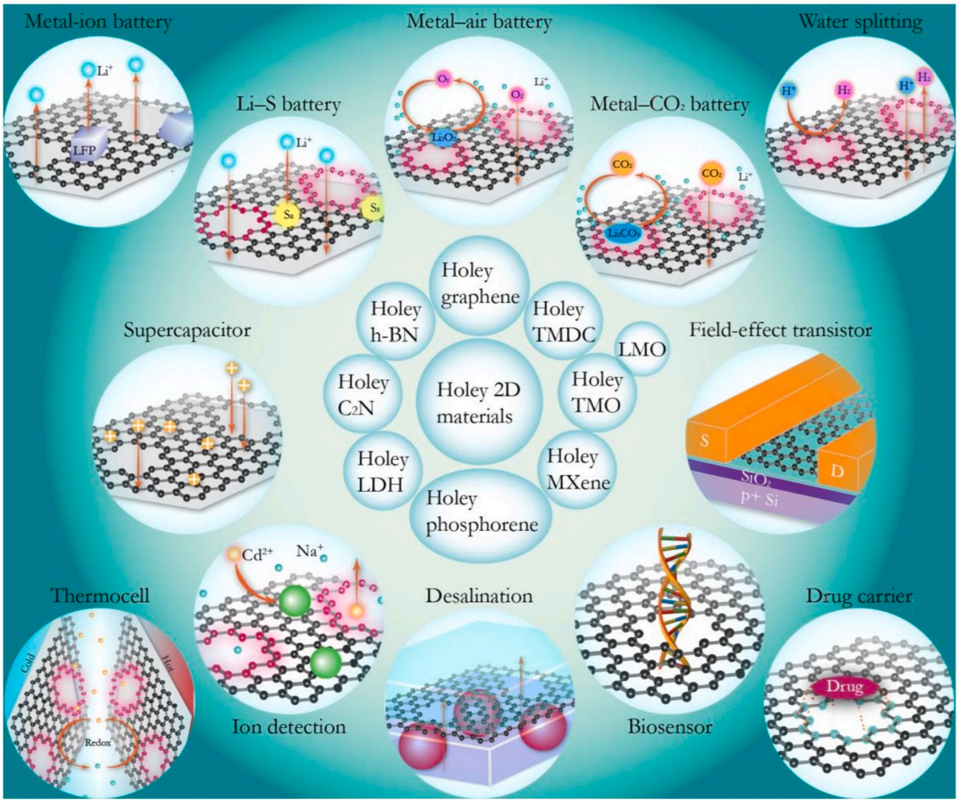

Fig. 1. Schematic diagram of various types of holey 2D nanomaterials and various applications. Against their non-holey counterparts, they have intrinsic advantages in mass transportation and diffusion.

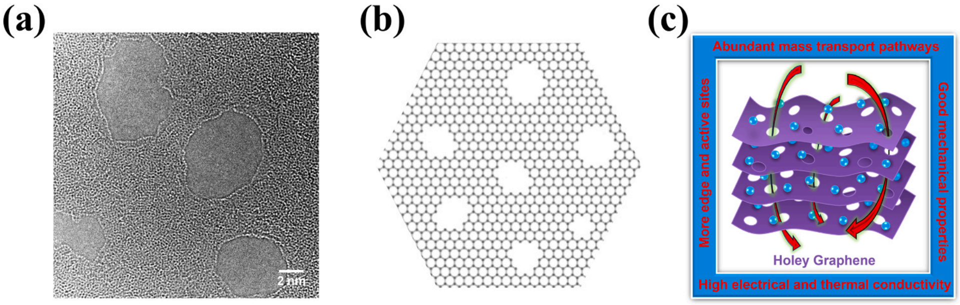

Fig. 2. Holey graphene: (a) TEM image, (b) structure and (c) fundamental properties.

charge transport of graphene in 2D field-effect transistors. In 2011, X. Zhao et al. [29] first proposed making graphene holey for the energy storage devices with enhanced performance, and they demonstrated that compared to that of pure graphene, the faster cross-plane ion diffusion brought by the nanoholes overcame the restacking issue of graphene and resulted in better lithium-ion storage and power delivery. These two studies enlightened researchers to further discover the great potential of holey graphene to replace pristine graphene in various fields and embarked the exponential growth of the studies on this fascinating material.

Electrochemical energy storage

Electrochemical energy storage, including supercapacitors and batteries (such as lithium-ion batteries, sodium-ion batteries, mixed metal-ion batteries, lithium–sulfur batteries, etc.), is a major field that graphene has been broadly used in research and shown great potential in industry. Naturally, the studies on holey graphene fast spread in this field, and many advantages of this material over its predecessor are quickly revealed. Obvious performance improvements can be observed from the Ragone plot of electrochemical energy storage applications based on holey and pristine graphene (Fig. 3**a**). Generally, besides the merits succeeded from pristine graphene, such as high mechanical strength and electrical and thermal conductivity, holey graphene can further improve the electrochemical performance of the final device by enhancing the specific surface area, specific capacitance or capacity, electrochemical activity, charge transfer rate, and ion diffusion rate. In the electrode, holey graphene can be used as an active material, a conductive additive for other active materials, or a 3D framework in the form of aerogels to provide hierarchical porous structures. For comparison, we collected the related articles on various batteries, supercapacitors, and hybrid energy storge devices as many as possible and summarized the reported crucial properties of the electrode materials based on holey graphene in Table 1 and Table 2. In the following part of Section 2.1.1, we first discuss the improvement of each energy storage application brought by holey graphene and then detail the microscopic improvement mechanisms.

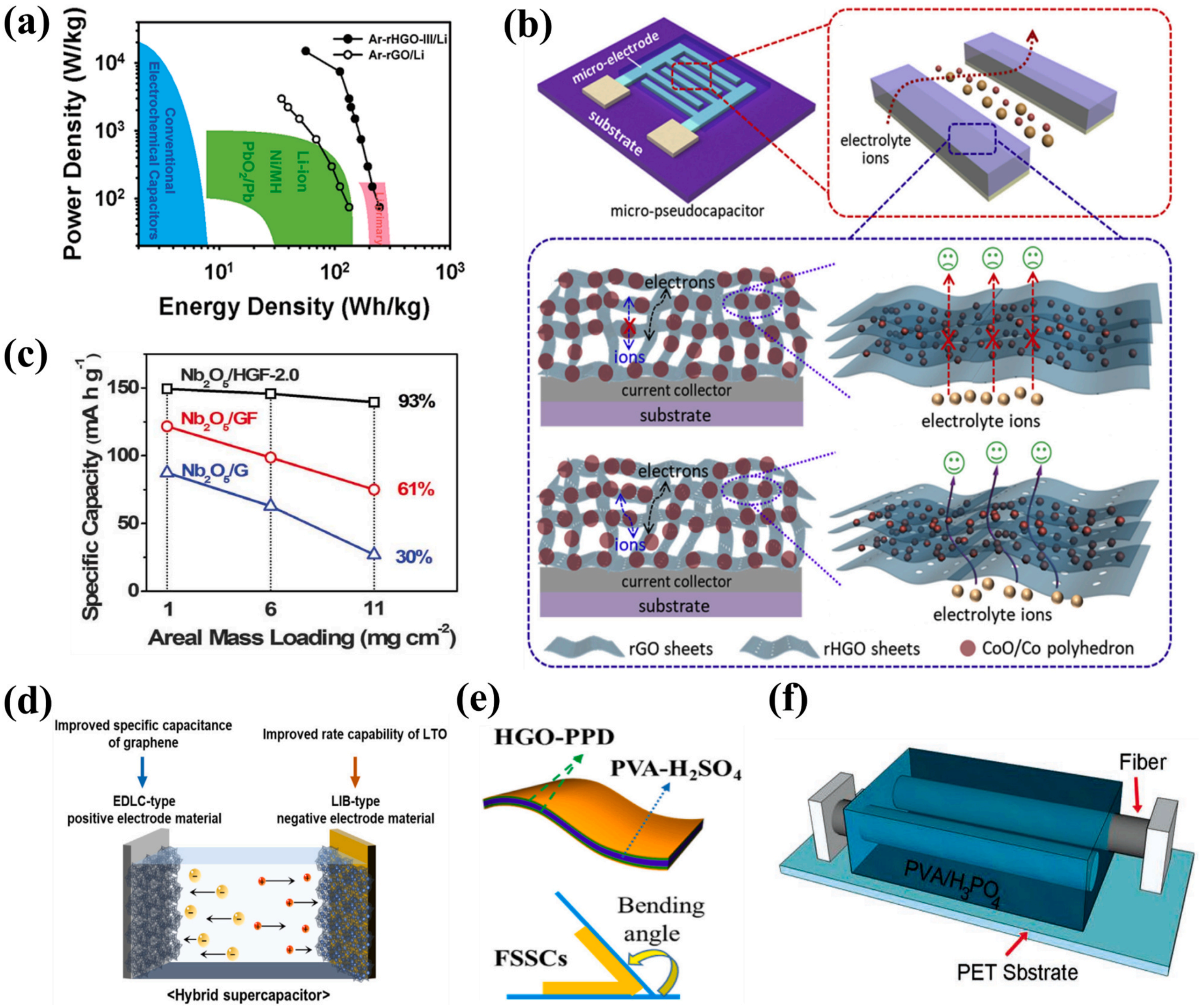

Fig. 3. Schematics showing holey graphene in energy storage applications: (a) Ragone plot of electrochemical energy storage devices based on holey graphene vs. pristine graphene (Reproduced with permission.[29] Copyright 2011, ACS.); (b) micro-supercapacitor (Reproduced with permission.[55] Copyright 2019, Elsevier.); (c) effect of areal mass loading on capacities of Li-ion batteries (Reproduced with permission.[56] Copyright 2017, Science.); (d) hybrid supercapacitor (Reproduced with permission.[49] Copyright 2019, Elsevier.); (e) flexible solid-state supercapacitor (Reproduced with permission.[35] Copyright 2019, Elsevier.); (f) fiber-based micro-supercapacitor (Reproduced with permission.[37] Copyright 2018, Wiley).

Holey graphene-based supercapacitors. Supercapacitors highlight the advantage in the power delivery due to the rapid charge and discharge processes on the electrode and has become a complementary energy storage solution for batteries, which show difficulty in further promoting the power density. Nevertheless, supercapacitors generally have relatively low energy storage, and therefore the improvement of the energy density is vital to promote their application.

Based on the charging mechanism, supercapacitors can be divided into three groups: electrical double-layer capacitors (EDLCs), pseudocapacitors, and hybrid capacitors [30]. In EDLCs, the charging is fulfilled by the electrostatic adsorption of electrolyte ions on the electrode surface without exchanging charges (i.e., the non-faradaic process). Pseudocapacitors are charged by the valance state changes of the electrode material (i.e., the faradaic process), which exchanges charges with the electrolyte through redox reactions. The different charging mechanisms generally make EDLCs more reversible and possessing longer cycling life and pseudocapacitors less reversible but having larger specific capacitance. Thus, the requirements of the two supercapacitors for the electrode materials are also different. For EDLCs, the specific surface area of the electrode material is a predominant factor affecting the specific capacitance, while for pseudocapacitors, the electrochemical activity, which can be characterized by charge transfer resistance, of the electrode material is also a significant factor besides the specific surface area. Hybrid capacitors have a series of variants, which can combine the above two charging mechanisms or even couple with the metal-ion battery electrode to introduce the crystalline-confined charging process, e.g., lithium-ion capacitors.

In terms of holey graphene, both the EDLC and pseudocapacitor mechanisms are activated, taking account of the larger accessible surface area enabled by the nanoholes and the lower charge transfer resistance contributed by the edge-site atoms around nanoholes (Fig. 3**b-f**). Pseudocapacitance can be further enhanced by heteroatom doping, functional group modification, polymer modification, transition metal compound incorporation, etc. The electrical conductivity of the supercapacitor electrode is another vital role for the performance. To ensure the high conductivity, cross-linking and incorporating conductive additives, such as carbon nanotubes and pure graphene, are effective approaches.

To preliminarily evaluate the energy density of a supercapacitor, the specific capacitance of the electrode material is a major indicator. The

Table 1
Supercapacitor properties of holey graphene.

Material	Surface area [$m^2\ g^{-1}$]	Capacitance [F g^{-1}]	Energy density [Wh kg^{-1}]	Power density [W kg^{-1}]	Cycling life[a])
Holey graphene [57]	658 (471)	45 (40) at 3 A g^{-1}	12 ^{V} (~2 ^{V}) SSC	\	96% @ 100,000
Holey graphene [58]	~600–700 (~500)	43 at 0.25 A g^{-1}	3.8–9.1 SSC	310–974 SSC	65% @ 2000
Holey graphene [47]	\	226 (104) at 4 mA cm^{-2}	9.25–10.37 SSSC	1388–4166 SSSC	93% @ 5000
Holey graphene [31]	750 (550)	330 (235) at 5 mV s^{-1}	124 (86) at 25 °C; 140 at 60 °C SSC	18.0 (17.5) at 25 °C; 52.5 at 60 °C SSC	90% @ 2000
Holey graphene [46]	42.4	30 ^{V} at 0.05 mA cm^{-2}	2.43–4.24 ^{V} MSC	120–21,840 ^{V} MSC	88.6% @ 10,000
Holey graphene[59]	763 (552)	251 (188) at 1 A g^{-1}	\	\	94% @ 6000
Holey graphene[60]	592 (520)	211 (142) at 0.5 A g^{-1}	\	\	99.9% @ 10,000
Holey graphene[38]	347 (~250)	110 or 165 ^{V} at 5 A g^{-1}	\	\	85.5% @ 7000
Holey graphene [32]	560.8 (254.6)	329 (208) at 0.5 A g^{-1}	\	\	\
Holey graphene [61]	\	137 (33.8) at 0.5 A g^{-1}	19.4	280	\
Holey graphene [62]	261 (210)	253 (158) at 1 A g^{-1}	\	\	91% @ 50,000
Holey graphene [49]	290 (250)	243 (180) at 0.1 A g^{-1}	43.1–117.3 HSC	100–19,700 HSC	81.7% @ 2000
Holey graphene aerogel [63]	528 (305)	178 (151) at 0.2 A g^{-1}	\	\	\
Holey graphene aerogel [64]	398	451 at 1 A g^{-1}	\	\	95.6%@ 2000
Holey graphene hydrogel[44]	1330 (990)	283 (205) at 1 A g^{-1}	116 (77) or 86 ^{V} Organic SSC	\	94% @ 20,000
Holey graphene framework [33]	BET 830 (260); MB 1560 (1030); BET 810 after compression	310 (208) at 1 A g^{-1} in aqueous solutions; 298 at 1 A g^{-1} in EMIMBF$_4$/AN	112 or 79 ^{V} Aqueous SSC; 123 or 87 ^{V} Organic SSC	10^2–10^3 SSC	91% @ 10,000
Holey N-graphene [65]	446	318.3 at 0.5 A g^{-1}	60.5 SSC	900 SSC	98.4% @ 10,000
Holey N-graphene [66]	1216 (630)	343 (296) at 0.3 A g^{-1}	\	\	> 100% (~80%) @ 10,000
Holey N-graphene [67]	\	126 at 1 A g^{-1}	53.5 SSC	17500 SSC	91%@ 2000
Holey N,S-graphene aerogel [39]	395 (183)	807 ^{V} (556^{V}) at 1 mA cm^{-2}	0.409 ^{V} SSSC	102 ^{V} SSSC	95.4% @ 1100
Holey N,S-graphene hydrogel [68]	370.4	346 at 1 A g^{-1} or 242 ^{V}	24.6 SSC	415.4 SSC	93.8%@ 10,000
Holey N,F-graphene composite film [69]	196	580 at 0.5 A g^{-1} (828 ^{V})	\	\	87.8%@ 2000
Holey B,N,P-graphene hydrogel [34]	980 (498)	362 (318) at 1 A g^{-1}	38.5 SSC	83,000 SSC	81.3% @ 50,000
p-phenylenediamine doped holey graphene [40]	67.32 (26.88)	300 (235) or 516 ^{V} (357.2 ^{V}) at 0.5 A g^{-1}	2.18–2.72 ^{V} FSSC	146.5–3313.6 ^{V} FSSC	88% @ 12,000
p-phenylenediamine doped holey graphene [35]	98.34 (83.56)	375.5 (311.8) at 0.5 A g^{-1}	5.59–11.71 FSSC	249–20,110 FSSC	75% @ 10,000
Polyaniline@holey N-graphene [36]	\	746 (618) at 1 A g^{-1}	24.7 SSC	329.5 SSC	74% @ 2000
Polyaniline@holey graphene framework [41]	185	730 or 1058 ^{V} at 0.5 A g^{-1}	26.5 ^{V} SSC	175.3 ^{V} SSC	81.5% @ 5000
aramid/holey graphene /polyaniline hydrogels [70]	44.2	200 at 0.2 A g^{-1}	\	\	98.9%@ 2500
Polypyrrole@holey graphene aerogel [71]	278 (131)	418 at 0.5 A g^{-1}	\	\	74% @ 2000
CNT@holey graphene [32]	\	557 at 0.5 A g^{-1}	\	\	90% @ 5000
CoO/Co@holey graphene [55]	\	241.3 (136.6) mF cm^{-2} at 0.5 A g^{-1}	\	\	91% @ 11,000
Co_3O_4 @holey graphene aerogel [72]	149.84	1783 at 0.5 A g^{-1}	42.6 ASC	775 ASC	81.1% @ 10,000
Co_3O_4 @holey graphene network [73]	26	2714 at 1 A g^{-1}	165 SSC	600 SSC	92%@ 10,000
$NiCo_2O_4$ @holey graphene framework [74]	98.7	1118 at 1 A g^{-1}	9.37 SSC	250 SSC	95.04%@ 5000
Holey graphene composite framework [75]	172.3	526 at 0.1 A g^{-1}	\	\	90.3%@ 5000
MnO_2 @holey graphene aerogel [76]	134.8 (39.7)	192.2 at 0.5 A g^{-1}	\		79% @ 5000
MnO_2 @holey graphene film [77]	241.8	108 ^{V} at 1 mA cm^{-2}	3.2 mWh cm^{-3} SSC	5.9 mW cm^{-3} SSC	93.7 @ 10,000
Holey graphene/Ni(PA)$_2$ paper [78]	\	738 at 1 A g^{-1} or 747 ^{V} at 1 A cm^{-3}	23.7 ^{V} ASC	632 ^{V} ASC	83.3%@ 10,000
V_2O_5 @holey graphene aerogel [79]	417 (149) for HGA (GA); 76 (35) for composite	316 (268) for HGA (GA); 264 for composite	\	\	98% for HGA; 85% @ 1000
RuO_2 @holey graphene fiber [37]	\	693 or 1054 ^{V} at 2 mV s^{-1}	15.9–27.3 ^{V} FMSC	147.7–2954.1 ^{V} FMSC	78.7% @ 10,000
MoS_2 @holey graphene fiber [48]	\	421 ^{V} (141 ^{V}) at 5 mV s^{-1}	4.1–8.2 ^{V} FMSC	40–2000 ^{V} FMSC	92% @ 3000
MXene@holey graphene [42]	68	438 or 1445 ^{V} at 2 mV s^{-1}	31.3–38.6 ^{V} SSC	206–8245 ^{V} SSC	93% @ 10,000
MXene@holey graphene hydrogel [80]	269.2	415 or 597 ^{V} at 1 A g^{-1}	15.4 or 22.2 ^{V} SSC	288.7 SSC	91.7%@ 10,000

ASC: asymmetric supercapacitor; SSC: symmetric supercapacitor; FSSC: flexible symmetric supercapacitor; MSC: micro-supercapacitor; FMSC: fiber-based micro-supercapacitor; SSSC: solid-state supercapacitor; HSC: hybrid supercapacitor.

[a] Capacity or capacitance retention percentage at certain cycles (numbers after @).

^{V}Volumetric properties: the unit of g^{-1} and kg^{-1} should be replaced by cm^{-3} and L^{-1}, respectively.

highest reported specific capacitance of pure holey graphene is 330 F g^{-1} at a scan rate of 5 mV s^{-1} in the butylmethylpyrrolidinium–dicyanamide ionic liquid electrolyte, about 1.4 times that of pristine graphene (235 F g^{-1})[31]. In aqueous electrolytes, the highest record of pure holey graphene is 329 F g^{-1} at a current density of 0.5 A g^{-1}, about 1.5 times that of pristine graphene (208 F g^{-1}) [32]. In organic electrolytes, the highest record of pure holey graphene is 298 F g^{-1} at a current density of 1 A g^{-1} in the EMIMBF$_4$/AN electrolyte [33]. Doping holey graphene with heteroatoms, such as B, N, S, P, etc., the specific capacitance can be improved mostly because of the higher

Table 2
Battery properties of holey graphene.

Material	Surface area [$m^2\ g^{-1}$]	Capacity [$mAh\ g^{-1}$]	Charge transfer resistance [Ω]	Cycling life[a]
Holey graphene [49]	290 (250)	170.4 (169.4) at 0.1 $A\ g^{-1}$; 117.0 (5.6) at 30 $A\ g^{-1}$;	\	81.7% @ 2000
Holey graphene [29]	15 (25)	819 (504) at 0.14 C	516 (551)	100% @ 1000 at 26.6 C
Holey graphene [51]	84 (156)	365 (251) at 0.1 $A\ g^{-1}$	\	45% @ 3000
Holey graphene [81]	457 (275) BET 945 MB	423 (164) at 0.1 $A\ g^{-1}$	37.4	95% @ 100
Holey Fe,N-graphene [82]	370.5 (202.5)	1255 at 0.1 C	33.07 (40.14)	75.1% (64.3%) @ 300
Holey B-graphene [83]	626.9	19698 at 0.1 $A\ g^{-1}$	\	100% @ 120
Holey B, N-graphene [84]	949	15340 at 0.1 $A\ g^{-1}$	\	90%@ 117
Holey N-GO aerogel [52]	260 (74)	446 (153) at 0.1 $A\ g^{-1}$	\	40% @ 2000
Holey graphene on Cu foil [85]	\	114 at 20 $A\ g^{-1}$	\	100% @ 1000
$LiFePO_4$ @holey graphene [86]	183.1	1507[b] at 0.1 C	8.75 (11.76)	78%@ 500
Fe_2O_3 @holey graphene [87]	157	923 at 0.1 $A\ g^{-1}$	\	
Co_3O_4 @holey graphene [50]	130.1	631 at 10 $A\ g^{-1}$; 1015 at 0.2 $A\ g^{-1}$	\	89.6% after 100
Co_3O_4 @holey graphene aerogel [72]	149.84	173.3 at 0.5 $A\ g^{-1}$	0.45	81.1% @ 10,000
$TiNb_2O_7$ @holey graphene[88]	181	276 at 0.05 $A\ g^{-1}$	\	90.2% @ 3000
MnS@holey graphene [89]	41	870.5 at 0.1 $A\ g^{-1}$	48.68	100% @ 200
MoS_2 @holey graphene [90]	52	1084 at 0.2 $A\ g^{-1}$	\	94.5% @ 2000
MoS_2 @holey graphene [91]		596 at 0.1 $A\ g^{-1}$; 912 at 0.1 $A\ g^{-1}$ with super P; 1200 at 0.5 $A\ g^{-1}$ after 1000 cycles with super P	71.8	133% @ 1000
$Li_4Ti_5O_{12}$ @holey graphene [92]	154.2	200 or 161 ^{V} at 0.035 $A\ g^{-1}$	17.1 (71.1)	84% @ 1000
$FePO_4$ @holey graphene framework [93]	96	156 at 0.5 C	48.6	95%@ 500
$NiCo_2O_4$ @holey N-graphene [94]	\	510 (221) at 0.1 $A\ g^{-1}$	63 (128)	85.7% @ 500
Mo_2C@holey N-graphene [95]	70.8 (29.2)	1221 at 0.1 $A\ g^{-1}$	314.5	58% @ 300
Nb_2O_5 @holey graphene aerogel [56]	83	139 at 10 C		90% @ 10,000
Fe_3O_4 @holey graphene aerogel [96]	204 (242)	1107 (862) at 0.1 $A\ g^{-1}$	33.42 (82.38)	85.4% @ 100
V/N quantum dots@holey graphene matrix [97]	272.5	1320 at 0.1 C	20	99.95% @ 500
Holey graphene/ polyacrylonitrile sulfur composite [98]	68.4	1178.9 at 0.05 C	19.4	81.5% @ 1500
Holey graphene/ polyaniline sulfur [99]	\	1082 at 0.5 C	39.6	85.3% @ 500
Holey graphene/ polymer framework [100]	\	135.8 at 1 C	35.5	71%@ 300

[a] Capacity or capacitance retention percentage at certain cycles (numbers after @).

[b] Based on the weight of sulfur.

contribution from the pseudocapacitance, which provides more energy storage chemically through the redox reactions between the electrode material and electrolyte ions. The highest reported value of the heteroatom-doped holey graphene is 362 $F\ g^{-1}$ at a current density of 1 $A\ g^{-1}$ (B, N, and P co-doped holey graphene), while under the same condition of doping, the non-holey version showed a lower value of 318 $F\ g^{-1}$[34]. Incorporating with crosslinking molecules, such as *p*-phenylenediamine, to prevent the restacking of graphene sheets, the specific capacitances of holey and pristine graphene are 375.5 and 311.8 $F\ g^{-1}$ at a current density of 0.5 $A\ g^{-1}$, respectively [35]. The addition of carbon nanotubes can achieve the same goal while enhancing the electric conductivity of the electrode, bringing a specific capacitance of 557 $F\ g^{-1}$ at a current density of 0.5 $A\ g^{-1}$ [32]. Some polymers including polyaniline and polypyrrole can contribute pseudocapacitance to enhance the specific capacitance with the highest reported value of 746 $F\ g^{-1}$ at a current density of 1 $A\ g^{-1}$, higher than that of the non-holey version reported in the same paper (618 $F\ g^{-1}$). [36] Transition metal compounds, including oxides, dichalcogenides, MXene, are employed to endow higher pseudocapacitance to holey graphene, and the highest reported specific capacitance for these nanocomposite electrodes is 693 $F\ g^{-1}$ at a scan rate of 2 $mV\ s^{-1}$, obtained by the RuO_2-incorporated holey graphene fiber.[37] Due to the ability of holey graphene in realizing the electrodes with higher packing densities without much performance sacrifice, the volumetric specific capacitances of holey graphene-based electrode materials are also significantly higher than those of non-holey versions. The highest reported volumetric specific capacitances of pure,[38] heteroatom-doped,[39] crosslinked, [40] polymer-incorporated,[41] and transition metal compound-incorporated[42] holey graphene are 165, 807, 516, 1058, and 1445 $F\ cm^{-3}$, respectively.

Compared to the electrode performance, the performance of the supercapacitor devices is closer to the real application and generally evaluated by the energy and power densities, which are more reliable than the specific capacitance measured from a single electrode and more comparable across different papers due to the generally acknowledged calculation method [43]. Based on the distinct requirements on the application end, the holey graphene-based supercapacitors can be further categorized into more groups, including the symmetric supercapacitor (SSC), asymmetric supercapacitor (ASC), flexible symmetric supercapacitor (FSSC), solid-state supercapacitor (SSSC), micro-supercapacitor (MSC), fiber-based micro-supercapacitor (FMSC), and hybrid supercapacitor (HSC).

The SSC is the most common supercapacitor device and made of two identical electrodes with a separator between them. The highest reported energy density in holey graphene-based SSCs is 124 $Wh\ kg^{-1}$ at a power density of 18.0 $W\ kg^{-1}$, about 1.4 times that of pristine graphene (86 $Wh\ kg^{-1}$ with 17.5 $W\ kg^{-1}$).[31] The similar magnitude of energy densities is reported by Y. Xu et al. [44] Generally, without trading off the power density and keeping it at higher than 10^3 $W\ kg^{-1}$, the energy densities of the holey graphene-based SSCs are in the magnitudes of

10^0–10^1 Wh kg^{-1}. Under a ultrahigh level of power densities (10^4 W kg^{-1}), the highest reported energy density is 38.5 Wh kg^{-1} at a power density of 83,000 W kg^{-1} using 1 M EMIMBF$_4$/AN electrolyte.[34] In terms of volumetric properties, the highest volumetric energy density of the holey graphene-based SSCs is 87 Wh L^{-1} with a volumetric power density of 10^2 W L^{-1} achieved in an EMIMBF$_4$/AN electrolyte with an ultrahigh electrode density of 10 mg cm^{-2} [33]. When the volumetric power density of the holey graphene-based SSC is higher than 10^3 W L^{-1}, the highest reported volumetric energy density is 31.3 Wh L^{-1} using the MXene/holey graphene nanocomposite electrode [42].

Different from an SSC, an ASC is generally composed of an EDLC electrode (e.g., activated carbon and mesoporous carbon spheres) and a pseudocapacitive electrode (e.g., MnO_2 and Co_3O_4) aiming to provide a better energy density than an SSC while maintaining a favorable power density. Graphene was often used as the conductive additive in the pseudocapacitive electrode and a framework material with high specific surface area, and the graphene-based nanocomposite electrode generally exhibited superior performance than the electrode solely made of pseudocapacitive metal oxides.[45] Holey graphene can be used in the same manner with the expectation of bringing better performance than pristine graphene due to the faster ion transport behavior. However, as far as we know, there is no study on the holey graphene-based ASC yet.

An FSSC is a flexible version of an SSC and has become increasingly demanded with the fast development of the portable, wearable, and foldable electronic devices. Besides the energy and power densities, the performance stability of an FSSC under high-angle distortion is a key factor to evaluate the electrode material. 2D nanomaterials, especially graphene, have natural advantages in terms of the flexibility. Thus, holey graphene is highly promising in this field. P. Du et al. [35] reported an holey graphene-based FSSC. The cyclic voltammetry of the FSSC showed little changes under bending and twisting, as well as after restoring to its original flat status. After bending to 180° for 250 cycles, the device kept 85% of its initial capacitance. Z. Pan et al.[34] fabricated a FSSC using the B, N, and P co-doped holey graphene hydrogel as the electrode, which showed little changes in the cyclic voltammetry under bending at 60°, 120°, and 180 °, and the device retained 91.6% of its initial specific capacitance after 20,000 cycles under 180 ° bending. Y. Xu et al. [44] reported an holey graphene FSSC, which also negligible changes in the cyclic voltammetry under bending with curvature radii of 2–12 mm, and the specific capacitance retained 90% after 20,000 cycles under 2-mm bending.

Because of using solid-state electrolytes (mainly polymer-based gels), the SSSC not only inherit the high power density of the SSC and also avoid the leakage of harmful electrolytes, thus making them promising in wearable devices and appliable in other subgroup of supercapacitors such as FSSCs [34,35,44] and MSCs [46]. A. C. Lokhande et al. [47] fabricated a holey graphene-based SSSC using poly (vinyl alcohol) (PVA)/KOH gel electrolyte, and the device exhibited energy densities of 9.25–10.37 Wh kg^{-1} at power densities of 1388–4166 W kg^{-1}. M. Kotal et al.[39] fabricated an SSSC using the sulfur and nitrogen co-doped holey graphene aerogel as the electrode and PVA/LiCl gel as the electrolyte. The holey graphene SSSC exhibited an areal energy density of 17.4 μWh cm^{-2} at a power density of 4457 μW cm^{-2}, higher than that of the non-holey version (11.1 μWh cm^{-2} at 3134 μW cm^{-2}).

MSCs are the thin-layer energy storage devices possessing many advantages over micro-batteries and have great potential as the energy storage component of the fast-developing wearable electronics. An MSC is composed of alignments of two or more 2D micro-electrodes deposited or printed on a substrate. Holey graphene offers extraordinary areal energy density because the holey structure allows the relatively thicker electrode films without compromising the rate performance while maintaining the flexibility. A. Lu et al.[46] reported a holey graphene MSC using the PVA/H_2SO_4 gel electrolyte, exhibiting volumetric energy densities of 2.43–4.24 Wh L^{-1} at a power density of 120–21,840 W L^{-1}, and the device retained 88.6% of its initial specific capacitance after 10,000 cycles.

FMSCs are the state-of-the-art fiber device that can be further fabricated as the clothes and textiles providing energy for the wearable electronics or storing energy from the thin-film energy harvest devices. Holey graphene is an excellent material for this application due to the need of high packing density (or mass loading) and high rate capability at the same time. S. Zhai et al.[37] reported an FMSC using the RuO_2 nanoparticle (Ru content: 42.5%) decorated holey graphene fiber as the electrode. The FMSC exhibited high volumetric energy densities of 15.9–27.3 Wh L^{-1} at the power density of 147.7–2954.1 W L^{-1}, and the specific capacitance of the device retained 78.7% of its initial value after 10,000 cycles. C. Wang et al.[48] fabricated an FMSC using the MoS_2 decorated holey graphene fiber electrode which has a core of graphite fiber bundles. The FMSC showed energy densities of 4.1–8.2 Wh L^{-1} at the power density of 40–2000 W L^{-1}, and the device retained 92% of its initial specific capacitance after 3000 cycles.

An HSC is similar to an ASC, but the difference is that the latter often refers to a capacitor combining an EDLC electrode and a pseudocapacitive one, while the former generally specifies a battery-like capacitor, which has well-defined anode and cathode, a battery-type one and a capacitive one. Holey graphene was proved effective in enhancing the performance of both of the electrodes in an HSC. Besides the improvement of the capacitive electrode (as discussed above), holey graphene has great potential in improving the battery-type electrode due to its contribution in the ion diffusion rate, which is a major limitation of the batter-type electrode towards higher power capability. J. H. Jeong et al. [49] fabricated an HSC using a holey graphene cathode and a $Li_4Ti_5O_{12}$/holey graphene anode, and the device exhibited energy densities of 43.1–117.3 Wh kg^{-1} at power densities of 100–19,700 W kg^{-1}. The simultaneous improvements of the energy and power densities are attributed by the high specific capacitance of the holey graphene cathode and the high-rate capability of the holey graphene-based anode, and these values were all higher than those with the non-holey crumpled rGO and its nanocomposite. The HSC retained 89.7% and 81.7% of its initial specific capacitance after 1000 and 2000 cycles at 2 A g^{-1}.

Holey graphene-based metal-ion batteries. In metal-ion batteries, holey graphene exhibits better specific capacity, rate capability, and cycling performance. D. Wu et al.[50] report a nanocomposite Li-ion battery electrode composed of hollow Co_3O_4 particles and holey graphene sheets, which exhibits an improvement of about 1.5 times in the specific capacity (631 mAh g^{-1}) at a high current density of 10 A g^{-1} compared to the electrode using regular graphene (406 mAh g^{-1}). After 250 cycles at 0.2 A g^{-1}, the discharge capacity of the former is about 1.3 times higher than that of the latter (1015 and 762 mAh g^{-1}, respectively).

Holey graphene has also been applied as the electrode material in Na-ion batteries for better electrochemical performance. It was reported [51] that when utilized as Na-ion battery anode materials, holey rGO exhibited a specific capacity of 365 mAh g^{-1} at 0.1 A g^{-1}, 1.45 times higher than that of non-holey rGO (251 mAh g^{-1}). Holey rGO also demonstrated a significantly improved rate performance with a specific capacity of 131 mAh g^{-1} at a high current density of 10 A g^{-1}, while non-holey rGO only had 42 mAh g^{-1}. The Na-ion storage capability of holey graphene can be further boosted by heteroatom doping due to expanded interlayer distance and enhanced conductivity. In the work of Zhao et al.,[52] the holey graphene showed a high capacity of 446 mAh g^{-1} at 0.1 A/g by codoping oxygen and nitrogen atoms.

Lin et al. [53] investigated the promising aspect of applying holey graphene as cathode materials in Li-S hybrid batteries. This type of batteries has recently received much interest owing to their high theoretical capacity and ultrahigh energy density; however, its poor rate capability significantly restricts the practical applications. This paper reported a composite cathode consisted of holey graphene and sulfur, exhibiting a high specific capacity of 1215 mAh g^{-1} at 1 mA cm^{-2} and an excellent rate capability with 402 mAh g^{-1} at 5 mA cm^{-2}. Similar to

Na-ion batteries, doping holey graphene with heteroatoms could further contribute to performance upgrade. Li et al. [54] fabricated a cathode with nitrogen-doped holey graphene and sulfur that exhibited a reversible capacity of 1062 mAh g^{-1} at 0.2 C, outperforming its counterpart composed of non-holey graphene and sulfur (800 mAh g^{-1}).

Mechanisms of performance enhancements brought by the nanoholes on holey graphene. By looking at all the collected studies on holey graphene for electrochemical energy storage, it is not too hard to find out the root causes of the superior electrochemical properties of holey graphene against pristine graphene, and they are i) the faster ion diffusion inside the electrode material and ii) the faster charge transfer at the electrolyte/electrode material interface. In fact, these two aspects can be further related to the effects of the nanoholes themselves and the edge-site atoms around the nanoholes, respectively. The schematics of the mechanisms of performance enhancements brought by the nanoholes on holey graphene is shown in Fig. 4**a**.

In terms of the ion diffusion, the nanoholes bring two major effects on the electrochemical performance of holey graphene: more ion diffusion channels and a larger effective surface area. From a perspective of the process, the nanoholes create more through-the-plane channels for ion diffusion inside the electrode, thus promoting the kinetics of the electrochemical process (Fig. 4**b**). From a perspective of the result, the ion diffusion channels created by the nanoholes result in an increase of the effective surface area of the electrode material by making the nanosheets that stay deep in the electrode and far away from the electrode/electrolyte interface accessible to the electrolyte so they can participate in the charge transfer process. Note that, the impacts of nanoholes on the ion diffusion of electrodes, significantly rely on the size and size distribution of nanoholes as well as the size of ions and their interactions with edge atoms.

As an example, M. Kotal et al.[39] report that the Brunauer–Emmett–Teller (BET) surface area of the N,S-doped holey graphene aerogel is 395 m^2 g^{-1}, and that of the N,S-codoped graphene aerogel prepared via the same conditions is only 183 m^2 g^{-1}. Another study by Z. Pan et al.[34] shows that a B,N,P-doped holey graphene aerogel has a BET surface area of 980 m^2 g^{-1}, 2 times of that of the non-holey counterpart.

Though nanoholes may negatively impact the electrical conductivity of graphene, a faster ion diffusion rate can be more beneficial to performance than a higher conductivity in electrochemical applications. This can be confirmed in the paper by D. Wu et al.[50] They find that the capacity of the nanocomposite of hollow Co_3O_4 and holey graphene is much higher than that of the one using nitrogen-doped graphene, which possesses even higher conductivity than pristine graphene. Y. Xiang et al.[92] indicate that the ion diffusion coefficient of lithium ions in the holey graphene based nanocomposite (10^{-10} cm^2 s^{-1}) is two magnitudes higher than that in the pristine graphene based one (10^{-12} cm^2 s^{-1}), which is actually one magnitudes lower than the blank active material (10^{-11} cm^2 s^{-1}). This result also suggests that the graphene without in-plane nanoholes can strongly hinder the ion transport in the electrode of batteries.

With a faster ion diffusion rate inside the electrode brought by the nanoholes, it is possible to realize the thicker or denser energy storage devices that combine the advantages of batteries and supercapacitors with both high energy and power densities. While the closely packed graphene sheets retard the ion diffusion kinetics and limit the capacity or capacitance of the electrode, the ones with nanoholes can be gradually activated during charging and discharging. S. Stolyarova et al.[91] found that after 1000 cycles, the MoS_2 @holey graphene electrode achieved an increase of 133% of its first-cycle capacity from 912 to about 1200 mAh g^{-1}. H. Sun et al.[56] manufactured a 3D holey graphene/Nb_2O_5 composite with highly efficient electrode kinetics, and it was used to fabricate a high mass loading electrode, which exhibited high energy densities without compromising the rate performance. At a high mass loading of 11 mg cm^{-2}, it showed a specific capacity of 139 mAh g^{-1} at a high rate of 10 C, which was only 7% less than that of the low-mass loading electrode (1 mg cm^{-2}). The composite exhibited a specific capacity retention of 93% with the mass loading changing from 1 to 11 mg cm^{-2}, while the graphene/Nb_2O_5 composite showed only 61%. Z. Pan et al.[34] fabricated a high-mass-loading supercapacitor (10 mg cm^{-2}) by B,N,P-doped holey graphene aerogels delivering ultrahigh gravimetric and volumetric energy densities of 38.5 Wh kg^{-1} and 57.4 Wh L^{-1} with ultrahigh power densities of 83 kW kg^{-1} and 55 kW L^{-1} and a long cycle life (81.3% retention after 50,000 cycles). A Ti_3C_2 MXene@holey graphene symmetric supercapacitor prepared by Z. Fan et al. [42] retains a volumetric capacitance of 998 F cm^{-3} at a ultrahigh mass loading of 12.6 mg cm^{-2}, while the pure graphene version

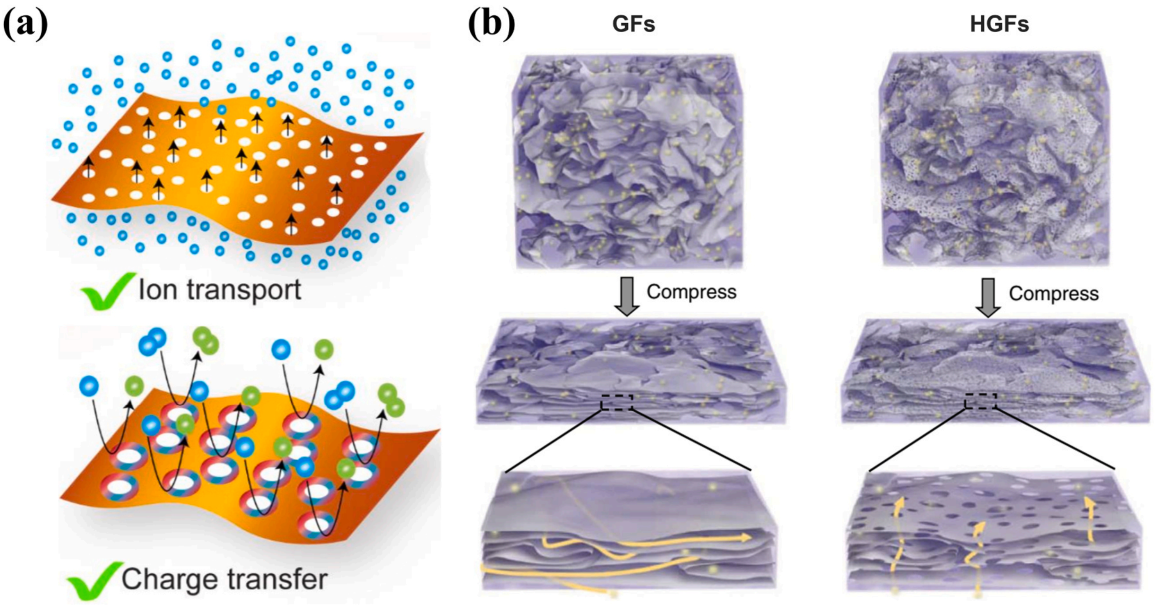

Fig. 4. Mechanisms of performance enhancements brought by the nanoholes on holey graphene: (a) ion transport and charge transport enhanced by nanoholes and edge-site atoms around nanoholes (Reproduced with permission.[61] Copyright 2020, Elsevier.); (b) Ion paths inside the electrode of a supercapacitor based on pristine graphene and holey graphene (Reproduced with permission.[33] Copyright 2014, Nature Publishing Group.).

of this material has only about 400–500 F cm^{-3}.

Creating nanoholes also allows gases to escape from the graphene powder mixture during electrodes compressing, thus enabling binder-free graphene structures with densities notably higher than what can be obtained by pure graphene. D. Kirsch et al.[101] reports the free-standing, binderless holey graphene electrode by compression. X. Han et al.[102] uses holey graphene to achieve the manufacturing of graphene monolithic architectures with a high density of 1.4 g cm^{-3} while maintaining the outstanding specific mechanical strength (18 MPa cm^3 g^{-1}) and electric (13,000 S m^{-1}) and thermal (20 W $m^{-1}K^{-1}$) conductivities.

It is a common concern that the volumetric specific capacity of the battery might be compromised when adding low-density porous materials like graphene, and the same concern falls upon holey graphene. Nevertheless, studies have shown that the gravimetric and volumetric specific capacities can be improved at the same time. Y. Xiang et al.[92] report a lithium titanate ($Li_4Ti_5O_{12}$) and holey graphene nanocomposite. At a low current density of 0.035 A g^{-1}, it has a specific capacity of 200 mA h g^{-1} based on the weight of $Li_4Ti_5O_{12}$, which is higher than that of the one with pristine graphene (190 mA h g^{-1}). At higher current densities up to 7 A g^{-1}, the former still retains 78%, and the latter has almost lost all the capacity. The similar trend is found in the variation of the volumetric specific capacity, and the former retained 98 mA h cm^{-3} at 17.5 A g^{-1}. M. Kotal et al.[39] report that the solid-state supercapacitor composed of holey graphene aerogel electrodes shows a volumetric capacitance of 203 mF cm^{-3} at 1 mA cm^{-2} and an volumetric energy density of 0.409 Wh L^{-1} with 95.4% retention after 1100 cycles.

These holes not only reduce the ion diffusion resistance but also the electron-ion charge transfer resistance in graphene flakes, which contributes to a faster kinetics during the charge and discharge process at the electrode/electrolyte interface. Y. Xiang et al.[92] shows that the charge transfer resistance of the nanocomposite of a lithium titanate and holey graphene is only a quarter of that of the one with pristine graphene. The reduced charge transfer resistance is attributed to the large amount of edge atoms created during hole-making process, while these edge sites have ultra-high electrochemical activities.

Further doping of these edge sites is demonstrated as another strategy to improve the electrochemical performance of the holey graphene. P. Xu et al.[65] compared the specific surface area, conductivity, and electrochemical capacitance of holey graphene aerogel and holey N-doped graphene aerogel and found that N doping effectively improved all the three properties of holey graphene aerogel. X. Ye et al.[40] added *p*-phenylenediamine (PPDA) molecules in between holey graphene sheets, which avoided restacking and exhibited both high gravimetric and volumetric capacitances of 300 F g^{-1} and 516 F cm^{-3} at 0.5 A g^{-1}, while pristine graphene had only 235 F g^{-1} and 357.2 F cm^{-3}. The FSSC assembled using this material showed energy and power densities of 2.18–2.72 Wh L^{-1} and 146.5–3313.6 W L^{-1} with a total volume of $3.8–4.2 \times 10^{-3}$ cm^{-3}.

The coupling effect of holey graphene and active materials is an intriguing phenomenon. Research shows that the nanocomposite composed of both metal oxides and holey graphene can bring performance even higher than the sum of each material.[92].

Electrocatalytic applications

With the in-plane nanoholes, graphene gains much higher electrochemical activity and thus exhibits great potential to be used in the electrocatalytic applications where pristine graphene is only used as a conductive additive. These applications include metal–air batteries, metal–CO_2 batteries, water splitting, thermocells, heavy metal ion detection, electrochemical sensors, etc., as shown in Fig. 5.

Metal–air batteries. Metal–air batteries, such as the Li–air and Zn–air batteries, are attractive energy storage devices due to the ultrahigh theoretical capacity (ca. 3500 Wh kg^{-1} for Zn–air). The operation of these batteries relies on the ORR and OER processes occurring on the air cathode, which is currently made of Pt/C. To reduce the cost of the electrode and improve the ORR and OER performance, holey graphene-based materials are introduced in these applications. D. Yu et al.[103] reported that the N-doped holey graphene aerogel was comparable to the Pt/C electrode in both the oxidation of hydrazine and oxygen reduction reaction (ORR). Y. Bian et al.[104] prepared N-doped holey graphene with a specific surface area of 1170.05 m^2 g^{-1} and 5.1 at% N doping. The ORR performance of this material (an onset potential of 0.91 V and a half-wave potential of 0.833 V) was higher than N-doped

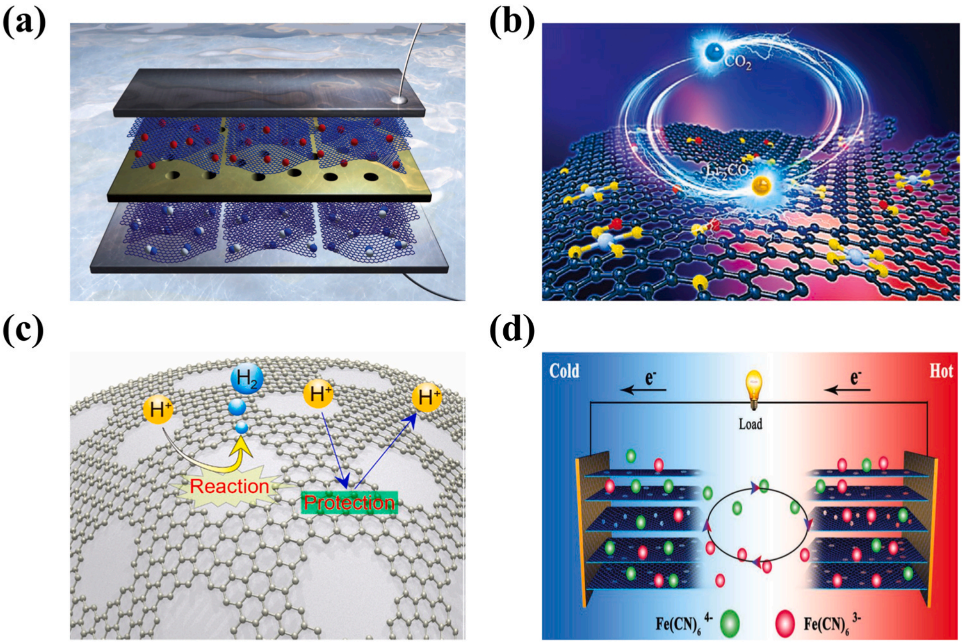

Fig. 5. Catalytic applications of holey graphene: (a) OER and ORR catalyst for metal–air batteries (Reproduced with permission[123]. Copyright 2012, Nature.); (b) catalyst for metal–CO_2 batteries (Reproduced with permission.[110] Copyright 2020, Wiley.); (c) HER catalyst for electrochemical water splitting (Reproduced with permission.[112] Copyright 2018, ACS.); (d) thermocells (Reproduced with permission.[115] Copyright 2019, Wiley.).

rGO and close to the Pt/C electrode. P. Du et al.[105] found that the ORR and OER performance of N,Mo-doped holey graphene was better than not only N,Mo-doped graphene but also Pt/C. They discovered that the higher number of nanoholes promoted the onset and half-wave potentials in the ORR process, and in OER process the nanoholes enhanced both the electrochemical surface area and the heteroatom doping. The Zn-air battery with this material as the air cathode exhibited higher maximum power density and discharge voltage and better cycling stability than the Pt/C–IrO_2-based batteries. W. Kong et al.[106] reported a Co,N-codoped holey graphene aerogel which exhibited an oxygen reduction reaction (ORR) activity comparable to the commercial Pt/C electrode due to efficient mass transport and abundant active sites around holey and doped areas. $Co_{5.47}N$ @ holey N-graphene[107] exhibited high catalytic activities for both ORR and OER due to the holey structure and strong connection between nanoparticles and holey graphene. The composite electrode brought a power density of 120.7 mW cm^{-2} and a specific capacity of 610 mAh g^{-1} (calculated by the weight of Zn) when assembled in Zn-air batteries. Ni–NiO@holey graphene had higher specific surface area (166.1 m^2 g^{-1}) and lower charge transfer resistance (101 Ω) compared to its counterpart of pristine graphene (72.3 m^2 g^{-1} and 143 Ω), so the former showed better OER performance with an overpotential of only 0.308 V, much lower than that of the latter (0.403 V).[108].

Metal– CO_2 batteries. As a solution to the energy storage for Mars explorations (where the atmosphere contains ca. 96% CO_2), the Li–CO_2 battery draws huge attention from the researchers interested in this field. Similar to the Li–air battery, this battery relies on the reduction and revolution of CO_2 on the cathode, and the electrochemical activity of the cathode material plays a vital role in these processes. Holey graphene exhibits prominent specific capacity, rate performance, and cycling stability in this battery due to the high electrochemical activity offered by the abundant active edge-sites atoms around the nanoholes. L. Qie et al. [109] prepared B,N-doped holey graphene with 4.1 at% N and 2.6 at% B and used it as the cathode in a Li-CO_2 battery obtaining significant improvement in irreversible polarization, rate performance, and cycle life. By incorporating single Fe atoms in N,S-doped holey graphene, the cathode made of this material in a Li-CO_2 battery exhibited an initial discharge capacity of 23,174 mAh g^{-1}, significantly higher than that of its counterpart of pristine graphene (15,280 mAh g^{-1}), due to the simultaneous improvement in gas/ion diffusion and catalytic activity brought by the nanoholes. [110].

Water splitting. Water splitting may be a significant energy generation technology in the near future as it produces a green energy resource, hydrogen. A work from Y. Luo et al. showed that the morphology and surface chemistry engineering play key roles in developing efficient electrocatalysts for hydrogen evolution (HER), especially for large current density reactions. [111] Holey graphene can typically realize fast ion and mass transport in electrochemical reactions due to the holes on basal plane working as transport channels, and the large amount of edge-site atoms surrounding the holes can be doped or incorporated with other materials leading to high electron ion charge transfer rate. These superior characteristics make holey graphene a potential candidate material for realizing high current density reactions, which currently severely restricts the practical implementation of HER and water splitting in widespread applications. Y. Ito et al. [112] reported that holey graphene incorporated NiMo showed the HER activity comparable to the commercial Pt/C electrode, demonstrating the potential application of holey graphene in electrochemical water splitting. A. Kumatani et al. [113] compared the HER activities of various holey doped graphene, including holey N,P-doped graphene, holey N-doped graphene, holey P-doped graphene, and non-holey N,P-doped graphene, and found that N,P co-doping led to the HER activity of holey graphene close to that of Pt electrode. Although the specific surface area of the holey N,P-doped graphene (622.5 m^2 g^{-1}) was lower than that of the non-holey one (821.5 m^2 g^{-1}), the charge transfer resistance of the former (21.5 Ω) was just half of that of the latter (48.1 Ω), indicating that the higher electrochemical activity led to the better HER performance. K. Savaram et al. [114] reported that the abundant zigzag edges around the nanoholes on holey graphene largely increased the catalytic activity, thus making it a potential metal-free catalyst in hydrogenation.

Thermocells. Thermocells convert temperature-dependent electrochemical redox potential to electric power. As the electrode material of the thermocell, holey graphene improves the cell performance by facilitating the ion diffusion kinetics within the electrode. As reported by G. Li et al.,[115] the power density of a single holey graphene-based thermocell reached 3.6 W m^{-2}, about three times that of activated carbon cloth electrodes, or 6.8 W kg^{-1}, increased by about 76% compared to that of rGO electrodes. The energy conversion efficiency of a single cell relative to the Carnot engine was 0.7%, much higher than that of other electrochemical thermocells (0.4%).

Heavy metal ion detection. F. Mo et al.[116] reported a AuNC@holey graphene for heavy metal ion detection showing favorable selectivity, accuracy, and recovery. Table 3.

Electrochemical desalination

Electrochemical desalination is an innovative and energy-efficient process that utilizes electrochemistry to remove salts and other minerals from water, making it suitable for human consumption, irrigation, and industrial use. By applying a voltage across electrodes inserted into saltwater, ions are drawn towards the oppositely charged electrodes, separating the salts from the water. W. Kong et al.[117] reported a holey graphene aerogel with a MB specific surface area of 1216.7 m^2 g^{-1}, and when it was used as the capacitive deionization electrode for water desalination systems, it exhibits a high desalination capacity of 26.8 mg g^{-1} in a 5 mg ml^{-1} NaCl solution due to the high capacitive absorption, which is confirmed by the high specific capacitance of 148 F g^{-1} in a 0.5 M NaCl solution.

M. Mi et al.[124] prepared a composite framework of holey graphene nanosheets and N-doped mesoporous carbon spheres via hydrothermal synthesis, and it had a specific surface area of 337.7 m^2 g^{-1} and a specific capacitance of 226.5 F g^{-1} in a 0.5 M NaCl solution. Its electro-sorption capacity was 6.8, 17.8, and 32 mg g^{-1} in 0.05, 0.5, and 2.5 mg ml^{-1} NaCl solutions, respectively, which did not obviously decline after 35 desalination cycles.

Y. Yang et al.[125] prepared a composite membrane of holey graphene nanosheets and carbon nanotubes with an average nanohole size and density of 0.63 nm and about 1.0×10^{12} cm^{-2}. The composite membrane showed a water permeance of 7.5–37.2 L m^{-2} $hour^{-1}$ bar^{-1} in a device based on cross-flow forward osmosis measurements, while the non-holey version had a negligible permeance. In a reverse osmosis cross-flow filtration apparatus, the composite membrane exhibited a hydraulic permeance of 110 L m^{-2} $hour^{-1}$ bar^{-1} with high salt rejection percentages in a range of 85.2–93.4% for NaCl, KCl, $MgCl_2$, and Na_2SO_4 and high rejection percentages of larger than 96% for methylene blue, rhodamine B, and fluorescein isothiocyanate. Moreover, the composite membrane withstood the 24 h osmotic operation while keeping a high salt rejection percentage.

Biochemical applications

Beyond the large surface area, excellent chemical and mechanical stability, and good biocompatibility of pristine graphene, the in-plane nanoholes enable unique structural and electronic properties for molecule traverse and adsorption. These unique properties offer great opportunities of applying holey graphene in biochemical applications including DNA sequencing, drug delivery and biomolecular sensor (Fig. 6).

Table 3
Properties of holey graphene for catalytic applications.

Materials	Surface area [m^2 g^{-1}]	Electrical conductivity [S m^{-1}]	Charge transfer resistance [Ω]	Ion diffusion coefficient [cm^2 s^{-1}]	Cycle life
Holey graphene [114]	744	17,500	\	\	\
Holey Co,N-graphene [106]	427 (220)	\	55	\	\
Holey N-graphene/NiMo [112]	\	\	5.1 (219)	\	\
Holey N-graphene aerogel [103]	784 (277)		40 (60)	\	96% @ 500
Holey B,N-graphene [109]	516.4		\	\	~100% @ 200
Holey graphene aerogel [117]	1216.7 (785.5)	\	1.02 (1.17)	4.29 (4.28) × 10^{-5}	
Holey graphene aerogel[64]	398	0.32	1.6	\	95.6%@ 2000
Holey N-graphene [118]	\	\	\	\	\
Holey N-graphene quantum dots [119]	353	\	1.3	\	
Holey graphene [120]	422 (657)	\	79–85		~100% @ 3000
Holey N,P-graphene [113]	622.5 (821.5)	\	21.5 (48.1)	\	85% @ 1000
Holey N,S-graphene [121]	362 (166)	\	\	\	~100% @ 2 d
Fe@holey N,S-graphene [110]	598		\	\	~100% @ 100
Ni–NiO@holey graphene [108]	166.1 (72.3)	\	101 (143)		\
Holey N,Mo-graphene [105]	430 (310)		\	\	~100% @ 5000 ORR ~100% @ 1000 OER
Holey N-graphene [104]	1170.05 (~600)	\	\	\	90.7% @ 2.78 h
MnO_2 @holey graphene [122]	247	\	\	\	\

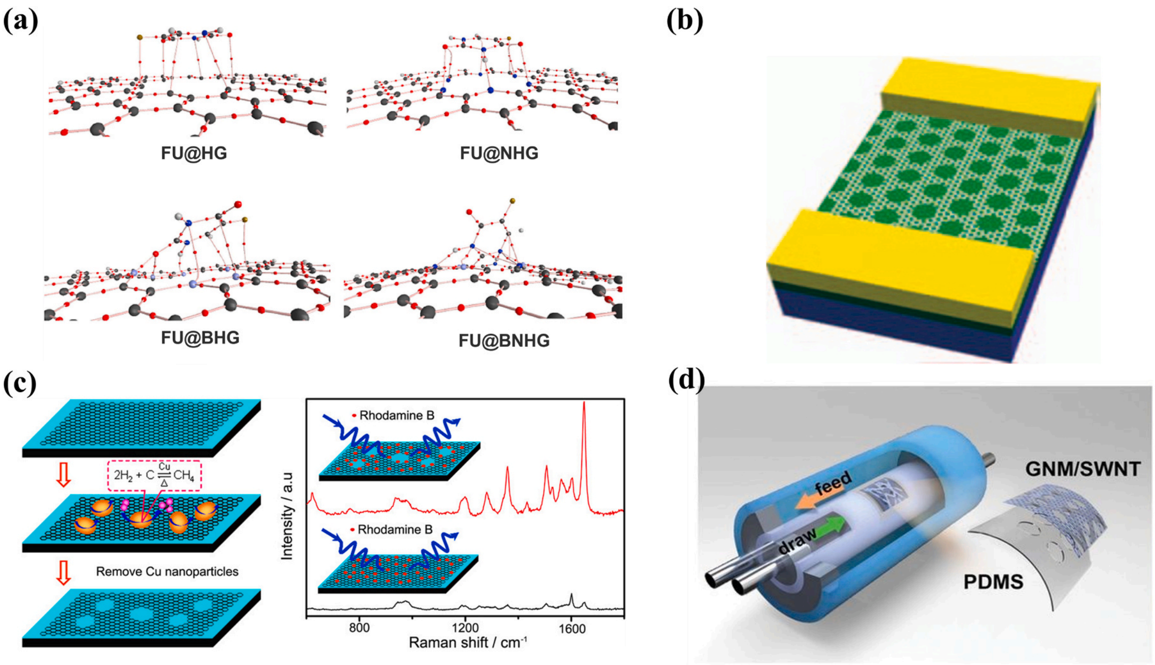

Fig. 6. Holey graphene for biochemical applications: (a) drug carrier (Reproduced with permission.[126] Copyright 2020, Elsevier); (b) biosensor (Reproduced with permission.[127] Copyright 2012, ACS). Holey graphene for electronics: (c) field-effect transistor (Reproduced with permission. [28]Copyright 2010, Nature). (d) Holey graphene for desalination (Reproduced with permission.[125] Copyright 2019, Science.).

DNA sequencing. Nanopore technology has received considerable attentions in genomic screening, particularly DNA sequencing which has significant impacts on diagnosis and treatment of diseases. In this application, the translocation of DNA molecules through nanoholes induces changes in ionic current that contributes to identifying four different types of nucleotide. Holey graphene provides new opportunities in this field for sequencing with faster identification and higher resolution, due to its unique properties such as excellent electrical conductivity and mechanical strength. In 2010, Schneider et al.[128] experimentally proved that monolayer graphene with nanohole size ranging from 2 to 40 nm could be used for single-molecule DNA translocation. It was found that the monolayer graphene has similar sequencing performance as a 20-nm-thick SiN membrane, in terms of the magnitude of the conductance drop arising from the DNA molecule translocating through the nanohole and the translocation time. More importantly, holey graphene with atomic thickness breaks the spatial-resolution limit of previous DNA sequencing analytics to sub-nm accuracy.

Drug delivery. Graphene has been extensively explored as one of the most promising biomaterials for the drug delivery application due to its high-loading efficiency. The emerge of holey graphene has provided new opportunities in future health-care industry since the edge-site atoms around nanoholes often possess a high chemical reactivity and thus can be easily doped with heteroatoms to enable modifications of adsorption energy, molecular electrostatic potentials, and electronic properties. In the work of J. Jiang et al.,[126] the interactions of holey graphene and B/N-doped holey graphene with 5-fluorouracil (FU) anticancer drug were investigated via DFT simulations. It was demonstrated that compared to pristine, N-doped, and B,N-doped holey graphene, B-doped holey graphene had a greater potential as an effective drug carried due to its high electrostatic adsorption energy to the FU drug. This was explained by the shorter interaction distance between O atoms of FU and B atoms of doped holey graphene. They further simulated that the interaction between the FU drug and B-doped holey graphene could be weakened when the pH of cell environment was reduced, enabling drug release onto the target site as tumor cells often has a lower pH value than normal cells.

Biomolecular sensor. Detection of hazardous biochemicals is of great importance to the ecological environment and human health. Due to the enhanced electron transfer kinetics and electrocatalytic activity, holey graphene has been applied to fabricate rapid and sensitive sensor for environmental monitoring and food/water security. J. Liu et al.[127] successfully used holey graphene to detect rhodamine B (RhB) molecules via Raman characterization. It was reported that the edges of nanoholes change its electronic structure and induces spontaneous p-type doping effect, leading to local charge transfer and adsorption of RhB molecules. Consequently, compared to pristine graphene, holey graphene enables enhanced Raman intensity for RhB molecules for sensitive detection. Similar experiment has been conducted by Y. Yang et al.[129] to detect carbendazim pesticide using holey graphene-based sensor. The promising detection limit and sensitivity were attributed to the excellent current response to carbendazim due to the nanohole-induced accelerated electron transfer and enhanced electrochemical performance.

Electronic applications

Holey graphene obtains the tunable band gap that pristine graphene does not possess, making it an attractive 2D semiconducting nanomaterial for the electronic applications, including field-effect transistors (FETs) and optoelectronics devices.

J. Bai et al.[28] prepared holey graphene with precisely patterned distribution of nanoholes aiming to replace graphene nanoribbons in FET, which have low driving currents and require high-cost processing. They found that the holey graphene-based FET could support significantly higher currents than graphene nanoribbon devices, and the electronic properties, such as the on–off ratio, could be effectively tuned by adjusting the neck width of holey graphene. X. Liang et al.[130] found that the band gap of holey graphene and the on–off ratio of the holey graphene FET increases with the inverse of the neck width of holey graphene. Z. Zeng et al.[131] proposed a different routes to obtain the patterned holey graphene. D. Yang et al.[132] fabricated a holey graphene FET with n-type behaviors and a high on–off ratio (ca. 2.5). O. Akhavan[133] prepared the patterned holey graphene with p-type behaviors.

D. Singh et al.[134] calculated the electronic, optical, and thermoelectric properties of the holey graphene structure that had two mirrored holes. The direct band gap and optical gap were 0.95 eV and 1.28 eV, and the thermopower was 1662.59 $\mu V\ K^{-1}$, suggesting that holey graphene was a promising material in optoelectronic and thermoelectric applications.

Nitrogenated carbon nanosheet

The holey nitrogenated carbon nanosheet, i.e., C_2N (Fig. 7**a**), is the graphene-like structure that has periodic nanoholes and nitrogen atoms substituting some of the specific carbon sites. It was created in searching of semiconductive structures for N-doped graphene nanosheets. Compared with non-holey N-doped graphene, holey C_2N has a periodic lattice and well-defined electronic structure, which meet the requirement of the fine nano-manufacturing processes in semiconductor industries. This unique porous structure of C_2N is expected to widen the bandgap to an ideal level for various application. Its theoretical and experimental bandgaps were reported as ca. 1.70 and 1.96 eV, respectively, and the field-effect transistor made of it showed a high on–off ratio of 10^7[135]. This multi-functional structure also exhibited favorable properties as catalysts. By encapsulating Fe nanoparticles[136] in C_2N or incorporated with Co_3O_4 nanoparticles[137], the ORR activity was comparable with that of the Pt/C electrode, while the cycling life was obviously superior than that of the latter.

Hexagonal boron nitride

Hexagonal boron nitride (*h*-BN) is a heteroatomic 2D nanomaterial and exhibits tunable electronic properties due to the diversity of the edge structure of this material. Like that of graphene, the edge of *h*-BN (Fig. 7**b**) can be like zigzag or armchair structures, while the zigzag edge of *h*-BN can further evolve into two forms, boron- and nitrogen-terminated edges, giving *h*-BN a vital role in the semiconductive 2D materials. Creating nanoholes on *h*-BN can open up a new dimension in tuning its electronic properties. Similar to holey graphene, the presence of holes with abundant edge-site atoms could finely tune through-plane molecular transport. Enlightened by the success of holey graphene, Y. Liao et al.[138] manufactured holey *h*-BN via a catalytic etching process and proposed potential applications in catalysis and molecular separation. Significantly changes in UV absorption spectra were observed, suggesting the distinct electronic structure of holey *h*-BN relative to its pristine version. However, further structural characterizations and property measurements should be taken to fully demonstrate the superiority of the holey version of this material.

Phosphorene

Similar to the development of holey *h*-BN, H. Liu et al.[139] were

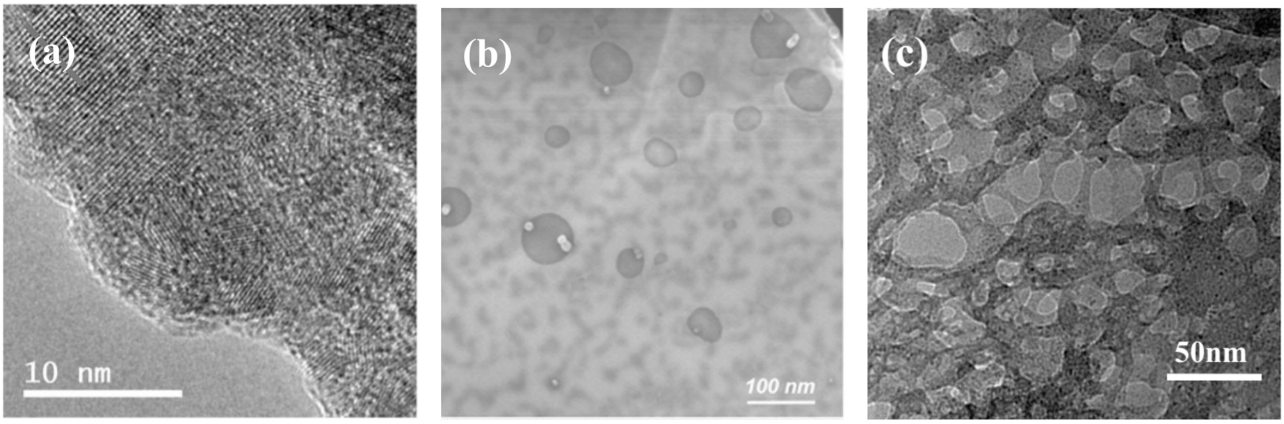

Fig. 7. Holey graphene-like materials: (a) Holey C_2N;(Reproduced with permission. [135] Copyright 2015, Nature) (b) holey *h*-BN; (Reproduced with permission. [138] Copyright 2015, Nature) (c) holey phosphorene. (Reproduced with permission. [139] Copyright 2019, Elsevier).

inspired by holey graphene and manufactured holey phosphorene via a electrochemical method, which would possess a larger specific surface area, high density of reactive sites and higher ion transport rate over pristine phosphorene. The obtained holey phosphorene (Fig. 7**c**) showed a large areal percentage of nanoholes, causing the blue-shifts of its Raman peaks and the change of its UV–vis absorption spectrum. The authors proposed the potential applications in photocatalysis and membrane separation, whereas further demonstrations are required.

Transition metal oxides and nitrides

2D TMOs and TMNs, mainly the oxides or nitrides of Fe, Co, Ni, Mn, Zn, Nb, are competent candidates for the electrode materials of electrochemical energy storage devices, including metal-ion batteries and supercapacitors, due to the coupling of the high intrinsic chemical activity of these crystals and the high specific surface area of the 2D structure (Fig. 8). Since TMOs and TMNs are not layered crystals like graphite, it is not possible to obtain the nanostructures composed of 2D lattice via either exfoliation of bulk materials or bottom-up deposition. So is manufacturing holey 2D TMOs and TMNs, while researchers have found a way to assemble the nanoparticles of TMOs or TMNs into 2D nanosheets with nanoholes left in between. The nanoholes increase the ion diffusion channels and the specific surface area accessible to the electrolyte promoting the kinetics of the energy storage process, and they can also offer the buffering spaces in between the nanoparticles to prevent the adverse effects of the volume expansion and contraction of these nanoparticles during charging and discharging.

Metal-ion batteries

G. Yu and his colleagues lead the research in this field. They developed a variety of holey 2D TMOs, including Co_3O_4, Mn_2O_3, Fe_2O_3, $ZnMnO_4$, $ZnCo_2O_4$, $NiCo_2O_4$, and $CoFe_2O_4$ for both lithium- and sodium-ion batteries.[140] The averaged specific capacity of the holey 2D $ZnMnO_4$ nanosheet anode in the lithium-ion battery was ca. 710 mAh g^{-1} at 0.2 A g^{-1} after 110 cycles of charging and discharging, and it retained a ca. 56% capacity at a high current density of 1.2 A g^{-1}, exhibiting significantly higher rate capability than the counterparts (32% for $ZnMnO_4$ + super P and 6% for $ZnMnO_4$). Similar trends were found for holey 2D $ZnCo_2O_4$ and $CoFe_2O_4$ compared to their counterparts. Moreover, the cycling life of these holey 2D TMOs were found all better than the non-holey ones. The specific capacity of the holey 2D $ZnMnO_4$ nanosheet anode retained ca. 360 mAh g^{-1} at a high current density of 1 A g^{-1} after 1000 cycles.

In sodium-ion batteries, since the volume expansion of the anode material during charging and discharging is severer than that in lithium-ion batteries (because of the larger radius of a sodium ion relative to a sodium ion), the advantages of the holey 2D TMOs become more obvious against their non-holey versions, making the former attractive in sodium-ion batteries. The same paper mentioned above reported that the holey 2D $NiCo_2O_4$ nanosheets as the anode in sodium-ion batteries exhibited a specific capacity of ca. 550 mAh g^{-1} at 0.2 A g^{-1} and kept at ca. 230 mAh g^{-1} at a high current density of 1.6 A g^{-1}, where the non-holey version showed only ca. 60 mAh g^{-1}.[140] After charging and discharging for 100 cycles at 1.6 A g^{-1}, the specific capacity of the holey 2D $NiCo_2O_4$ nanosheet anode retained ca. 160 mAh g^{-1}, while that of the non-holey version was only ca. 36 mAh g^{-1}.

In a follow-up study, this group reported the coupling effect of the diameter of nanoholes and single nanoparticles of holey 2D TMOs on lithium- and sodium-ion battery performance.[141] They found that a higher ratio of diameters of nanoholes to nanoparticles led to better specific capacity and cycling life of these materials as anodes in both lithium- and sodium-ion batteries. It means that larger nanoholes and smaller nanoparticles (in certain ranges, 5–20 and 8–45 nm as reported by this study) are favorable to the performance because larger nanoholes can facilitate the ion transport and accommodate the volume fluctuation, and relatively smaller nanoparticles increase the specific surface area accessible to the electrolyte.

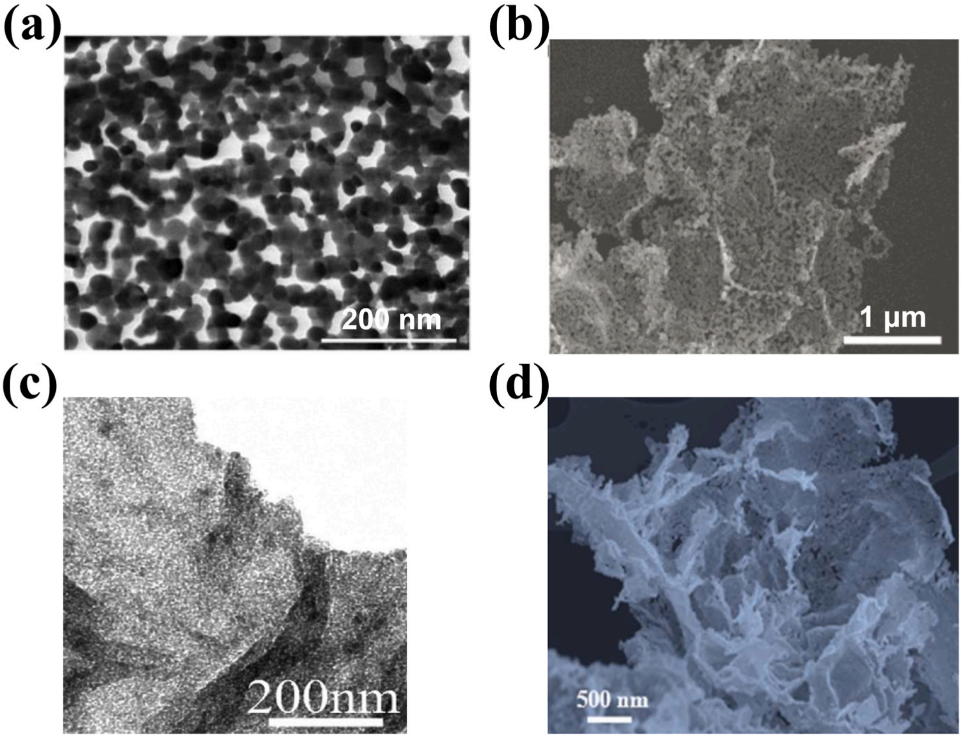

Fig. 8. Holey transition metal oxides and nitrides: (a,b) Holey 2D transition metal oxides; (Reproduced with permission.[140,142], Copyright 2017, Nature) (c) holey 2D $ZnFe_2O_4$ attached on rGO; (Reproduced with permission.[143] Copyright 2018, Elsevier) (d) holey 2D Co_3FeN. (Reproduced with permission.[145] Copyright 2019, RSC).

Mixed metal-ion batteries

H. Huang et al.[142] investigated the prospect of holey 2D Nb_2O_5 nanosheets as cathode materials in magnesium/lithium-ion hybrid batteries. This type of batteries is promising in combining the advantages of both lithium- and magnesium-ion batteries, which feature the development maturity and dendrite-free charging behavior, respectively, however, it is relatively picky with its selection of the cathode material. This paper reported that the holey 2D *t*-Nb_2O_5 nanosheets exhibited an initial discharge specific capacity of 199.6 mAh g^{-1} and retained 70% after 100 cycles at 0.2 A g^{-1}, higher than those of the *t*-Nb_2O_5 nanoparticles (186.1 mAh g^{-1} and 59% retention). After 1000 cycles at a high current density of 2 A g^{-1}, the specific capacity of the holey 2D *t*-Nb_2O_5 nanosheets remains 55.5 mAh g^{-1}. The superior performance of this material relative to its non-holey counterpart was accredited to its higher specific surface area, lower charge transfer resistance, and higher ion diffusion coefficient.

Performance of TMO/graphene nanocomposites

By incorporating holey 2D TMOs with graphene, the performance as anodes in batteries can be further promoted. W. Yao et al.[143] manufactured the nanocomposite of holey 2D $ZnFe_2O_4$ and rGO nanosheets. As the anode in lithium-ion batteries, it showed a specific capacity of 1022 mAh g^{-1} after 100 cycles at 0.5 A g^{-1} and retained its 47% capacity at a high current density of 8 A g^{-1} and 69% after 500 cycles at 2 A g^{-1}, which were all higher than those of the non-holey $ZnFe_2O_4$/rGO nanocomposite and pure $ZnFe_2O_4$ nanoparticles. The charge transfer resistance of holey 2D $ZnFe_2O_4$/rGO was 301 Ω, much smaller than those of its counterparts (356 and 626 Ω for $ZnFe_2O_4$/rGO and $ZnFe_2O_4$).

Supercapacitors

In supercapacitors, the high specific surface area and fast ion transport of holey 2D TMOs make them a good candidate material. B. Saravanakumara et al.[144] measured the energy storage performance of an asymmetric supercapacitor fabricated by holey 2D $MnCo_2O_4$ nanosheets paring with activated carbon and found that it delivered an energy density of 33.8 Wh kg^{-1} at a power density of 318.9 W kg^{-1} and retained ca. 85% of its full capacity after 10,000 cycles.

Zn–air batteries

H. Guo et al.[145] probed the application of holey 2D Co_3FeN nanosheets in Zn–air batteries, and the battery using this material as the air cathode catalyst exhibited a specific capacity of 890 mAh g^{-1}, higher than 836 mAh g^{-1} of Co_3Fe particles and 798 mAh g^{-1} of Co_3Fe layered double hydroxide. The holey 2D Co_3FeN nanosheets showed great electrocatalytic activities in both oxygen reduction and oxygen evolution reactions due to the active edge-site atoms and the abundant transport channels for the electrolytes, intermediates, and gases.

Lithium transition metal oxides

Owing to the success of the 2D materials as anodes of lithium-ion batteries, researchers start to evaluate the necessity of two-dimensionalizing lithium transition metal oxides (LTMOs), which are already broadly studied cathode materials. This type of materials includes lithium oxides of nickel, cobalt, manganese, and aluminum and their metallurgical mixtures with various compositions. By far, many efforts have been made to realize facile manufacturing of 2D LTMOs, while only a few are towards two-dimensionalization and creating nanoholes simultaneously. Y. Wu et al.[146] prepared and investigated a series of holey 2D LTMO nanosheets, including $LiCoO_2$, $LiNi_{0.8}Co_{0.15}Al_{0.05}O_2$, $LiNi_{0.8}Co_{0.1}Mn_{0.1}O_2$, $LiNi_{0.6}Co_{0.2}Mn_{0.2}O_2$, and $LiNi_{0.5}Co_{0.2}Mn_{0.3}O_2$, as the cathode material of lithium-ion batteries. Among them, the holey 2D $LiCoO_2$ cathode maintained a specific capacity of 138.6 mAh g^{-1} for up to 100 cycles at a current density of 0.5 C and a high cutoff voltage of 4.5 V; the holey 2D $LiNi_{0.8}Co_{0.15}Al_{0.05}O_2$, $LiNi_{0.8}Co_{0.1}Mn_{0.1}O_2$, $LiNi_{0.6}Co_{0.2}Mn_{0.2}O_2$, and $LiNi_{0.5}Co_{0.2}Mn_{0.3}O_2$ cathodes yielded 169.3, 162, 149.6, and 134.1 mAh g^{-1}, respectively, at a high current density of 5 C. It was reported that the nanoholes played a vital role in facilitating the ion transport kinetics and brought abundant edge-sites to improve the electrochemical activity.

Transition metal dichalcogenides

2D transition metal dichalcogenides (TMDCs, metal compounds of S, Se, and Te) are another group of versatile materials having been broadly investigated in electronics, energy storage and transfer, catalysis, biochemistry, etc. During the fast development of this area, researchers found that the edges of the 2D crystal of TMDCs are more catalytically active than the basal plane.[147] This enlightened further exploration of holey 2D TMDCs (Fig. 9).

D. Sarkar et al.[148] studied holey 2D MoS_2 nanosheets as active materials for solar water disinfection. By creating nanoholes on 2D MoS_2 nanosheets, the material obtained the edge-site atoms that had high electrocatalytic activity, and higher amount of hydroxide could be generated from the light-induced reaction on the surface of the material to eliminate the bacteria in water. This led to a 10^5 times improvement in the disinfection efficiency for the holey 2D MoS_2 nanosheets compared to its non-holey version. A prototype device removed 100% of 10^3 CFU ml^{-1} Escherichia coli in water after 5 passing-through.

Z. Fang et al.[149] explored holey 2D $Ni_xCo_{3-x}Se_4$ nanosheets as electrocatalytic materials for high efficient OER process. The material they obtained is like holey 2D TMOs, which are mostly nanoparticles interconnected with each other leaving spaces in between them, while the oxygen atoms are replaced by selenium. In this study, highly efficient OER processes were observed for 36 h with a low overpotential of 300 mV and a low Tafel slope between 50 and 60 mV/dec at a current density of 10 mA cm^{-2}. The favorable performance was due to the low OER overpotential offered by the mixed metal selenide lattice, plus the high electrocatalytic activity and electrolyte diffusion rate facilitated by the holey structure.

MXene

Holey 2D materials have been recently investigated for their potential application in nanohole-based biomolecular sensing, e.g., DNA and RNA translocation (Fig. 10**a**). During sensing, when a biomolecular is passing through a nanohole on the 2D material, electric signals are generated under a certain voltage applied across the nanohole and record this passage. Due to the atomic-thin thickness, the 2D materials can significantly enhance the detection resolution compared to the proteins as the current predominant sensor material. MXene as a conductive, hydrophilic, and mechanically robust 2D material is very competent in this field. This type of materials is generally composed of transition metal layers and carbon layers stacking one on another with functional groups doping on the surface. M. Mojtabavi et al.[150] prepared and investigated the holey MXene, Ti_2CT_x, in detecting DNA translocation and observed obvious current signals. The capture rate increased with voltage, and the nanohole on MXene was stable under a high voltage of 500 mV and the signal-to-noise ratio is higher than 10.

Layered double hydroxides

Layered double hydroxides (LDH) are layered hydroxides of active transition metals such as Fe, Ni, Co, Mn, etc. Due to the high catalytic activity, these materials are promising in fuel cells and water splitting applications. By creating nanoholes on the interconnected Ni,Co–LDH nanosheets (Fig. 10**b-d**), i.e., $NiCo(OH)_2$, N. L. W. Septiani et al.[151] demonstrated the higher specific surface area provided by this holey structure could enhance reaction kinetics and ion transport during OER process.

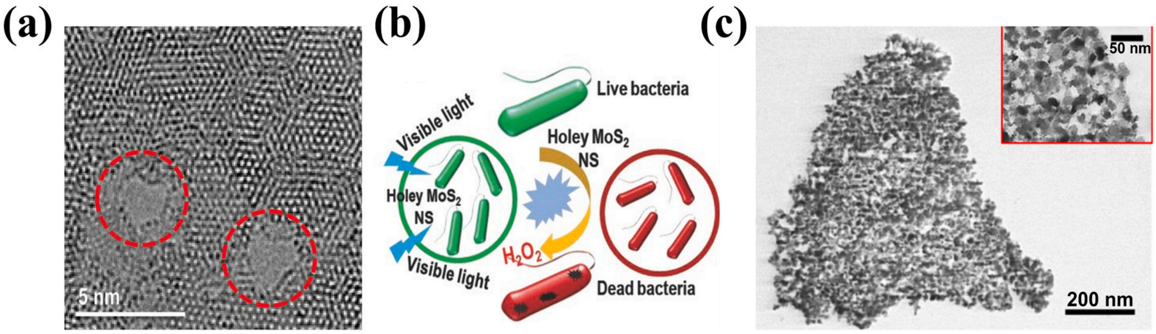

Fig. 9. Holey transition metal dichalcogenides: (a,b) Holey 2D Mo2S for solar water disinfection; (Reproduced with permission.[148] Copyright 2018, Wiley) (c) holey 2D Ni$_x$Co$_{3-x}$Se$_4$ for oxygen evolution reaction. (Reproduced with permission.[149] Copyright 2017, ACS.).

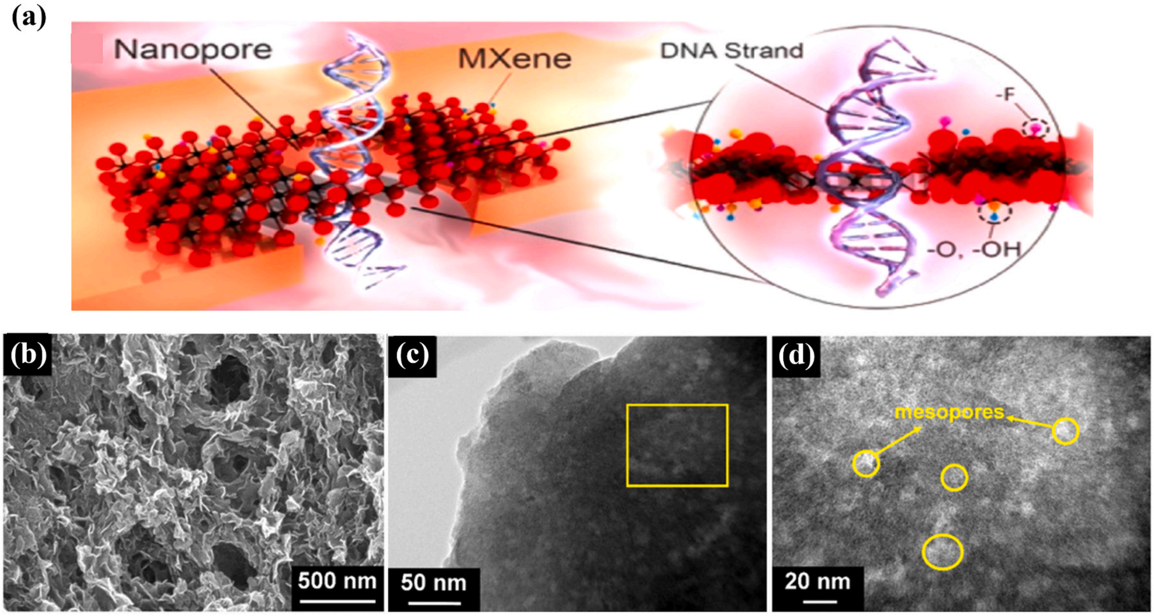

Fig. 10. (a) Holey MXene (Reproduced with permission.[150] Copyright 2019, ACS); (b,c,d) Holey layered double hydroxides (Reproduced with permission.[151] Copyright 2020, Wiley).

Manufacturing methods

The manufacturing methods for holey 2D materials are summarized and categorized in Fig. 11. According to the obtained distribution of nanoholes, i.e., the random or periodic distribution, sections 3.1 and 3.2 will discuss the current manufacturing methods for the random and periodic holey 2D materials, respectively. For each section, more subgroups are summarized based on their hole-formation mechanisms. All the mentioned holey 2D materials and the corresponding methods are listed in Table 4.

Manufacturing random holey structures on 2D crystals

Manufacturing 2D nanomaterials with random distribution of nanoholes is mostly by partially removing (i.e., etching) atoms from the 2D nanomaterial. The etching process can be induced by oxidation, hydrogenation, catalytic reactions, replacement reactions (i.e., interdiffusion), local high-energy impact, decomposition, etc., and the etchant can be very distinctive for each specific method, ranging from reactive chemicals to high-energy particles and from substances to electromagnetic waves. Another broadly adopted manufacturing method is by assembling atoms on a sacrificial holey template, such as holey graphene, via chemical vapor deposition or solution-based approaches.

Oxidative etching

Currently, the oxidative etching is the most adopted method for holey graphene manufacturing because the carbon atoms on graphene lattice are inert to acid or alkali but vulnerable under the oxidative environment. Many studies use O_2 or other oxidants, such as H_2O_2, HNO_3, Co_3O_4, Fe_2O_3, etc., as the etchant to directly react with the carbon atoms in the graphene materials, while the others use medium materials to catalyze the oxidative etching, and the reactions can be either photocatalyzed or electrochemically catalyzed.

For the manufacturing methods of other 2D materials, etching is often caused by nitridation, sulfidation, selenization, etc., which are also oxidative etching since they involve the reactions causing the increase of the valence state of the raw materials. Corresponding to these reactions, the oxidant can be nitrogen, sulfur, selenium, etc.

Etching by HNO_3. The earliest solution-based method to manufacture holey graphene was by using HNO_3 as the etchant (Fig. 12**a**), first seen in the study by X. Zhao et al. [29] They mixed 1 mg ml^{-1} GO (prepared by the Hummers method) aqueous dispersion and a 70% HNO_3 aqueous solution with GO-to-HNO_3 volume ratios of 1:5–1:12.5 and then ultrasonicated the mixture for 1 h to obtain the solution of holey GO, which

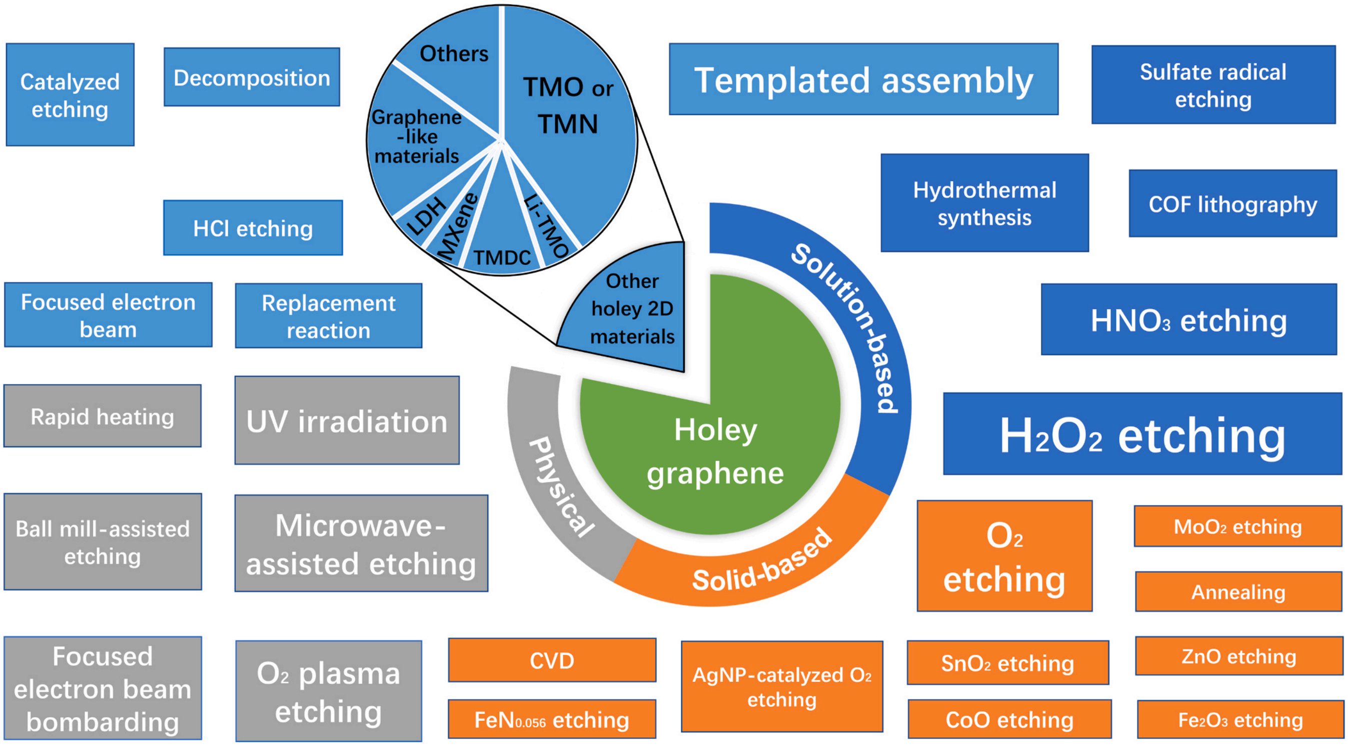

Fig. 11. Schematic showing the categories of various manufacturing methods for holey 2D materials.

was filtered, dried, and finally reduced by annealing under Ar or H_2/Ar atmosphere at 700 °C for 1 h. The randomly distributed nanoholes on holey rGO had the average diameters of 7, 20, 80 and 600 nm determined by the fraction of HNO_3 added in the mixture before reaction, and higher fractions led to larger average diameters. The authors perceived this idea referring to the process of cutting carbon nanotubes into fullerene pipes using concentrated acid, and then they proposed that nitric acid as a strong oxidant can oxidize the carbon atoms in the active areas including the existing edge sites of graphene sheets and the damaged sites created by ultrasonication. In two studies using the same method, the average diameters of nanoholes on holey rGO were 2–5 nm under the GO-to-HNO_3 volume ratio of 1:5[103] and 0–90 nm under a different set of parameters [152], respectively.

M. Petal et al.[159] used graphite powder as the starting material to fabricate holey GO in a one-step oxidative etching method. With microwave irradiation (300 W) to achieve simultaneous oxidative exfoliation and etching, the vigorous reactions between the graphite powder and the mixture of HNO_3 and $KMnO_4$ led to the formation of holey GO in just 40 s. They confirmed that non-holey GO was obtained if the duration of the microwave treatment was 30 s

Etching by H_2O_2. The method using H_2O_2 as the etchant are currently the most popular one for holey graphene manufacturing attributed by a series of works from UCLA (Fig. 12**b**). As reported in their first work on this subject, [33] 2 mg ml^{-1} GO (prepared by the Hummers method) aqueous dispersion and a 0.3% H_2O_2 aqueous solution were mixed with a GO-to-H_2O_2 volume ratio of 10:1, and the mixture was directly used in the hydrothermal treatment at 180 °C for 12 h to obtain the holey GO hydrogel, which was reduced in 1 M sodium ascorbate aqueous solution at 100 °C for 2 h. The obtained holey rGO framework showed a remarkably high BET specific surface area (ca. 830 m^2 g^{-1}), even after being compressed into holey graphene films (ca. 810 m^2 g^{-1}). This method was originated and adapted from a catalytic etching method proposed in an earlier work by J. G. Radich et al.,[160] which will be discussed in Section 3.1.2. The etching mechanism of using H_2O_2 is very similar to that of using HNO_3 since the oxidation of the carbon atoms in the active sites plays the vital role. It is believed that as the etchant, H_2O_2 are more attractive over HNO_3 given that the former is similarly effective, less corrosive, greener, and more easily to be fully removed from the prepared materials. In the subsequent studies by the same group in UCLA,[44] the method was slightly altered by separating the mixture reaction and hydrothermal treatment, increasing the H_2O_2 concentration, and lowering etching temperature and duration. Specifically, GO aqueous dispersion of 2 mg ml^{-1} and a 30% H_2O_2 aqueous solution were mixed with a GO-to-H_2O_2 volume ratio of 10:1 and heated under stirring at 100 °C for 4 h to obtain the holey GO solution. The obtained holey GO showed a BET specific surface area of ca. 430 m^2 g^{-1} and prominent pore size distribution in 2–3 nm determined by the Barrett–Joyner–Halenda method. Many studies adopted the H_2O_2 method to obtain holey GO for further development of new nanocomposites, and the size distribution was confirmed in the range of 1–10 nm by either the nitrogen adsorption measurement or TEM observation (Table 4).

While most studies carried out H_2O_2 etching by the solution-based method, which can be hours-long, Our group[61] reported a microwave-assisted H_2O_2 etching method for minute-scale manufacturing of holey graphene, making it cost-effective and promising for large-scale manufacturing (Fig. 12**c**). In this method, a 3 mg ml^{-1} GO aqueous solution pretreated by microwave irradiation for 90–360 s was mixed with a 30% H_2O_2 aqueous solution by a GO-to-H_2O_2 volume ratio of 5:2, and the mixture was irradiated under microwave for 45–180 s and centrifugated to obtain holey GO. The average size (368 nm^2 to 161 nm^2), size distribution, population (3 to 137), and area percentage (0.36% to 7.24%) were effectively controlled by tuning the lengths of the microwave pretreatment and microwave assisted H_2O_2 etching. [167] The major merit of this method was contributed by the rapid and direct energy delivery to the atoms on graphene sheets as we calculated the temperature of GO sheets were about 100 °C higher than the surrounding water under the microwave irradiation of this study. Compared to that under conventional heating, the etching reaction between H_2O_2 and GO was more efficient and effective under microwave heating, given that H_2O_2 molecules could easily decompose around 100 °C before reacting with GO.

Table 4
Holey 2D material manufacturing and the size and distribution of the obtained in-plane holes.

Material	Treatment	Hole-formation mechanism	Dry/ Wet	Size /nm	Pattern
Holey graphene	Solution-based etching	Oxidative etching: H_2O_2 etching [32–42,44,51,55,56,59,65,71,79,86,92,94,96,106,108,115,118,124]	W	2–3[44] 2–5[34] 2–4[106] 1–3.5[94] 2–10[51] 2[96]	Random
		Oxidative etching: HNO_3 etching [29,103,152]	W	7–600[29] 2–5[103] 0–90[152]	Random
		Sulfate radical etching [46]	W	1–10	Random
		Lithography: COF lithography [153]	W	4–50	Periodic
	Calcination	Oxidative etching: O_2 etching [52,57,58,101,102,104,109,110,154,155]	D	5–10[57] 10–20[102] 5–20[110]	Random
		Catalyzed etching: AgNP-catalyzed O_2 etching [47,81,156,157]	D	10^1–10^2 [156] 5–150[157]	Random
		Oxidative etching: Fe_2O_3 etching [121]	D	2–50	Random
		Oxidative etching: SnO_2 etching [62]	D	5–10	Random
		Oxidative etching: ZnO etching [158]	D	1.5–5	Random
		Oxidative etching: CoO etching [120]	D		Random
		Oxidative etching: $FeN_{0.056}$ etching [82]	D	20–30	Random
		Oxidative etching: MoO_2 etching [95]	D	2–50	Random
	Microwave-assisted etching	Oxidative etching: O_2 etching [114]	D	2–5	Random
		Oxidative etching: H_2O_2 etching [61]	W	\	Random
		Oxidative etching: $KMnO_4 + HNO_3$ etching [159]	W	\	Random
	UV irradiation	O_2 etching [132]	D	20	Random
		Catalyzed etching: AuNP-mediated, photocatalyzed OH• etching [160]	W	5–100	Random
		Catalyzed etching: Templated, ZnO-mediated, photocatalyzed etching [133]	D	200	Random
	Annealing	Catalyzed etching: Cu-catalyzed hydrogenation [127]	D	Nanoscale	Random
	Ball mill-assisted etching	KOH etching [66]	W	\	Random
	Hydrothermal synthesis	Oxidative etching: O_2 etching [63]	W	2–5	Random
	O_2 plasma etching	Lithography: Templated O_2 plasma etching [28,125,130,131]	D	17.7–31.9 [28] 67[131] 0.63[125]	Periodic
		Lithography: COF lithogrpahy [161]			
	Rapid heating	High-energy impact: Local pressure damage [31,60]	D	10–250[98] 50–100[23]	Random
	Focused electron beam bombarding	Focused electron beam [128]	D	2–40	Single
	CVD	Templated assembly [112,113]	D	10–15	Random
Holey 2D TMO or TMN					
Holey Co_3O_4, Fe_2O_3, Mn_2O_3, $ZnMn_2O_4$, or $NiCo_2O_4$ [141]	Templating + calcination	Templated assembly: templated nanoparticle assembly	W+D	5–20	Random
Holey Nb_2O_5 [142]		Templated assembly: templated nanoparticle assembly	W+D	28–100	Random
Holey $ZnMnO_4$, $ZnCo_2O_4$ or $CoFe_2O_4$ [140]		Templated assembly: templated nanoparticle assembly	W+D	\	Random
Holey $ZnFeO_4$[143,162]		Templated assembly: templated nanoparticle assembly	W+D	6–13	Random
Holey $MnCo_2O_4$[144]		Templated assembly: templated nanoparticle assembly	W+D	\	Random
Holey Co_3FeN [145]	Calcination	Replacement reaction	W+D	10–12	Random
Holey Mo_2N[163]	Solution method	Catalyzed nitridation	D	10	Random
Holey 2D Li-TMO					
Holey $Li(NCM)O_2$[146]	Calcination	Decomposition	W+D	47	Random
Holey 2D TMDC					
Holey MoS_2[148]	Solution-based etching	Replacement reaction	W	\	Random
Holey $Ni_xCo_{3-x}Se_4$ [149]	Calcination + selenization	Templated assembly: templated nanoparticle assembly	D+W	\	Random
Holey MXene					
Holey MXene [150]	Focused electron beam bombarding	Focused electron beam	D	3–10	Single
Holey LDH					
Holey $NiCo(OH)_2$ [151]	Interdiffusion	Replacement reaction	W	2–50	Random
Holey graphene-like materials					
Holey C_2N [135,137]	Bottom-up	NA	W	0.83	Periodic
Holey Phosphorene [139]	Solution-based etching	High-energy impact: Rapid gas release	W	1-99	Random
Holey h-BN [138]	Solution-based etching	Catalyzed etching: Ag-catalyzed oxidation	D	20–400	Random
Other holey 2D materials					
Holey carbon sheet [164]	Foaming + solution method	HCl etching	W+D	60	Random
Holey N-carbon sheet@graphene [165]	Hydrothermal synthesis + Calcination	Evaporation of pre-occupied atoms (Decomposition)	W+D	2	Random
Holey SiO_2 @MXene [166]	Templating	CTAC pore-making	D	3.1	Random

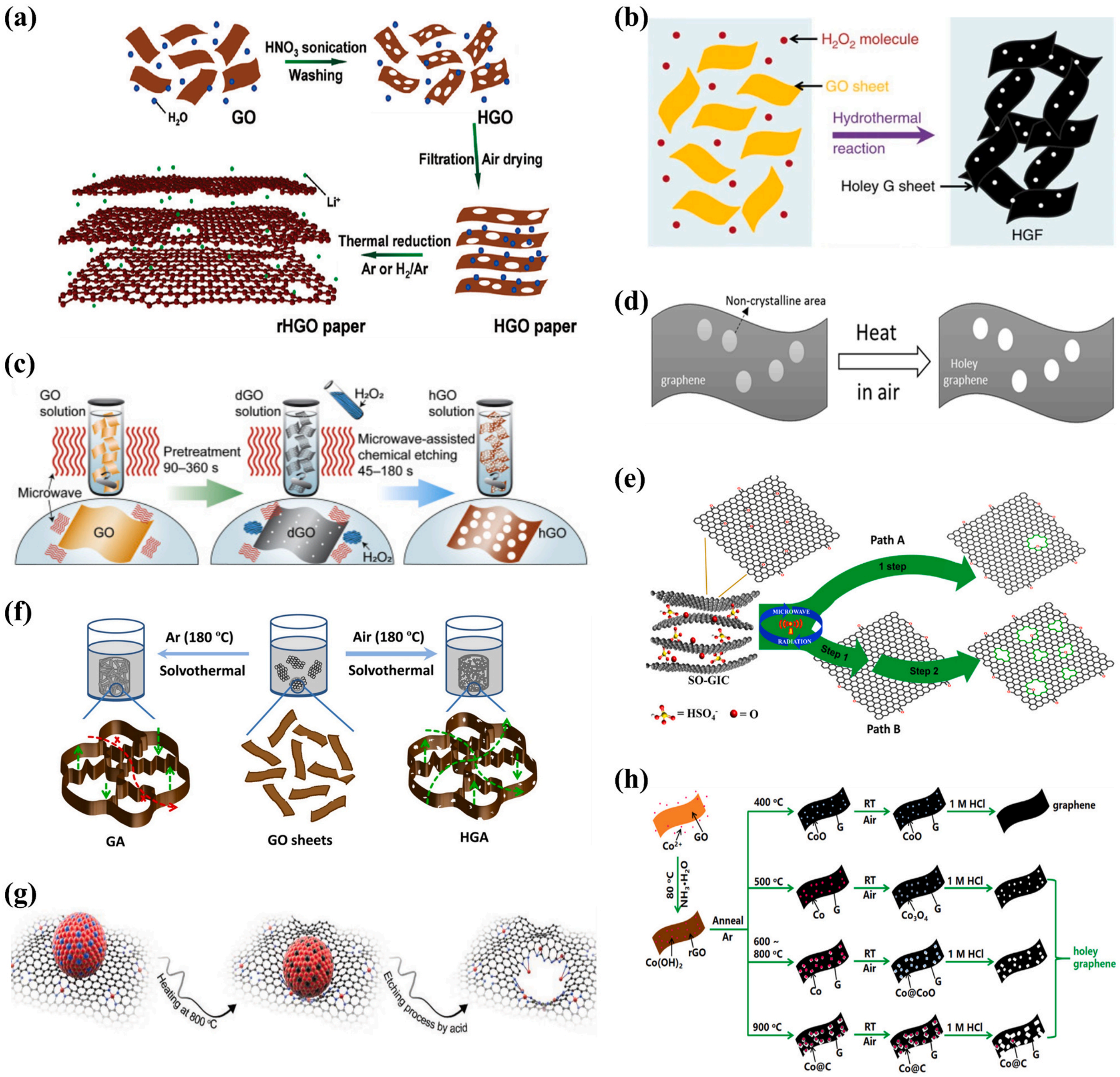

Fig. 12. Oxidative etching for fabricating holey 2D materials: (a) HNO_3 etching, (Reproduced with permission.[29]Copyright 2011, ACS) (b) H_2O_2 etching, (Reproduced with permission.[33]Copyright 2014, Nature) (c) Microwave-assisted H_2O_2 etching, (Reproduced with permission.[61]Copyright 2020, Elsevier) (d) O_2 etching, (Reproduced with permission.[57]Copyright 2014, ACS) (e) microwave-assisted O_2 etching, (Reproduced with permission.[114]Copyright 2018, Elsevier) (f) solvothermal O_2 etching, (Reproduced with permission.[63]Copyright 2016, Elsevier and (g,h) oxide etching. (Reproduced with permission.[82,120]Copyright 2019, Wiley).

In addition, since this H_2O_2 etching method was the most widely used in current literature, several studies conducted atomic simulations through density functional theory (DFT) and molecular dynamics (MD) [61,168] to provide some hypotheses regarding the hole formation mechanism on graphene basal plane. It is agreed that, in the beginning of the etching reaction, the graphene structure is effectively functionalized as a result of an oxidation process that takes place between the layers of H_2O_2 and graphene. This reaction weakens the covalent carbon-carbon bonds that hold the graphene structure intact. Hydroxyl, epoxide, and carboxylic acid groups are all included in the functionalization process. An excessive accumulation of functionalization causes the structure of graphene to become weakened, which in turn causes the carbon atom rings to break apart. As a result, the nucleation stage of the formation of in-plane holes has indeed been initiated. This also results in the collapse of conjugated pi-bonds, which leads to thermal degradation of the graphene sheet. The dissociation of H_2O_2 on graphene has been identified into two distinct processes. The first kind describes the direct interaction of H_2O_2 with graphene, whereas the second type describes the dissociation of H_2O_2 molecules into OH radical species, which then react with the carbon atoms in the graphene layer. Until now, there has been no clear evidence to support any of the above mechanisms. Our group[61] explored the process of holey graphene formation, our calculations demonstrate that there is low possibility of H_2O_2 molecules reacting with pure graphene or pure graphene oxide. However, when H_2O_2 molecules react with defective graphene, they form functionalized graphene structures containing carbonyl, hydroxyl, and hydrogen groups at the edge sites of the defected graphene. Furthermore, our MD simulation findings revealed that the nanoholes are generated by a cyclic etching oxidation process that occurs mostly at the edges of the defective graphene structure. In the following work[167], we investigated the formation of holey graphene and defined the process as a reduction-oxidation-reduction reaction in three stages. The vacancies are created in the first stage using a partial reduction pretreatment. Then, the H_2O_2 molecules preferentially react at the edge-sites of the defective graphene oxide sheets, resulting in functionalization. Finally, by another reduction process, the edge carbon atoms near the defects and their neighbors are removed, forming larger nanoholes.

Etching by O_2. The oxidative etching by directly using O_2 as the etchant is another facile method to fabricate holey graphene since it is commonly known that carbon degrades above 450 °C (Fig. 12**d**). Therefore, this method is mostly achieved through calcination under atmosphere. Generally, 1 g graphene powder is placed in an open-ended tube furnace and heated under ambient to 450 °C for 10 h to obtain holey graphene with nanohole diameters of 5–20 nm.[57,110,154] The long processing time is not very economical and thus limits this method having larger users, while it is practicable for the researchers seeking for obtaining gram-scale holey graphene through simple operations.

K. Savaram et al.[114] reported a microwave-assisted method using graphite intercalation compounds as the staring material instead of GO (Fig. 12**e**). Under rapid heating by microwave irradiation, the oxygen-rich intercalation molecules reacted with carbon atoms and escaped the system, the oxygen in air also participated in the oxidative etching, resulting in simultaneous formation of nanoholes and expansion of graphite layers. Compared to that of the tube furnace heat treatment, the processing time of the microwave method was largely reduced to tens of minutes.

Besides the dry methods, holey graphene can also be fabricated through O_2 etching under wet conditions. P. Zang et al.[63] reported a solvothermal method to fabricate holey graphene, during which the GO solution was purged with air for 1 h before the solvothermal reaction at 180 °C for 36 h (Fig. 12**f**). Whereas this is similar to the H_2O_2 etching method through hydrothermal synthesis proposed by the UCLA group as mentioned above, this method required even longer reaction time possibly due to the lower oxygen concentration in the solution.

Etching by oxides or nitrides. Though not strongly oxidative, oxides or nitrides, such as Fe_2O_3,[121] SnO_2,[62] Co_3O_4,[120] $FeN_{0.056}$,[82] MoO_2,[95] ZnO[158], were found to be successful etchants for creating nanoholes on graphene (Fig. 12**g-h**). By dispersing nanoparticles or precursors of oxides or nitrides onto GO[62,95,120,158] sheets or within inner cells of graphene aerogels[121], the carbon atoms of graphene or GO can be oxidized and partially removed by the oxides or nitrides under annealing at high temperatures. Both inert[95,120,121,158] and ambient[62,120] atmospheres during annealing are found effective for the etching. To obtain pure holey graphene, the nanoparticles are removed by acids[62,120,121] or evaporation[158]. The as-prepared holey graphene has randomly distributed nanoholes with diameters in a range of 2–50 nm. Changing the annealing temperature brings different products and morphologies due to the change of the reactions between the oxides or nitrides and the carbon atoms on graphene, especially for the oxides or nitrides with transition metal atoms of various valance states, e.g. Co_3O_4.[120] This method offers a good solution for the control over the diameter and population of nanoholes on graphene sheets via adjusting the diameter of nanoparticles and the concentration during dispersing, while it requires more delicate processing steps, which often bring more variables and uncertainties during fabrication. Moreover, the annealing time is hours-long, and the process for dispersing or in situ formation of nanoparticles is complicated. This method is favorable to the fabrication of metal oxides-incorporated holey graphene nanocomposites.[95] If the ultimate goal is to obtain just holey graphene, nevertheless, the introduction of foreign nanomaterials can be difficult to eliminate.

Catalytic etching

Catalyzed oxidation. The mediated, catalyzed etching is one of the earliest methods for holey graphene fabrication and first seen in the paper by O. Akhavan[133], who perceived this idea referring to the studies on photodegradation of graphene sheets using semiconducting TiO_2 or ZnO (Fig. 13**a**). Upon UV irradiation for 10 h, holey GO was obtained with nanohole diameters of ca. 200 nm. The author proposed that the UV photons excited electronic holes on the surface of the ZnO nanorods and caused the oxidation of hydroxyl groups originally attached to the ZnO nanorods, forming hydroxyl (OH•) radicals, which etched the carbon atoms around the contacting regions between the ZnO nanorods and GO sheet. J. G. Radich et al.[160] used Au nanoparticles as the photocatalysis medium absorbing laser irradiation and catalyzing the transformation of H_2O_2 to OH• radicals, which oxidize and etch the carbon atoms on the rGO sheets (Fig. 13**b**). It was also proposed that the irradiation-caused decomposition of H_2O_2 to O_2 and H_2O was a competing process which reduced the formation of OH• radicals for etching.

Y. Lin et al.[156] employed Ag nanoparticles as the medium to catalyze the oxidative etching of graphene sheets (Fig. 13**c**). The etching was carried out in an open-ended furnace, and the Ag@graphene powders were heated at 300 °C for 3 h in air to obtain holey graphene with nanohole diameters of ranging from 10^1 to 10^2 nm. Different from the photocatalyzed etching, the Ag-catalyzed oxidative etching relies on O_2 instead of OH• radicals. C. Guo et al.[157] reported that the average nanohole diameters of ca. 5, 20, 25, 100, and 150 nm were obtained with the ratio of the Ag precursor to GO of 1:20, 2:20, 3:20, 6:20, and 8:20. E. Alsharaeh et al.[81] prepared Ag@rGO via the microwave-assisted method and obtain similar holey graphene structures using the same etching process.

Holey h-BN can also be prepared by the Ag-mediated, catalyzed etching as reported by Y. Liao et al.[138] They used Ag nanoparticles as the medium to catalyze the oxidation of and the formation of nanoholes on h-BN under annealing at 800 °C. The nanoholes with diameters of ca. 20–80 or 200–400 nm were obtained by annealing of 1 or 10 h, respectively.

Catalyzed nitridation. G. Sun et al.[163] manufactured holey Mo_2N nanosheets via a catalyzed nitridation method using CaO as the catalyst and NH_3 as the nitrogen source. To achieve the nitridation, MoS_2 powder was mixed with CaO powder and then annealed under NH_3 gas flow at 820 °C for 3 h. The average pore size was 10.5 nm, bringing a relatively high BET specific surface area of 42.28 $m^2\ g^{-1}$. This study demonstrated that no holey structure was observed after the same nitridation process of MoS_2 powder without the addition of CaO.

Catalyzed hydrogenation. While most catalytic etching reactions induced by metals are oxidative, some studies show that metals can also lead to catalytic etching of graphene through hydrogenation (Fig. 13**d**).[127] By direct observation of Fe nanoparticles etching graphene along its crystallographic directions, S. S. Datta et al.[169] propose that the existance of Fe nanoparticles catalyzes the reaction between carbon atoms on the graphene lattice and hydrogen atoms from the annealing atmosphere. The same phenomena are observed in the annealing of Ni[170] or Cu[171] nanoparticle-deposited graphene.

Replacement etching

Metal atom replacement. D. Sarkar et al.[148] prepared holey Mo-rich MoS_2 by the replacement reaction between Ag^+ ions and MoS_2 forming Ag_2S and removing S atoms of MoS_2 sheets (Fig. 14**a**). The obtained holey MoS_2 had randomly distributed nanoholes with diameters of 3–5 nm.

N. L. W. Septiani et al.[151] prepared holey Fe-doped NiCo layered

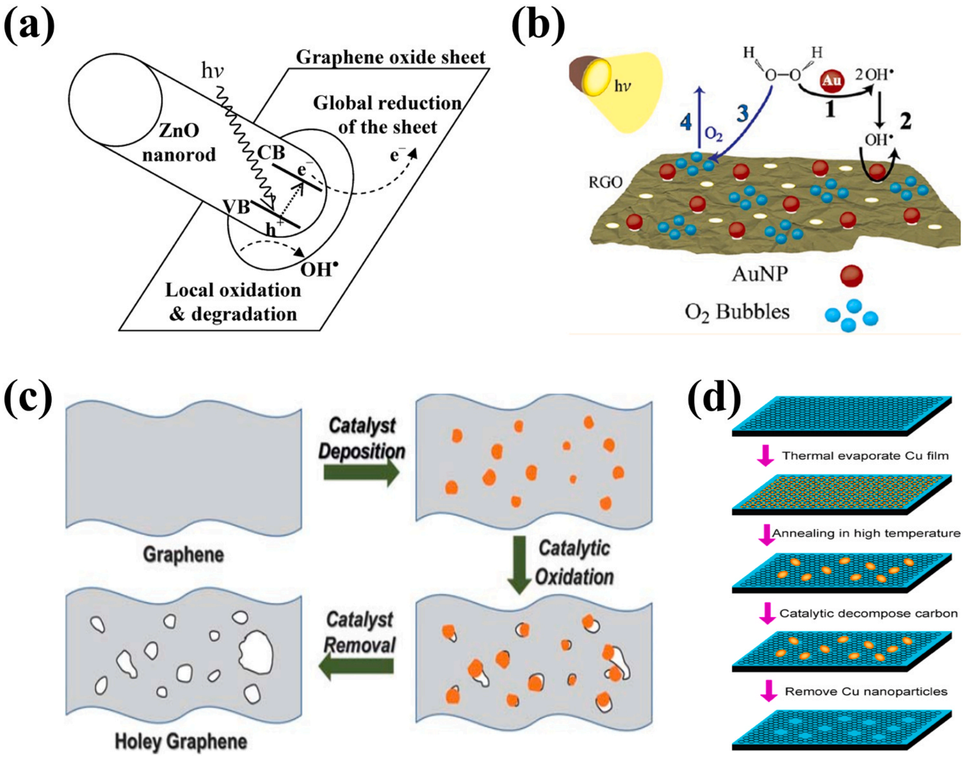

Fig. 13. Catalyzed etching: (a) ZnO nanorod catalyzed etching, (Reproduced with permission.[133]Copyright 2010, ACS) (b) Au nanoparticle catalyzed etching, (Reproduced with permission.[160]Copyright 2013, ACS) (c) Ag nanoparticle catalyzed etching, (Reproduced with permission.[156]Copyright 2013, RSC) and (d) Cu catalyzed hydrogenative etching. (Reproduced with permission.[127]Copyright 2012, ACS).

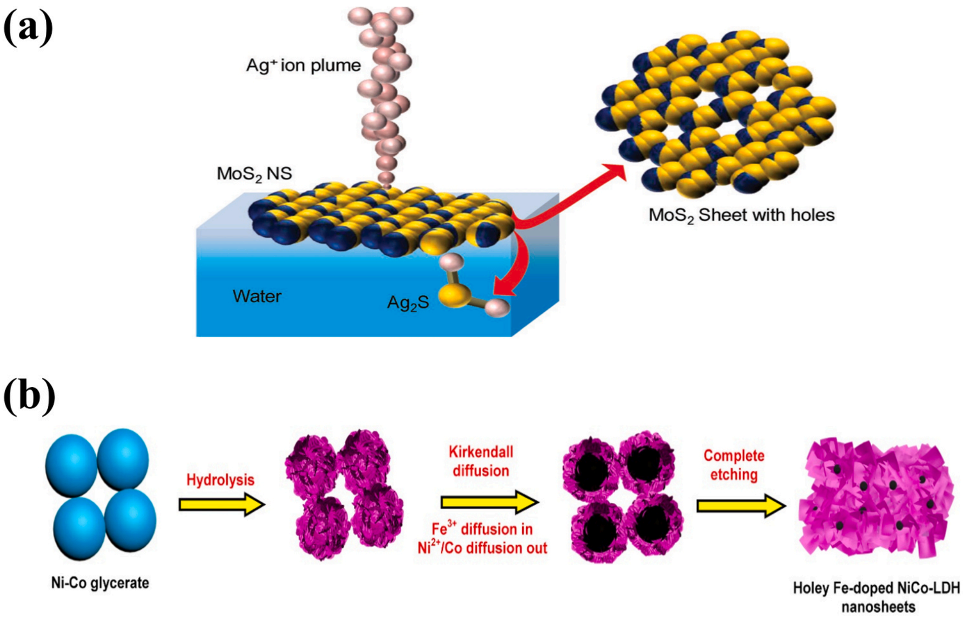

Fig. 14. Etching via replacement reaction: (a) Ag+ replacing S atoms; (Reproduced with permission.[148]Copyright 2018, Wiley) (b) Fe^{3+} replacing Ni^{2+}/Co. (Reproduced with permission.[151]Copyright 2020, Wiley).

double hydroxide sheets by interdiffusion-caused replacement of Ni^{2+}/Co in the Ni–Co glycerate spheres by Fe^{3+} ions during hydrothermal synthesis (Fig. 14**b**). The as-prepared holey sheets had pores with a prominent diameter range of 2–50 nm.

Non-metallic replacement. H. Guo et al.[145] manufactured holey Co_3FeN nanosheets with average nanohole diameters of 10–12 nm by annealing Co_3Fe layered double hydroxide with NH_3 under 500 °C for 1 min with a ramping rate of about 10 °C/min. The nitrogen atoms replaced the hydroxide groups, causing the phase transformation that further led to the formation of nanoholes. G. Sun et al.[163] used the similar method to fabricate holey molybdenum nitrides nanosheets, and they added CaO to absorb byproducts and thus promoted the replacement reaction between NH_3 and MoS_2.

High-energy impact

Rapid gas release. Y. Peng et al. [60] reported that the rapid heating of graphene powder in air led to the formation of holey graphene due to fast accumulated gaseous products punching through the basal planes of graphene sheets. In this study, the quartz tube was firstly heated to 300 °C and held for 30 min before directly dropping graphene powder in the tube, which resulted in the rapid heating with an ultra-high rate of 100 °C/s (or 6000 °C/min). The randomly distributed nanoholes with diameters of 10–250 nm could form in just about 2–3 s. They also confirmed that for the final temperature of 300 °C during the tube furnace heating of graphene powder, the heating rate lower than 60 °C/min could not bring obvious formation of nanoholes. C. Yang et al. [31] reported that by directly transferring graphene powder to the heated tube under 300 °C with an estimated heating rate of > 6000 °C/min, the holey graphene with nanohole diameters of 50–100 nm was obtained as illustrated in Fig. 15**a**. For the final temperature of 1100 °C during the tube furnace heating of graphene powder, the increase of the heating rate between 300 and 3000 °C/min caused the formation of nanoholes with higher diameters and populations.

Besides holey graphene, holey black phosphorous was reported being fabricated by the rapid gas release method. [139] By first intercalating Na particles in between black phosphorous layers using an electrochemical route, a large amount of gas formed after contacting with water and punched randomly distributed nanoholes with diameters of 1–99 nm on the basal planes of black phosphorous (Fig. 15**b**).

Focused electron beam bombarding. Focused electron beam bombarding is a highly delicate processing method used to create a single nanohole with a designed nanohole diameter on 2D nanomaterials for single molecule processing such as DNA sensing, translocation, sequencing, etc. G. F. Schneider et al. [128] reported using the focused electron beam to bombard single nanoholes with diameters of 2–40 nm on graphene. During the process, a mechanically exfoliated graphene sheet was transferred onto a 20 nm SiN_x coated Si/SiO_2 substrate with a preformed 5 μm hole and then shot by a 300 kV focused electron beam in a TEM. Both single-layer and multilayer (≤8) graphene nanosheets were successfully bombarded to form single nanoholes. Single-hole MXene nanosheets with nanohole diameters of 3–10 nm were also fabricated by focused electron beam bombarding as reported by M. Mojtabavi et al. [150] They first transferred MXene flakes onto a 50 nm SiN_x coated Si/SiO_2 substrate, which was pretreated by the focused ion beam to obtain a 100 or 200 nm hole, and then shot a focused electron beam to the MXene flake in a TEM (JEOL 2010FEG) with spot sizes of 3–5. Similar studies were also reported using this method in Fig. 15**c** to obtain single-hole MoS_2, [172] WS_2, [173] BN, [174] etc.

Decomposition

Transition metal hydroxides can decompose to oxides under calcination at high temperatures, and this method is broadly used for fabrication of lithium transition metal oxides for Li-ion battery cathodes. Y. Wu et al. [146] first prepared double layered hydroxide nanosheets of $Ni_xCo_{1-x}(OH)_2$ and then slightly altered the above calcination method by adding the pre-calcination at 500 °C before the final calcination at 750 °C to retain the nanosheet morphology and simultaneously introduce the nanohole feature. They finally obtained a series of holey lithium transition metal oxide nanosheets including $LiCoO_2$, $LiNi_{0.8}Co_{0.15}Al_{0.05}O_2$ (NCA), $LiNi_{0.8}Co_{0.1}Mn_{0.1}O_2$ (NCM811), $LiNi_{0.6}Co_{0.2}Mn_{0.2}O_2$ (NCM622), $LiNi_{0.5}Co_{0.2}Mn_{0.3}O_2$ (NCM523).

Templated assembly and deposition

Templated assembly method uses GO and rGO as templates for synthesis of holey 2D metal oxide nanosheets (Fig. 16**a-c**). D. Chen et al. [141] fabricated holey Co_3O_4 by conjugating Co_3O_4 nanocrystals into a free-standing 2D structure, during which 2D structure of GO modified with sufficient oxygen-containing functional groups promoted the growth of metal ion on its surface. L. Peng et al. [140] reported a general two-step strategy for controlled synthesis of holey 2D TMO nanosheets

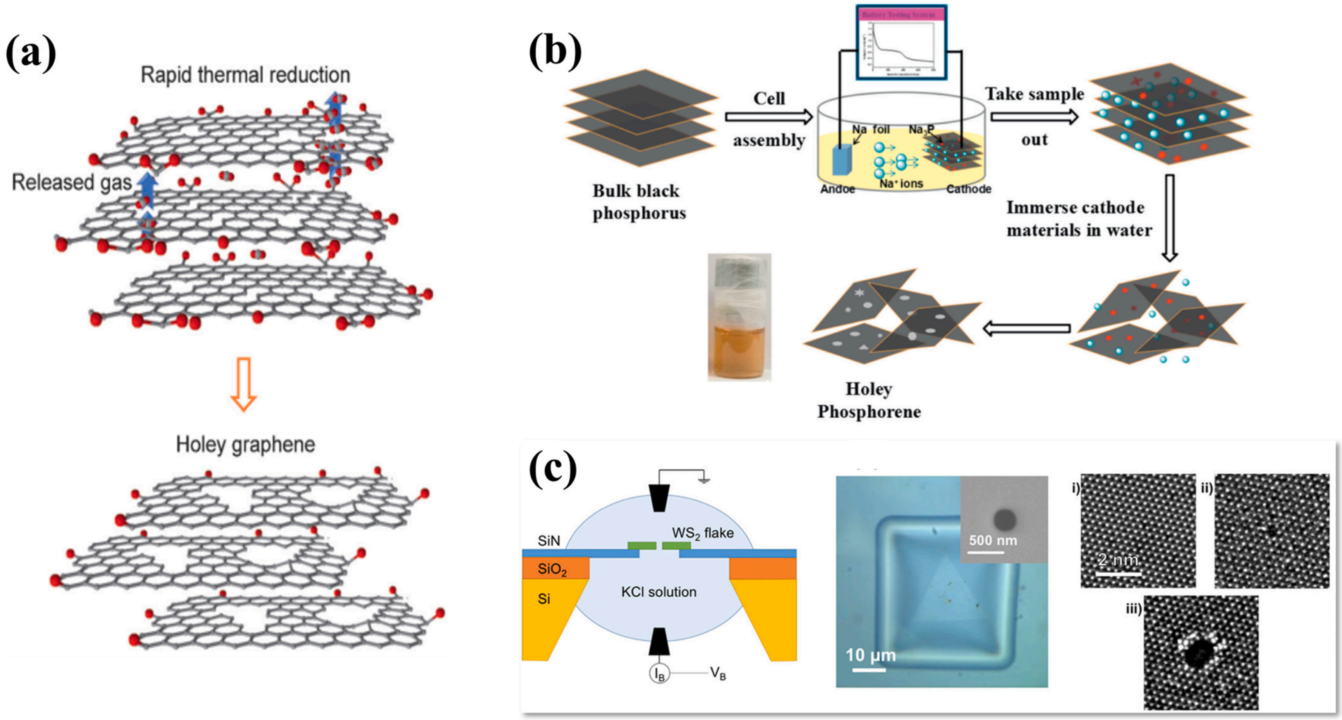

Fig. 15. High-energy impact: (a) rapid heating for holey graphene fabrication; (Reproduced with permission. [31] Copyright 2015, Wiley) (b) electrochemical intercalation for holey black phosphorous fabrication; (Reproduced with permission. [139] Copyright 2019, Elsevier) (c) focused electron beam bombarding for single-hole 2D nanosheets. (Reproduced with permission. [173] Copyright 2017, ACS).

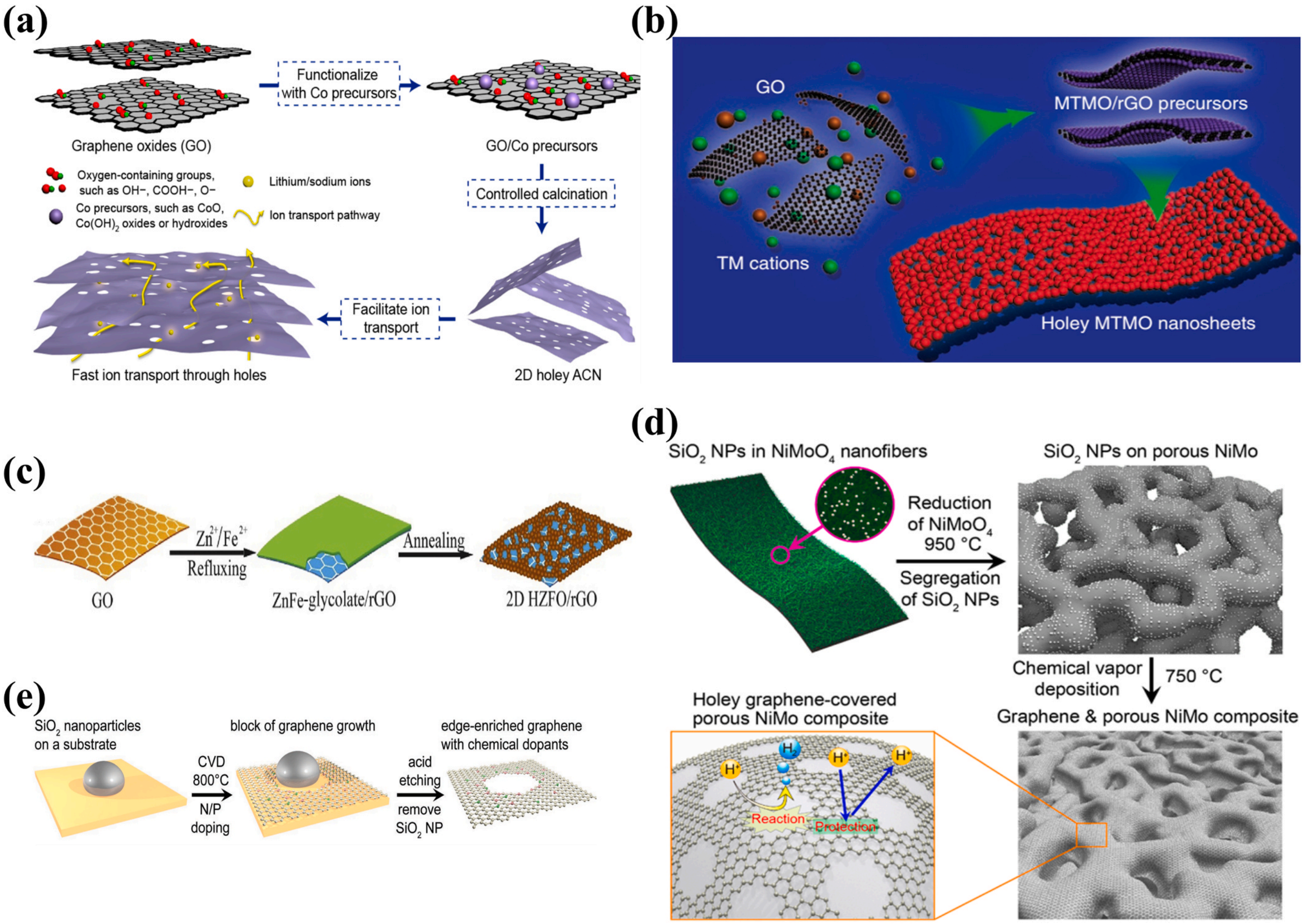

Fig. 16. Templated assembly: (a–c) GO templated assembly of holey metal oxide nanosheets; (Reproduced with permission.[141] [140] [143]Copyright 2017, ACS; 2018, Elsevier) (d,e) templated CVD. (Reproduced with permission.[112] [113]Copyright 2018, ACS; 2019, Wiley).

with tunable pore sizes using graphene oxides as a sacrificial template. This approach has been demonstrated to synthesize various 2D holey TMO nanosheets, including simple oxides such as Fe_2O_3, Co_3O_4, Mn_2O_3, and mixed oxides such as $ZnMn_2O_4$, $ZnCo_2O_4$, $NiCo_2O_4$ and $CoFe_2O_4$, through growth of TMO precursors on GO surface followed by chemical interconnection of TMO nanoparticles and controlled decomposition of GO templates. W. Yao et al.[143] reported a method to synthesize the holey $ZnFe_2O_4$ nanosheet/rGO composite by the self-assembly of ZnFe-glycolate/rGO precursor. Templated CVD is a bottom-up method for synthesis of high-quality holey 2D materials by presetting nanoparticles on the template to block local growth. Y. Ito et al.[112] first decorated NiMo nanofibers with 18–27 nm SiO_2 nanoparticles and then used them as the templates to grow graphene via CVD as shown in Fig. 16**d**-**e**. The existence of SiO_2 nanoparticles prevented the growth of graphene lattice in these regions, and therefore the nanohole features could be effectively controlled by the concentration and size of SiO_2 nanoparticles on the NiMo template. A. Kumatani et al.[113] also used the same method to prepare holey graphene@NiMo nanofibers and found the nanohole diameter ranged from 0.01 to 1 μm.

Manufacturing periodic holey structures on 2D crystals

The manufacturing methods of the 2D nanomaterials with periodic distribution of nanoholes are the bottom-up chemical assembly and various types of lithography. To obtain the periodic patterns of nanoholes on the atomic level, the bottom-up chemical assembly requires the precursor molecules having the specific ligands that only allow a certain ordered arrangement of the molecules. In terms of lithography, the preparation of the preform is the key to manufacture the periodic patterns of nanoholes.

Lithography

Block copolymer lithography. The block copolymer lithography (Fig. 17**a**-**b**) with O_2 plasma as the etchant (also referred as reactive ion etching, RIE) is generally employed to fabricate the semiconductor-level graphene nanomesh and was first reported by J. Bai et al.[28] They placed a mechanically peeled graphene sheet on a silica substrate and then coated a SiO_x intermediate layer and a poly(styrene–block–methyl methacrylate) (P(S–b–MMA)) block copolymer thin film. The UV exposure and glacial acid development removed PMMA from the block copolymer layer leaving the cylinder domains constructed by PS frames. Then, O_2 plasma was used to remove exposed random copolymer and control the thickness of PS frames, and the underneath SiO_x film was further etched by CHF_3 plasma to expose the templated regions of the graphene sheet, which was finally etched by O_2 plasma to form periodical in-plane nanoholes with average diameters of 17.7–31.9 nm and average neck widths (the shortest distance between the edges of two nanoholes) as low as 5 nm. This method aims to create high-density nanoholes on graphene with precisely controlled diameters and neck width, which significantly affect the charge transport behavior of graphene and its performance in field-effect transistors. The O_2 plasma etching is much more active than the general O_2 etching mentioned above, reducing the etching time down to seconds, while it requires much more time for the pretreatment and posttreatment relative to the

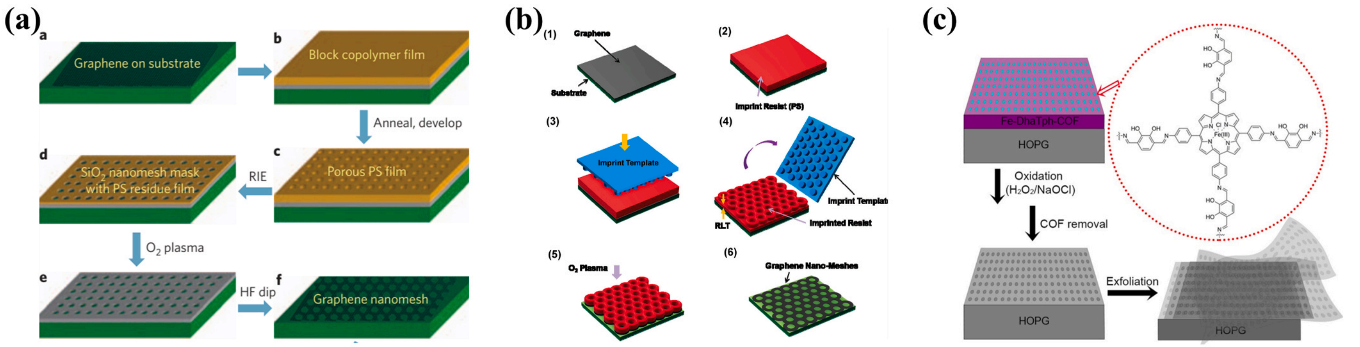

Fig. 17. Lithography: (a,b) block copolymer lithography; (Reproduced with permission.[28] [130]Copyright 2010, Nature) (c) covalent organic framework lithography. (Reproduced with permission.[153]Copyright 2017, Wiley).

latter. The vital point of this method is templating, which determines the distribution and pattern of nanoholes as well as the neck width. Though expansive and complicated, this method is effective in fundamental explorations of novel properties of holey 2D materials, especially in the field of electronics. X. Liang et al.[130] used a male copolymer layer to create an imprinted template on a polymeric intermediate layer for creating nanoholes on graphene. The average neck width was controlled between 7 and 17 nm by adjusting the plasma etching time from 10 to 30 s. To avoid using toxic etchants like CHF_3 and CF_4 and degrading the SiO_2/Si substrate, as well as to lower the cost, Z. Zeng et al.[131] used an

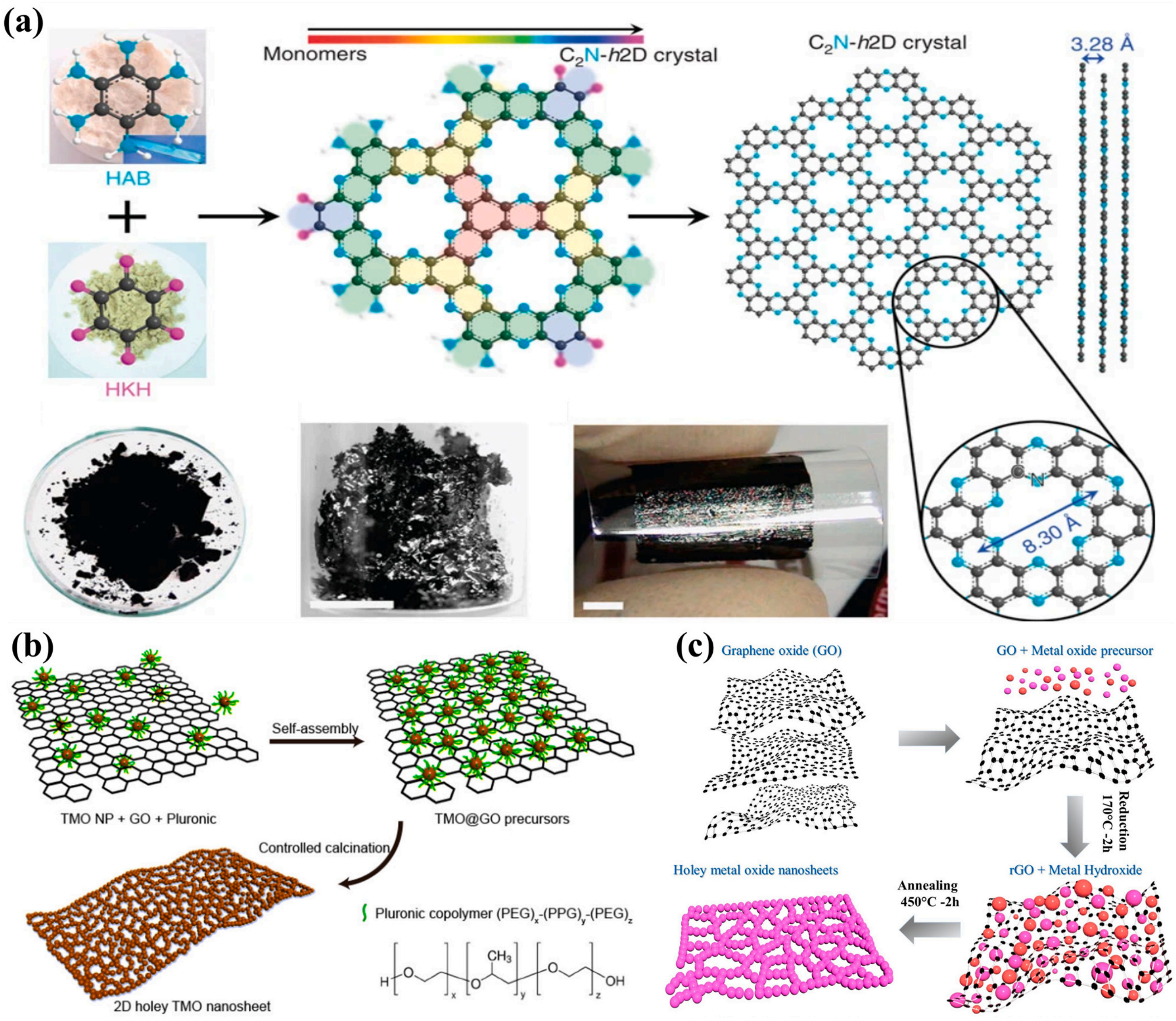

Fig. 18. (a) Bottom-up synthesis of holey C_2N. (Reproduced with permission.[135] Copyright 2015, Nature) (b,c) Schematic illustration of manufacturing fused particle nanosheets. (Reproduced with permission. [144] [162]Copyright 2017, ACS; 2019, Elsevier).

anodic aluminum oxide mask as the template for creating nanoholes on graphene with neck widths of 33 or 15 nm by etching for 30 or 40 s under O_2 plasma. Y. Yang et al.[125] employed the block copolymer lithography to etch the high-quality graphene sheets synthesized via CVD. Average hole sizes of ca. 0.55, 0.63, and 1.41 nm can be obtained by O_2 plasma exposure of 5, 10, and 20 s, respectively.

Covalent organic framework lithography. The strategy of covalent organic framework (COF) lithography (Fig. 17**c**) employs a bifunctional, metalated COF which serves as a surface catalyst and a master template for creating holes on graphite that is subsequently exfoliated into multiple patterned graphene sheets. W. Seo et al.[153] grew metalloporphyrin COF on highly ordered pyrolytic graphite and chemically etched and exfoliated graphene layers with H_2O_2 and NaOCl solutions. Using a similar method, D. L. White et al.[161] grew COF-5 particles on a CVD-grown graphene sheet and employed RIE to etch the exposed areas of the graphene sheet, but they obtained randomly distributed dense nanoholes on graphene sheets.

Bottom-up chemical synthesis

J. Mahmood et al.[135] reported a simple and scalable chemical synthesis route of holey C_2N (Fig. 18a) by slowly adding NMP and a few drops of sulfuric acid or trifluoromethanesulfonic acid into the mixture of hexaaminobenzene (HAB) trihydrochloride and hexaketocyclohexane (HKH) octahydrate and then heating with oil bath at 175 °C for 8 h. The obtained C_2N nanosheets exhibited a layered structure with an inter-planar distance of 0.328 nm, periodically distributed sub-nanoscale holes with an inter-distance of ca. 0.824 nm. The BET surface areas of the holey C_2N nanosheets before and after annealing under argon at 700 °C were 26 and 281 $m^2 g^{-1}$. In a study of this process mechanism, Mortazavi *et al.*,[175] conducted atomic simulations and found that the carbon-carbon bonds break under strain along the perpendicular to the loading direction, resulting in the formation of substantial triangular voids comprised of mono-atomic chains, then eventually the formation of larger holes in the material. Their calculations also revealed that as temperature rises, the elastic modulus and tensile strength of the nitrogenated holey graphene decrease.

Manufacturing fused particle nanosheets

Templated nanoparticle assembly

Templated nanoparticle assembly is a method largely used in fabrication of holey TMO nanosheets (Fig. 18b-c). The as-prepared holey TMO nanosheet is not formed by 2D lattice. Instead, it is composed of conjoined nanoparticles with randomly distributed void spaces in between them. Generally, the precursors are adsorbed by a sacrifice 2D template (usually GO), and after calcination in air, they form oxide nanoparticles connecting with each other, while the template is burnt. Two steps are essential to the fabrication: i) linking the precursor to the template and ii) parameter control to obtain desired sintering, unit particle sizes, and nanohole diameters. GO is usually the template. Besides its superior properties such as the specific surface area and mechanical strength, GO provides the active functional groups, including carboxyl, hydroxyl, and epoxy groups, to facilitate the growth of the TMO precursors and anchor TMO particles covalently. Without GO as the template, the holey 2D structure cannot be obtained.[140].

D. Chen et al.[141] reported a GO-templated nanoparticle assembly for fabrication of holey Co_3O_4 nanosheets. In this study, GO–ethylene glycol solution and cobalt acetate solution were mixed and stirred for over 1 h and then refluxed at 170 °C under oil bath for 2 h. The collected precipitates were annealed at 500 °C in air for 2 h by a ramping rate of 0.5 °C/min to fabricate the holey nanosheets assembled by Co_3O_4 nanoparticles. Higher Co precursor concentrations led to higher average nanohole diameters changing from 5 to 20 nm and higher average unit particle sizes changing from 8 to 45 nm. The nanohole feature could not retain if the annealing temperature was above 800 °C. This method was also effective to fabricate the holey nanosheets of Fe_2O_3, Mn_2O_3, $ZnMn_2O_4$, $NiCo_2O_4$, [141] Nb_2O_5[142] and $MnCo_2O_4$[144] respectively. L. Peng et al.[140] fabricated holey nanosheets of $ZnMn_2O_4$, $ZnCo_2O_4$, $NiCo_2O_4$, and $CoFe_2O_4$ with uniform lateral sizes (ca. 500 nm) and nanosheet thickness (ca. 20 nm) and found that the calcination temperature was a vital factor to the morphology and electrochemical performance of these materials. Higher calcination temperatures in the range of 400–600 °C resulted in larger sizes of both nanoholes and individual nanoparticles, and the calcination temperature higher than 600 °C led to the aggregation of nanoparticles, which was unfavorable to the performance in lithium-ion batteries. By slightly altering this method, W. Yao et al.[143] fabricated holey $ZnFe_2O_4$ nanosheets@rGO nanocomposites. When the block copolymer was added during the mixing step, and the areal occupation ratio of metal oxides on GO sheets could be tuning by the molecular weight of the block copolymer so the final nanohole diameter was further effectively adjusted.[162] Z. Fang et al.[149] added a selenization step after obtaining holey $NiCo_2O_4$ nanosheets and fabricated holey $NiCo_2Se_4$ nanosheets with similar morphology as its precedent.

Characterization methods

The development of manufacturing processes for holey 2D materials requires characterization techniques to investigate the resulting holes. The hole size can range from few nanometers to hundreds of nanomaterials and the 2D materials can be conductive or non-conductive, thereby a variety of characterization techniques has been utilized priorly. This section will briefly summarize the existing characterization methods for holey 2D materials and classify them into two categories: direct observation by microscopy techniques and indirect measurements. Typically, all these methods are developed from common techniques for nanoparticle characterization.

Direct observation by microscopy techniques

Microscopy techniques are widely used for direct observation of the morphology of holey 2D materials, providing visual images of nanoholes directly. Two types of microscopy techniques used in existing literature are electron microscope (EM) and atomic force microscope (AFM).

EM takes advantage of the short wavelength of electrons to form images, rendering ultra-high resolution for investigating nanoholes. The most commonly used EM is Scanning Electron Microscope (SEM), which is typically employed to observe nanoholes larger than tens of nanometers. The SEM observation relies on the secondary electrons excited and emitted from atoms by an electron beam and then the detection facilitated by a secondary electron detector, thereby it requires the objects (i.e. 2D materials) to be electrically conductive. For holey 2D materials with inadequate electrical conductivity, a thin conductive coating from gold evaporation has been demonstrated as an effective strategy. On the other hand, when the size of nanoholes is small, e.g., less than 10 nm, the transmission electron microscope (TEM) is more preferably used for the observation. Rather than the collection of secondary electrons in SEM, TEM uses transmitted electrons interacting with internal structures of the specimen and therefore is able to realize a much higher resolution. For instance, existing studies have utilized high-resolution TEM (HRTEM), aberration-corrected TEM, and scanning transmission electron microscope (STEM) to characterize nanoholes in 1–2 nm, as illustrated in Figs. 2, 7, 9, and 10. It is also noteworthy that though TEM can produce high resolution images of nanoholes, it can only observe a small area, whereas SEM is better for 3D surface morphology characterization.

In contrast to EM that requires specimen with high electrical conductivity, Atomic Force Microscopy (AFM) can be used to characterize holey 2D materials with inadequate conductivity. AFM is versatile in characterizing both electrically conductive and less conductive samples by scanning the surface with a mechanical probe. The AFM technique can generate topographic images of the surface, e.g., holey 2D materials dispersed on an atomically flat substrate. Through measuring the surface profile of the holey 2D material and the height difference from the non-holey area to holey area, the size of nanoholes can be characterized. With demonstrated resolution on the order of sub-nanometer scale, AFM has been utilized in current literature to characterize the size and size distribution of nanoholes and the thickness of holey 2D materials. However, the reader should be aware that AFM observation of holey 2D materials might require a careful sample preparation process, such as dispersing them onto a substate with atomic-flat top surface and avoiding their stacking.

Indirect measurements

Other techniques for indirect measurements of nanoholes in holey 2D materials have also been developed, such as various adsorption/desorption isotherms which can determine the specific surface area (SSA) and total pore volume, then the pore diameter and size distribution can be calculated accordingly. Two most common techniques will be discussed as follows.

Brunauer-Emmett-Teller (BET) analysis measures SSA of solid holey 2D materials by gas adsorption/desorption. This technique is based on BET theory, which is extended from the Langmuir theory and builds an ideal model for multilayer adsorption following some simple hypotheses. This technique is widely used to measure the SSA of holey graphene, and a typical result is shown in Fig. 19**a**. The BET isotherms plot the SSA change as the relative pressure of nitrogen gas increases from 0 to 1 (adsorption) and decreases back to 0 (desorption). The linear section under low pressure is used to calculate SSA, which ranges from 552–763 m^2/s here, suggesting the increase of porosity by introduction of nanoholes on graphene sheets.

Barrett-Joyner-Halenda (BJH) analysis determines pore size distribution on mesoporous materials. BJH measurement is often incorporated with BET measurement and performed simultaneously. The quantity of adsorbate (N_2 in most case) removed from the pores is calculated by the modified Kelvin equation, and a typical result is shown in Fig. 19**b.** By calculating the surface area of pores, the pore volume and pore size can be determined, generating the plot of pore radius distribution.

Conclusion and future outlook

In summary, holey 2D materials show many advantages over their predecessors, leading to a broad range of potential applications in electrochemistry, bioscience, optoelectronics, thermoelectric, and among others. In sections above, we have summarized the important applications and categorized and compared the currently developed manufacturing processes for holey 2D materials. The discussion in this section will try to cover a few topics related to the current manufacturing challenges, physical properties of holey 2D materials and future outlook in this field.

Challenges of current manufacturing and future outlook

The manufacturing of holey 2D materials at large scale with controlled hole characteristics is of critical importance for specific applications but remains a major challenge. Table 4 summarized the current manufacturing methods which are grouped by their raw materials, treatment, hole-formation mechanisms, dry/wet process, hole size and random/periodic hole patterns. By analyzing these existing methods, we identify the manufacturing challenges are centered on three aspects: scalability, controllability, and manufacturing process mechanism understanding.

The first challenge of the current manufacturing is scalability, and most previously developed methods in Table 4 are difficult to scale up. The wet etching processes strongly depend on the solution-based chemical reactions. The environmental impacts of the used aggressive etchants and dispersion solvents become more considerable in scale up production. And since the solutions usually only contain low concentration of the 2D materials due to the dispersion issues, the energy input required to activate the etching reactions are typically consumed by the solution solvents, thus resulting in low energy efficiency and scalability. To improve the scalability of the wet etching processes, environmentally friendly chemical etchants and solvents are preferred, and the more efficient energy delivery methods are also attractive. For instance, several recent studies explored using microwave, laser, UV irradiation, etc., to selectively deliver energy to 2D materials in solutions and then activate the etching reactions which might shed light on energy-efficient wet etching process development. On the other hand, the dry etching methods use dry powders and chemicals as raw materials are certainly more feasible for production in large amounts. However, it has been reported difficult to uniformly mix 2D materials dry powder with chemical etchants or uniformly disperse the etchant to every 2D material flake due to the nature re-stacking issue. This leads to significant variations of etching reactions from batch to batch and even in one single batch production. In addition to wet/dry etching methods, there are other processes use nanoparticle templated assembly, bottom-up

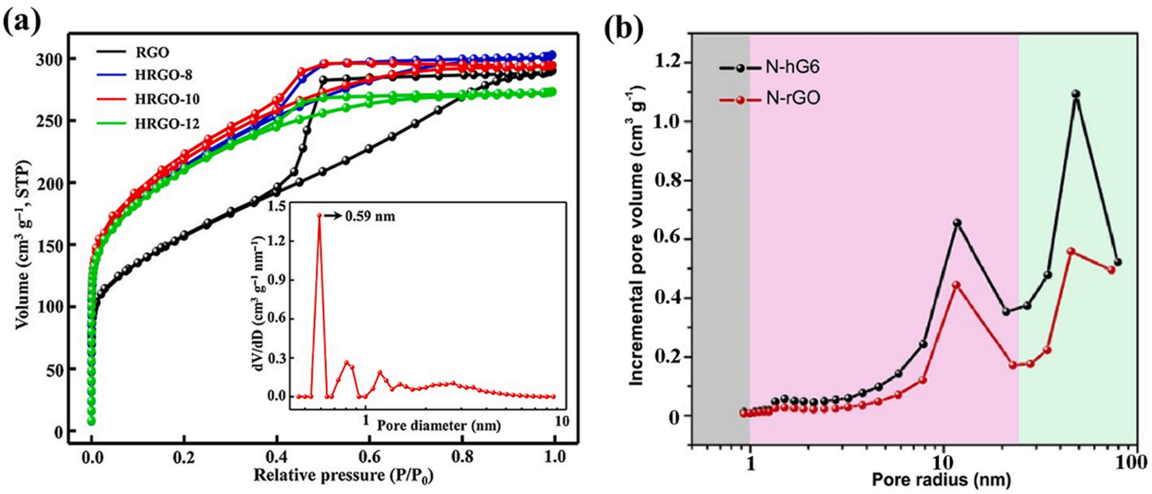

Fig. 19. (a) Adsorption/desorption isotherms of holey graphene by BET (Reproduced with permission.[59] Copyright 2016, Elsevier). (b) Pore size distribution of nitrogen-doped holey graphene calculated by BJH analysis (Reproduced with permission.[104] Copyright 2020, Elsevier).

assembly, plasma etching/lithography and focused ion beam bombarding, while these processes are naturally even more difficult to scale up due to the challenges in handling of nanoparticles/assembly process and the requirements of expensive plasma/ion beam, masks as well as high vacuum chambers, etc.

The second challenge of current manufacturing is the inadequate controllability of the hole size and hole patterns in these processes. Table 4 summarized that the size of the holes fabricated on current 2D materials can vary from as small as 0.63 nm to as large as 600 nm. Among wet etching processes, mild etchant like H_2O_2 render the best control over hole sizes which generally produces single digit holes (<10 nm) with small size variations. When aggressive etchants or catalysts are used in the processes, the fast reaction kinetics generally led to a much larger size variations of the holes, e.g., ranging two orders of magnitude (10^0-10^2 nm). Using nanoparticle template to direct the assembly, the variations of hole size can be controlled to a smaller range, while the obtained holes are generally larger than H_2O_2 etched ones but comparable to ones by other aggressive etchants. Both the etching processes and template-directed synthesis approaches yield random hole patterns with minimum controllability in hole size or size variations. If holes are required to be controlled to periodic patterns or single size holes, current lithography-based processes, bottom-up synthesis or focus ion beam approaches can be used but in high cost and low scalability. Therefore, there is a tradeoff between the controllability and scalability for current manufacturing. Novel methods that can achieve desired controllability without sacrificing scalability would mark a major advancement in not only manufacturing process but also large-scale applications.

The third challenge of current manufacturing is about the physics understanding of manufacturing process mechanisms. Up to date, there are very limited research focusing on the manufacturing mechanisms of holey 2D materials, though a small number of computational studies have tried using atomic simulations including density functional theory (DFT) and molecular dynamics (MD) simulations to understand the hole formation on 2D flakes. In spite of these advancements, the utilization of DFT and MD simulations has been challenging. DFT simulation is accurate but limited to hundreds of atoms, thereby the models are far smaller than desired ones typically requiring 2D flakes containing nanometer to tens of nanometers sized holes. MD simulations allow the modeling of larger structures of 2D flakes; however, the precise depiction of interatomic interactions is lacking due to the classical empirical potentials are used. To tackle these challenges, recent machine learning models are promising, such as neural networks (NN) models have made rapid progress in combining DFT and classical simulations to create interatomic potentials of materials. These modeling studies can help understand the mechanisms that are not easily observable in experiments. However, besides development of novel modeling tools, validation of these computation models on graphene and other holey 2D materials are needed, such as by close comparation to in-situ monitoring of hole forming process and ex-situ holey 2D materials characterizations. Therefore, to reveal the process mechanisms and improve manufacturing scalability-controllability for holey 2D materials, both in-process monitoring tools and ex-situ characterizations are called for. In-process monitoring of temperature, pressure, radicals, chemical species, etc., combining with ex-situ characterizations of 2D flakes, holey structure, edge sites atoms, functional groups, physical properties, electrochemical characteristics, etc., are critical for the physics understanding of process mechanisms.

Physical properties of holey 2D materials and future outlook

Electrochemical, chemical, and mechanical properties: Firstly, the introduction of holes onto 2D materials is a double-sided sword affecting electrochemical properties and thus need to be addressed for practical applications. For instance, the electrical conductivity of holey 2D materials is generally lower than that of pristine counterparts due to the degradation of lattice structure. However, the increased ion diffusion and enlarged specific surface area due to holey structure can accommodate the decrease in electric conductivity, and eventually boost up the electrochemical energy storage capability in devices. This accommodation might be alleviated if the 2D material restacks together during assembling process and leads to limited interlayer spacing for ions to travel. Therefore, for large-scale utilization of holey 2D materials in practical electrochemical applications, it is of critical importance to prevent the restacks of 2D flakes through methods such as compositing with spacer fillers (e.g., nanoparticles, nanotubes, flakes, etc.) or assembly into three-dimensional structures (e.g., aerogel, frameworks, foams, etc.). Secondly, the performance stability of holey 2D materials could be compromised over long-term periods since the edge-site atoms around holes with a high chemical reactivity may lead to self-repairing of nanoholes or unwanted atom adsorption under certain environmental conditions. Development of passivation strategies to make these edge-site atoms chemically inert is expected to improve the performance stability of holey 2D materials if necessary. For instance, it has been proved that nanoholes on graphene can be stable over a few months via Si decoration. Thirdly, compared to pristine counterparts, holey 2D materials often possess a reduced mechanical strength as the holes become preferential sites for crack initiation under loading conditions. Considering charging and discharging of electrochemical devices may involve significant volume change of electrodes, it is key to realize a balance between hole size/density and mechanical properties via the rational design and controlled fabrication. Assembling holey 2D materials with other structural supportive materials (e.g., nanotubes, fibers, etc.) into composites may help.

Electronic, magnetic, and optical properties: It is reported that creating and doping of holes on 2D materials can change their optoelectronic properties. For example, holey 2D materials typically exhibit reduced electrical conductivity due to the degraded lattice structure and increased boundary/edge scattering of electrons. The introduction of holes to graphene can open a band gap in its electronic band structure [176] and lead to tunable optical absorption spectra as predicted by DFT calculations[177]. A broad and significant optical absorption in monolayer holey graphene over the visible spectrum of light has been predicted[176]. Another study reported that chemical species like hydrogen, oxygen, and boron absorbed by nitrogenated holey graphene, will lead to the evolution of mid-gap states that are quite near to the Fermi level[178]. The density of states for spin up and down channels reveal the existence of a nonvanishing magnetic moment within the case of nitrogenated holey graphene adsorbed with hydrogen and boron atoms. The existence of magnetic moments imparts magnetoresistance to nitrogenated holey graphene with modest levels of adsorbed species.

Thermoelectric and phonon transport properties: New phonon modes (including extended and localized modes) can emerge through the introduction of micro-/nano-holes to 2D materials, which has led to the investigations of phonon metamaterials (also known as phononic crystals). Moreover, the added holes directly change the scattering rates and mean-free-path of electrons and phonons by increasing boundary/edge scattering sites, leading to a substantial change in their conductivities. First-principles and semi-classical Boltzmann transport analysis have predicted that high Seebeck coefficient values emerge from the flat bands near the Fermi level along with a wide band gap in nitrogenated holey graphene[179], which exhibit a low lattice thermal conductivity from strong anharmonic scattering and high electron mobility due to the dipping of conduction bands at the Brillouin zone center. Besides, it is predicted that the nitrogen atoms in the nitrogenated holey graphene layer display additional phonon modes, and the specific heat variation with temperature is linear at low temperatures but follows the Dulong-Petit law at high temperatures[180].

CRediT authorship contribution statement

Sun Haofan: Writing – review & editing. **Jiang Xinyu:** Writing –

review & editing. **Nian Qiong:** Writing – review & editing, Supervision, Methodology, Funding acquisition, Data curation, Conceptualization. **Bi Kun:** Writing – review & editing, Validation, Data curation. **Panneerselvam Iyyappa Rajan:** Writing – review & editing. **Liao Yiliang:** Writing – review & editing, Supervision. **Dou Yan:** Writing – review & editing, Validation, Data curation. **Ding Ling:** Supervision. **Zhang Xing:** Writing – review & editing, Validation, Data curation. **Lu Yongfeng:** Writing – review & editing, Supervision. **Wang Yan:** Writing – review & editing, Supervision. **Wang Dini:** Writing – original draft, Methodology, Data curation, Conceptualization. **Zhuang Houlong:** Writing – review & editing. **Dai Rui:** Writing – review & editing. **Song Kenan:** Writing – review & editing.

Declaration of Competing Interest

The authors declare the following financial interests/personal relationships which may be considered as potential competing interests: Qiong Nian reports financial support was provided by National Science Foundation.

Data Availability

Data will be made available on request.

Acknowledgements

This study was partially supported by NSF grants CMMI-1826392, CMMI-1826439, CMMI-1825576 National Science Foundation EFRI (award # 2132183), and CMMI-1825608. We acknowledge the use of facilities within the Eyring Materials Center at Arizona State University supported in part by NNCI-ECCS-1542160.

References

[1] (a) Y. Dong, Z.-S. Wu, W. Ren, H.-M. Cheng, X. Bao, Sci. Bull. 62 (2017) 724; (b) X. Zhang, L. Hou, A. Ciesielski, P. Samorì, Adv. Energy Mater. 6 (2016) 1600671.
[2] J. Tan, S. Li, B. Liu, H.-M. Cheng, Small Struct. 2 (2021) 2000093.
[3] Z.L. Lei, B. Guo, Adv. Sci. 9 (2022) 2102924.
[4] G.H. Jeong, S.P. Sasikala, T. Yun, G.Y. Lee, W.J. Lee, S.O. Kim, Adv. Mater. 32 (2020) 1907006.
[5] Z. Li, S. Gadipelli, H. Li, C.A. Howard, D.J.L. Brett, P.R. Shearing, Z. Guo, I. P. Parkin, F. Li, Nat. Energy 5 (2020) 160.
[6] (a) L. Li, F. Yang, G.J. Ye, Z. Zhang, Z. Zhu, W. Lou, X. Zhou, L. Li, K. Watanabe, T. Taniguchi, Nat. Nanotechnol. 11 (2016) 593; (b) Y. Zhang, Y.-W. Tan, H.L. Stormer, P. Kim, nature 438 (2005) 201; (c) S.H. Mir, V.K. Yadav, J.K. Singh, ACS Omega 5 (2020) 14203.
[7] S. Gupta, S.N. Shirodkar, A. Kutana, B.I. Yakobson, ACS nano 12 (2018) 10880.
[8] (a) M.C. Lemme, D. Akinwande, C. Huyghebaert, C. Stampfer, Nat. Commun. 13 (1) (2022); (b) Z. Cheng, R. Cao, K. Wei, Y. Yao, X. Liu, J. Kang, J. Dong, Z. Shi, H. Zhang, X. Zhang, Adv. Sci. 8 (2021) 2003834.
[9] H. Zhu, X. Gan, A. McCreary, R. Lv, Z. Lin, M. Terrones, Nano Today 30 (2020) 100829.
[10] M. Acerce, D. Voiry, M. Chhowalla, Nat. Nanotechnol. 10 (2015) 313.
[11] H. Li, Y. Tan, P. Liu, C. Guo, M. Luo, J. Han, T. Lin, F. Huang, M. Chen, Adv. Mater. 28 (2016) 8945.
[12] C. Yan, C. Lv, Y. Zhu, G. Chen, J. Sun, G. Yu, Adv. Mater. 29 (2017) 1703909.
[13] E. Pomerantseva, Y. Gogotsi, Nat. Energy 2 (2017) 1.
[14] E. Paek, A.J. Pak, K.E. Kweon, G.S. Hwang, J. Phys. Chem. C. 117 (2013) 5610.
[15] X. Wang, X. Shen, Z. Wang, R. Yu, L. Chen, ACS nano 8 (2014) 11394.
[16] X. Chen, Z. Feng, J. Gohil, C.M. Stafford, N. Dai, L. Huang, H. Lin, ACS Appl. Mater. Interfaces 12 (2019) 1387.
[17] C.E. Ren, M.Q. Zhao, T. Makaryan, J. Halim, M. Boota, S. Kota, B. Anasori, M. W. Barsoum, Y. Gogotsi, ChemElectroChem 3 (2016) 689.
[18] T. Liu, L. Zhang, B. Cheng, X. Hu, J. Yu, Cell Rep. Phys. Sci. 1 (2020) 100215.
[19] Y. Chen, Z.P. Michael, G.P. Kotchey, Y. Zhao, A. Star, ACS Appl. Mater. Interfaces 6 (2014) 3805.
[20] J. Safaei, P. Xiong, G. Wang, Mater. Today Adv. 8 (2020) 100108.
[21] B. Ni, X. Wang, Adv. Sci. 2 (2015) 1500085.
[22] L. Peng, Z. Fang, Y. Zhu, C. Yan, G. Yu, Adv. Energy Mater. 8 (2018) 1702179.
[23] (a) N.S. Rajput, S. Al Zadjali, M. Gutierrez, A.M. Esawi, M. Al Teneiji, RSC Adv. 11 (2021) 27381; (b) Y. Lin, Y. Liao, Z. Chen, J.W. Connell, Mater. Res. Lett. 5 (2017) 209; (c) A. Lokhande, I. Qattan, C.D. Lokhande, S.P. Patole, J. Mater. Chem. A 8 (2020) 918.
[24] V. Nithya, J. Energy Storage 44 (2021) 103380.
[25] Z. Chen, X. An, L. Dai, Y. Xu, Nano Energy 73 (2020) 104762.
[26] K.S. Novoselov, V.I. Fal'ko, L. Colombo, P.R. Gellert, M.G. Schwab, K. Kim, Nature 490 (2012) 192.
[27] (a) R. Raccichini, A. Varzi, S. Passerini, B. Scrosati, Nat. Mater. 14 (2015) 271; (b) K.S. Novoselov, A. Mishchenko, A. Carvalho, A. H. Castro Neto (2016) 353.
[28] J. Bai, X. Zhong, S. Jiang, Y. Huang, X. Duan, Nat. Nanotechnol. 5 (2010) 190.
[29] X. Zhao, C.M. Hayner, M.C. Kung, H.H. Kung, ACS Nano 5 (2011) 8739.
[30] K. Poonam, A. Sharma, Arora, S.K. Tripathi, J. Energy Storage 21 (2019) 801.
[31] C.-H. Yang, P.-L. Huang, X.-F. Luo, C.-H. Wang, C. Li, Y.-H. Wu, J.-K. Chang, ChemSusChem 8 (2015) 1779.
[32] K.A. Sammed, L. Pan, M. Asif, M. Usman, T. Cong, F. Amjad, M.A. Imran, Sci. Rep. 10 (2020) 2315.
[33] Y. Xu, Z. Lin, X. Zhong, X. Huang, N.O. Weiss, Y. Huang, X. Duan, Nat. Commun. 5 (2014) 4554.
[34] Z. Pan, H. Zhi, Y. Qiu, J. Yang, L. Xing, Q. Zhang, X. Ding, X. Wang, G. Xu, H. Yuan, M. Chen, W. Li, Y. Yao, N. Motta, M. Liu, Y. Zhang, Nano Energy 46 (2018) 266.
[35] P. Du, Y. Dong, H. Kang, Q. Wang, J. Niu, Electrochim. Acta 320 (2019) 134610.
[36] J. Liu, P. Du, Q. Wang, D. Liu, P. Liu, Electrochim. Acta 305 (2019) 175.
[37] S. Zhai, C. Wang, H.E. Karahan, Y. Wang, X. Chen, X. Sui, Q. Huang, X. Liao, X. Wang, Y. Chen, Small 14 (2018) 1800582.
[38] X. Chen, J. Han, X. Lv, W. Lv, Z.-Z. Pan, C. Luo, S. Zhang, Q. Lin, F. Kang, Q. H. Yang, , J. Mater. Chem. A (2019).
[39] M. Kotal, H. Kim, S. Roy, I. Oh, J. Mater. Chem. A 5 (2017) 17253.
[40] X. Ye, Y. Zhu, H. Jiang, Z. Yue, L. Wang, Z. Wan, C. Jia, J. Power Sources 441 (2019) 227167.
[41] Z. Fan, Z. Cheng, J. Feng, Z. Xie, Y. Liu, Y. Wang, J. Mater. Chem. A 5 (2017) 16689.
[42] Z. Fan, Y. Wang, Z. Xie, D. Wang, Y. Yuan, H. Kang, B. Su, Z. Cheng, Y. Liu, Adv. Sci. (2018) 1800750.
[43] M.D. Stoller, R.S. Ruoff, Energy Environ. Sci. 3 (2010) 1294.
[44] Y. Xu, C.-Y. Chen, Z. Zhao, Z. Lin, C. Lee, X. Xu, C. Wang, Y. Huang, M.I. Shakir, X. Duan, Nano Lett. 15 (2015) 4605.
[45] Z. Fan, J. Yan, T. Wei, L. Zhi, G. Ning, T. Li, F. Wei, Adv. Funct. Mater. 21 (2011) 2366.
[46] A.-K. Lu, H.-Y. Li, Y. Yu, J. Mater. Chem. A (2019).
[47] A.C. Lokhande, S. Teotia, I.A. Qattan, D. Anjum, K. Liao, S.P. Patole, Mater. Lett. 271 (2020) 127793.
[48] C. Wang, S. Zhai, Z. Yuan, J. Chen, X. Zhang, Q. Huang, Y. Wang, X. Liao, L. Wei, Y. Chen, Electrochim. Acta 305 (2019) 493.
[49] J.H. Jeong, G.-W. Lee, Y.H. Kim, Y.J. Choi, K.C. Roh, K.-B. Kim, Chem. Eng. J. 378 (2019) 122126.
[50] D. Wu, C. Wang, H. Wu, S. Wang, F. Wang, Z. Chen, T. Zhao, Z. Zhang, L. Y. Zhang, C.M. Li, Carbon 163 (2020) 137.
[51] J. Zhao, Y.-Z. Zhang, F. Zhang, H. Liang, F. Ming, H.N. Alshareef, Z. Gao, Adv. Energy Mater. 9 (2019) 1803215.
[52] J. Zhao, Y.-Z. Zhang, J. Chen, W. Zhang, D. Yuan, R. Chua, H.N. Alshareef, Y. Ma, Adv. Energy Mater. 10 (2020) 2000099.
[53] Y. Lin, K.J. Jones, L.C. Greenburg, J.W. Kim, L. Hu, J.W. Connell, Batter. Supercaps 2 (2019) 774.
[54] C. Li, X.-L. Sui, Z.-B. Wang, Q. Wang, D.-M. Gu, Chem. Eng. J. 326 (2017) 265.
[55] X. Tian, K. Tang, H. Jin, T. Wang, X. Liu, W. Yang, Z. Zou, S. Hou, K. Zhou, Carbon (2019).
[56] H. Sun, L. Mei, J. Liang, Z. Zhao, C. Lee, H. Fei, M. Ding, J. Lau, M. Li, C. Wang, X. Xu, G. Hao, B. Papandrea, I. Shakir, B. Dunn, Y. Huang, X. Duan, Science 356 (2017) 599.
[57] X. Han, M.R. Funk, F. Shen, Y.-C. Chen, Y. Li, C.J. Campbell, J. Dai, X. Yang, J.-W. Kim, Y. Liao, J.W. Connell, V. Barone, Z. Chen, Y. Lin, L. Hu, ACS Nano 8 (2014) 8255.
[58] E.D. Walsh, X. Han, S.D. Lacey, J.-W. Kim, J.W. Connell, L. Hu, Y. Lin, ACS Appl. Mater. Interfaces 8 (2016) 29478.
[59] Y. Bai, X. Yang, Y. He, J. Zhang, L. Kang, H. Xu, F. Shi, Z. Lei, Z.-H. Liu, Electrochim. Acta 187 (2016) 543.
[60] Y.-Y. Peng, Y.-M. Liu, J.-K. Chang, C.-H. Wu, M.-D. Ger, N.-W. Pu, C.-L. Chang, Carbon 81 (2015) 347.
[61] D. Wang, R. Dai, X. Zhang, L. Liu, H. Zhuang, Y. Lu, Y. Wang, Y. Liao, Q. Nian, Carbon 161 (2020) 880.
[62] H.-K. Kim, S.-M. Bak, S.W. Lee, M.-S. Kim, B. Park, S.C. Lee, Y.J. Choi, S.C. Jun, J. T. Han, K.-W. Nam, K.Y. Chung, J. Wang, J. Zhou, X.-Q. Yang, K.C. Roh, K.-B. Kim, Energy Environ. Sci. 9 (2016) 1270.
[63] P. Zang, S. Gao, L. Dang, Z. Liu, Z. Lei, Electrochim. Acta 212 (2016) 171.
[64] X. Liu, L. Liu, J. Zhang, Q. Meng, Colloids Surf. A: Physicochem. Eng. Asp. 618 (2021) 126463.
[65] P. Xu, Q. Gao, L. Ma, Z. Li, H. Zhang, H. Xiao, X. Liang, T. Zhang, X. Tian, C. Liu, Carbon (2019).
[66] Z.-j Jiang, Z. Jiang, W. Chen, J. Power Sources 251 (2014) 55.
[67] F. Su, S. Zheng, F. Liu, X. Zhang, F. Su, Z.-S. Wu, Chin. Chem. Lett. 32 (2021) 914.
[68] Z. Zhu, Z. Wang, Z. Ba, J. Dong, Q. Zhang, X. Zhao, J. Energy Storage 39 (2021) 102658.
[69] B. Zhu, R. Guo, H. Li, H. Liu, J. Mater. Res. 36 (2021) 4169.
[70] Y. Zou, Z. Chen, Z. Peng, C. Yu, W. Zhong, Nanoscale 13 (2021) 16734.
[71] Y. He, Y. Bai, X. Yang, J. Zhang, L. Kang, H. Xu, F. Shi, Z. Lei, Z.-H. Liu, J. Power Sources 317 (2016) 10.
[72] C. Lai, S. Wang, L. Cheng, Y. Wang, L. Fu, Y. Sun, B. Lin, Electrochim. Acta 365 (2021) 137334.

[73] M. Yun, Y. Ma, Z. Cai, H. Ji, J. Han, M. Wang, Z. Tong, L. Xiao, S. Jia, X. Chen, Ceram. Int. 47 (2021) 27210.

[74] Y. Jiang, X. Li, F. Liu, B. Wang, W. Zhou, S. Dong, X. Fan, Appl. Surf. Sci. 576 (2022) 151801.

[75] J. Feng, L. Liu, Q. Meng, J. Colloid Interface Sci. 582 (2021) 447.

[76] Y. Chai, Z. Li, J. Wang, Z. Mo, S. Yang, J. Alloy. Compd. 775 (2019) 1206.

[77] S. Hwa Park, H. Jun Park, S. Gyu Son, D. Seok Kim, S. Jin Kim, H. Suh, J. shin, T. Ryu, J.-M. Jeong, B. Gill Choi, FlatChem 29 (2021) 100268.

[78] C. Yang, Q. Pan, Q. Jia, W. Qi, H. Wei, S. Yang, N. Hu, B. Cao, Chem. Eng. J. 408 (2021) 127302.

[79] Y. Bai, Z. Yan, L. Kang, Z.-H. Liu, J. Alloy. Compd. 780 (2019) 792.

[80] Z. Zhu, Z. Wang, Z. Ba, X. Li, J. Dong, Y. Fang, Q. Zhang, X. Zhao, J. Energy Storage 47 (2022) 103911.

[81] E. Alsharaeh, F. Ahmed, Y. Aldawsari, M. Khasawneh, H. Abuhimd, M. Alshahrani, Sci. Rep. 6 (2016) 29854.

[82] Y. Wang, D. Adekoya, J. Sun, T. Tang, H. Qiu, L. Xu, S. Zhang, Y. Hou, Adv. Funct. Mater. 0 (2018) 1807485.

[83] F. Xiao, Y. Meng, Z. Lin, Y. Lei, X. Chen, J. Zhang, H. Lu, Y. Tong, G. Liu, J. Xu, Carbon 189 (2022) 404.

[84] J. Zhang, X. Chen, Y. Lei, H. Lu, J. Xu, S. Wang, M. Yan, F. Xiao, J. Xu, Chem. Eng. J. 428 (2022) 131025.

[85] H.C. Shim, C.V. Tran, S. Hyun, J.B. In, Appl. Surf. Sci. 564 (2021) 150416.

[86] B. Wang, F. Jin, Y. Xie, H. Luo, F. Wang, T. Ruan, D. Wang, Y. Zhou, S. Dou, Energy Storage Materials 2019.

[87] C. Zheng, X. Xu, Q. Lin, Y. Chen, Z. Guo, B. Jian, N. Li, H. Zhang, W. Lv, Carbon 176 (2021) 31.

[88] X. Jiao, Q. Hao, X. Xia, D. Yao, Y. Ouyang, W. Lei, J. Power Sources 403 (2018) 66.

[89] D. Hu, C. Zhu, Y. Yao, S. Liu, X. Meng, H. Yuan, Z. Chen, X. Jiang, Y. Li, S. Zhu, Appl. Surf. Sci. 542 (2021) 148496.

[90] Z. Mi, D. Hu, J. Lin, H. Pan, Z. Chen, Y. Li, Q. Liu, S. Zhu, Electrochim. Acta 403 (2022) 139711.

[91] S.G. Stolyarova, V.O. Koroteev, Y.V. Shubin, P.E. Plyusnin, A.A. Makarova, A.V. Okotrub, L.G. Bulusheva, Energy Technology 2019.

[92] Y. Xiang, W. Zhang, B. Chen, Z. Jin, H. Zhang, P. Zhao, G. Cao, Q. Meng, J. Power Sources 447 (2020) 227372.

[93] R. Mo, D. Rooney, K. Sun, J.N. Wang, Chem. Eng. J. 417 (2021) 128475.

[94] D. Yang, B. Xu, Q. Zhao, X.S. Zhao, J. Mater. Chem. A (2019).

[95] L. Zhang, J. Yue, T. Wei, Z. Liu, J. Zhou, C. Liu, H. Jiang, Z. Jiang, Z. Fan, Carbon 142 (2019) 327.

[96] C. Zhu, Z. Hui, H. Pan, S. Zhu, Q. Zhang, J. Mao, Z. Guo, Y. Li, M. Imtiaz, Z. Chen, J. Mater. Chem. A 7 (2019) 4788.

[97] F. Li, M. Zhang, W. Chen, X. Cai, H. Rao, J. Chang, Y. Fang, X. Zhong, Y. Yang, Z. Yang, X. Yu, ACS Appl. Mater. Interfaces 13 (2021) 30746.

[98] T. Wang, Q. Zhang, J. Zhong, M. Chen, H. Deng, J. Cao, L. Wang, L. Peng, J. Zhu, B. Lu, Adv. Energy Mater. 11 (2021) 2100448.

[99] J. Li, X. Li, X. Fan, T. Tang, M. Li, Y. Zeng, H. Wang, J. Wen, J. Xiao, Carbon 188 (2022) 155.

[100] J. Xu, Y. Meng, Q. Ding, R. Wang, T. Gan, J. Zhang, Z. Lin, J. Xu, J. Mater. Chem. A (2022).

[101] D.J. Kirsch, S.D. Lacey, Y. Kuang, G. Pastel, H. Xie, J.W. Connell, Y. Lin, L. Hu, ACS Appl. Energ. Mater. 2 (2019) 2990.

[102] X. Han, Z. Yang, B. Zhao, S. Zhu, L. Zhou, J. Dai, J.-W. Kim, B. Liu, J.W. Connell, T. Li, B. Yang, Y. Lin, L. Hu, ACS Nano 11 (2017) 3189.

[103] D. Yu, L. Wei, W. Jiang, H. Wang, B. Sun, Q. Zhang, K. Goh, R. Si, Y. Chen, Nanoscale 5 (2013) 3457.

[104] Y. Bian, H. Wang, J. Hu, B. Liu, D. Liu, L. Dai, Carbon 162 (2020) 66.

[105] P. Du, K. Hu, J. Lyu, H. Li, X. Lin, G. Xie, X. Liu, Y. Ito, H.-J. Qiu, Appl. Catal. B: Environ. 276 (2020) 119172.

[106] W. Kong, K. Yao, X. Duan, Z. Liu, J. Hu, Electrochim. Acta 269 (2018) 544.

[107] X. Shu, S. Chen, S. Chen, W. Pan, J. Zhang, Carbon 157 (2020) 234.

[108] P. Wu, J. Wu, H. Si, Z. Zhang, Q. Liao, X. Wang, F. Dai, K. Ammarah, Z. Kang, Y. Zhang, Adv. Energy Mater. 10 (2020) 2001005.

[109] L. Qie, Y. Lin, J.W. Connell, J. Xu, L. Dai, Angew. Chem. Int. Ed. 56 (2017) 6970.

[110] C. Hu, L. Gong, Y. Xiao, Y. Yuan, N.M. Bedford, Z. Xia, L. Ma, T. Wu, Y. Lin, J. W. Connell, R. Shahbazian-Yassar, J. Lu, K. Amine, L. Dai, Adv. Mater. 32 (2020) 1907436.

[111] Y. Luo, L. Tang, U. Khan, Q. Yu, H.-M. Cheng, X. Zou, B. Liu, Nat. Commun. 10 (2019) 269.

[112] Y. Ito, T. Ohto, D. Hojo, M. Wakisaka, Y. Nagata, L. Chen, K. Hu, M. Izumi, J.-i Fujita, T. Adschiri, ACS Catal. 8 (2018) 3579.

[113] A. Kumatani, C. Miura, H. Kuramochi, T. Ohto, M. Wakisaka, Y. Nagata, H. Ida, Y. Takahashi, K. Hu, S. Jeong, J.-i Fujita, T. Matsue, Y. Ito, Adv. Sci. 6 (2019) 1900119.

[114] K. Savaram, M. Li, K. Tajima, K. Takai, T. Hayashi, G. Hall, E. Garfunkel, V. Osipov, H. He, Carbon 139 (2018) 861.

[115] G. Li, D. Dong, G. Hong, L. Yan, X. Zhang, W. Song, Adv. Mater. (2019).

[116] F. Mo, Z. Ma, T. Wu, M. Liu, Y. Zhang, H. Li, S. Yao, Sens. Actuators B: Chem. 281 (2019) 486.

[117] W. Kong, X. Duan, Y. Ge, H. Liu, J. Hu, X. Duan, Nano Res. 9 (2016) 2458.

[118] X. Liu, L. Jiang, Z. Zhu, S. Chen, Y. Dou, P. Liu, Y. Wang, H. Yin, Z. Tang, H. Zhao, Mater. Today Energy 11 (2019) 24.

[119] M. Ali, R. Riaz, A.S. Anjum, K.C. Sun, H. Li, S.H. Jeong, M.J. Ko, Carbon 171 (2021) 493.

[120] R. Lv, H. Wang, H. Yu, F. Peng, Electrochim. Acta 228 (2017) 203.

[121] Y. Zhao, C. Hu, L. Song, L. Wang, G. Shi, L. Dai, L. Qu, Energy Environ. Sci. 7 (2014) 1913.

[122] S.B. Jin, J.-M. Jeong, S.G. Son, S.H. Park, K.G. Lee, B.G. Choi, Mater. Today Commun. 26 (2021) 101857.

[123] K.S. Novoselov, V.I. Falʹko, L. Colombo, P.R. Gellert, M.G. Schwab, K. Kim, Nature 490 (2012) 192.

[124] M. Mi, X. Liu, W. Kong, Y. Ge, W. Dang, J. Hu, Desalination 464 (2019) 18.

[125] Y. Yang, X. Yang, L. Liang, Y. Gao, H. Cheng, X. Li, M. Zou, R. Ma, Q. Yuan, X. Duan, Science 364 (2019) 1057.

[126] J. Jiang, D. Cui, T. Yan, F. Guo, W. Gu, Phys. E: Low. -Dimens. Syst. Nanostruct. 124 (2020) 114303.

[127] J. Liu, H. Cai, X. Yu, K. Zhang, X. Li, J. Li, N. Pan, Q. Shi, Y. Luo, X. Wang, J. Phys. Chem. C. 116 (2012) 15741.

[128] G.F. Schneider, S.W. Kowalczyk, V.E. Calado, G. Pandraud, H.W. Zandbergen, L. M. Vandersypen, C. Dekker, Nano Lett. 10 (2010) 3163.

[129] Y. Yang, Z. Chen, Q. Wang, Q. Wang, Y. Zhang, Phys. Status Solidi (a) 219 (2022) 2100412.

[130] X. Liang, Y.S. Jung, S. Wu, A. Ismach, D.L. Olynick, S. Cabrini, J. Bokor, Nano Lett. 10 (2010) 2454.

[131] Z. Zeng, X. Huang, Z. Yin, H. Li, Y. Chen, H. Li, Q. Zhang, J. Ma, F. Boey, H. Zhang, Adv. Mater. 24 (2012) 4138.

[132] D.-P. Yang, X. Wang, X. Guo, X. Zhi, K. Wang, C. Li, G. Huang, G. Shen, Y. Mei, D. Cui, J. Phys. Chem. C. 118 (2013) 725.

[133] O. Akhavan, ACS nano 4 (2010) 4174.

[134] D. Singh, V. Shukla, R. Ahuja, in *arXiv.org*, 2020.

[135] J. Mahmood, E.K. Lee, M. Jung, D. Shin, I.Y. Jeon, S.M. Jung, H.J. Choi, J.M. Seo, S.Y. Bae, S.D. Sohn, N. Park, J.H. Oh, H.J. Shin, J.B. Baek, Nat. Commun. 6 (2015) 6486.

[136] J. Mahmood, F. Li, C. Kim, H.-J. Choi, O. Gwon, S.-M. Jung, J.-M. Seo, S.-J. Cho, Y.-W. Ju, H.Y. Jeong, G. Kim, J.-B. Baek, Nano Energy 44 (2018) 304.

[137] J. Kim, O. Gwon, O. Kwon, J. Mahmood, C. Kim, Y. Yang, H. Lee, J.H. Lee, H. Y. Jeong, J.-B. Baek, G. Kim, ACS Nano 13 (2019) 5502.

[138] Y. Liao, K. Tu, X. Han, L. Hu, J.W. Connell, Z. Chen, Y. Lin, Sci. Rep. 5 (2015) 14510.

[139] H. Liu, P. Lian, Q. Zhang, Y. Yang, Y. Mei, Electrochem. Commun. 98 (2019) 124.

[140] L. Peng, P. Xiong, L. Ma, Y. Yuan, Y. Zhu, D. Chen, X. Luo, J. Lu, K. Amine, G. Yu, Nat. Commun. 8 (2017) 15139.

[141] D. Chen, L. Peng, Y. Yuan, Y. Zhu, Z. Fang, C. Yan, G. Chen, R. Shahbazian-Yassar, J. Lu, K. Amine, G. Yu, Nano Lett. 17 (2017) 3907.

[142] H. Huang, G. Zhao, N. Zhang, K. Sun, Nanoscale 11 (2019) 16222.

[143] W. Yao, Z. Xu, X. Xu, Y. Xie, W. Qiu, J. Xu, D. Zhang, Electrochim. Acta 292 (2018) 390.

[144] B. Saravanakumar, X. Wang, W. Zhang, L. Xing, W. Li, Chem. Eng. J. 373 (2019) 547.

[145] H.-P. Guo, X.-W. Gao, N.-F. Yu, Z. Zheng, W.-B. Luo, C. Wu, H.-K. Liu, J.-Z. Wang, J. Mater. Chem. A 7 (2019) 26549.

[146] Y. Wu, T. Cao, R. Wang, F. Meng, J. Zhang, C. Cao, J. Mater. Chem. A 6 (2018) 8374.

[147] T.F. Jaramillo, K.P. Jørgensen, J. Bonde, J.H. Nielsen, S. Horch, I. Chorkendorff, Science 317 (2007) 100.

[148] D. Sarkar, B. Mondal, A. Som, S.J. Ravindran, S.K. Jana, C.K. Manju, T. Pradeep, Glob. Chall. 2 (2018) 1800052.

[149] Z. Fang, L. Peng, H. Lv, Y. Zhu, C. Yan, S. Wang, P. Kalyani, X. Wu, G. Yu, ACS Nano 11 (2017) 9550.

[150] M. Mojtabavi, A. VahidMohammadi, W. Liang, M. Beidaghi, M. Wanunu, ACS Nano 13 (2019) 3042.

[151] N.L.W. Septiani, Y.V. Kaneti, Y. Guo, B. Yuliarto, X. Jiang, Y. Ide, N. Nugraha, H. K. Dipojono, A. Yu, Y. Sugahara, D. Golberg, Y. Yamauchi, ChemSusChem 13 (2020) 1645.

[152] X. Wang, L. Jiao, K. Sheng, C. Li, L. Dai, G. Shi, Sci. Rep. 3 (2013) 1996.

[153] W. Seo, D.L. White, A. Star, Chem. – A Eur. J. 23 (2017) 5652.

[154] Y. Lin, X. Han, C.J. Campbell, J.-W. Kim, B. Zhao, W. Luo, J. Dai, L. Hu, J. W. Connell, Adv. Funct. Mater. 25 (2015) 2920.

[155] (a) S.D. Lacey, E.D. Walsh, E. Hitz, J. Dai, J.W. Connell, L. Hu, Y. Lin, Nano Energy 31 (2017) 386;
(b) Y. Lin, B. Moitoso, C. Martinez-Martinez, E.D. Walsh, S.D. Lacey, J.-W. Kim, L. Dai, L. Hu, J.W. Connell, Nano Lett. 17 (2017) 3252.

[156] Y. Lin, K.A. Watson, J.-W. Kim, D.W. Baggett, D.C. Working, J.W. Connell, Nanoscale 5 (2013) 7814.

[157] C. Guo, Y. Zhang, T. Zeng, D. Huang, Q. Wan, N. Yang, Carbon 157 (2020) 298.

[158] J. Wang, T. Park, J.W. Yi, B. Ding, J. Henzie, Z. Chang, H. Dou, X. Zhang, Y. Yamauchi, Nanoscale Horiz. 4 (2019) 526.

[159] M. Patel, W. Feng, K. Savaram, M.R. Khoshi, R. Huang, J. Sun, E. Rabie, C. Flach, R. Mendelsohn, E. Garfunkel, H. He, Small 11 (2015) 3358.

[160] J.G. Radich, P.V. Kamat, ACS Nano 7 (2013) 5546.

[161] D.L. White, S.C. Burkert, S.I. Hwang, A. Star, Nano Lett. (2019).

[162] L. Peng, Z. Fang, J. Li, L. Wang, A.M. Bruck, Y. Zhu, Y. Zhang, K.J. Takeuchi, A. C. Marschilok, E.A. Stach, E.S. Takeuchi, G. Yu, ACS Nano 12 (2018) 820.

[163] G.-D. Sun, G.-H. Zhang, K.-C. Chou, Ceram. Int. 46 (2020) 4024.

[164] C. Cai, Q. Sui, Z. She, H.-B. Kraatz, C. Xiang, P. Huang, H. Chu, S. Qiu, F. Xu, L. Sun, A. Shah, Y. Zou, Electrochim. Acta 283 (2018) 904.

[165] H. Zhao, Z. Tang, J. Sun, S.E. Lowe, L. Zhang, Y. Wang, K. Pang, Y. Wang, Y. Zhong, P. Liu, K. Zhao, Angew. Chem. Int Ed. 0 (2018) 16511.

[166] Z. Li, H. Zhang, J. Han, Y. Chen, H. Lin, T. Yang, Adv. Mater. 30 (2018) 1706981.

[167] K. Bi, D. Wang, R. Dai, L. Liu, Y. Wang, Y.-F. Lu, Y. Liao, L. Ding, H.L. Zhuang, Q. Nian, Nanoscale (2022).

[168] (a) R.S. Ribeiro, A.M. Silva, J.L. Figueiredo, J.L. Faria, H.T. Gomes, Carbon 62 (2013) 97;
(b) W. Xing, G. Lalwani, I. Rusakova, B. Sitharaman, Part. Part. Syst. Charact. 31 (2014) 745;
(c) K. Bi, D. Wang, R. Dai, L. Liu, Y. Wang, Y. Lu, Y. Liao, L. Ding, H. Zhuang, Q. Nian, Nanoscale 14 (2022) 4762.
[169] S.S. Datta, D.R. Strachan, S.M. Khamis, A.T.C. Johnson, Nano Lett. 8 (2008) 1912.
[170] L.C. Campos, V.R. Manfrinato, J.D. Sanchez-Yamagishi, J. Kong, P. Jarillo-Herrero, Nano Lett. 9 (2009) 2600.
[171] Y. Zhang, Z. Li, P. Kim, L. Zhang, C. Zhou, ACS Nano 6 (2012) 126.
[172] K. Liu, J. Feng, A. Kis, A. Radenovic, ACS Nano 8 (2014) 2504.
[173] G. Danda, P. Masih Das, Y.C. Chou, J.T. Mlack, W.M. Parkin, C.H. Naylor, K. Fujisawa, T. Zhang, L.B. Fulton, M. Terrones, A.T. Johnson, M. Drndic, ACS Nano 11 (2017) 1937.
[174] S. Liu, B. Lu, Q. Zhao, J. Li, T. Gao, Y. Chen, Y. Zhang, Z. Liu, Z. Fan, F. Yang, L. You, D. Yu, Adv. Mater. 25 (2013) 4549.
[175] B. Mortazavi, O. Rahaman, T. Rabczuk, L.F.C. Pereira, Carbon 106 (2016) 1.
[176] D. Singh, V. Shukla, R. Ahuja, Phys. Rev. B 102 (2020) 075444.
[177] I.R. Panneerselvam, P. Chakraborty, Q. Nian, Y. Lu, Y. Liao, Y. Wang, Semicond. Sci. Technol. 37 (2021) 025013.
[178] R.M. Tromer, M.G. da Luz, M.S. Ferreira, L.F.C. Pereira, J. Phys. Chem. C. 121 (2017) 3055.
[179] Y. Zhao, Z. Dai, C. Lian, S. Meng, RSC Adv. 7 (2017) 25803.
[180] H. Sahin, Phys. Rev. B 92 (2015) 085421.